Antiferromagnetism, ferromagnetism and magnetic phase separation in $Bi_2Sr_2CoO_{6+\delta}$

by

Kennedy Jessica Thomas

B.S. Physics
Yale University (1997)

Submitted to the Department of Physics
in partial fulfillment of the requirements for the degree of

Doctor of Philosophy

at the

MASSACHUSETTS INSTITUTE OF TECHNOLOGY

February 2003

Author .....
Department of Physics
November 15, 2002

Certified by .....
Marc A. Kastner
Donner Professor of Physics
Thesis Supervisor

Accepted by .....
Thomas Greytak
Professor, Associate Department Head for Education

Antiferromagnetism, ferromagnetism and magnetic phase separation in $Bi_2Sr_2CoO_{6+\delta}$

by

Kennedy Jessica Thomas

Submitted to the Department of Physics
on November 15, 2002, in partial fulfillment of the
requirements for the degree of
Doctor of Philosophy

Abstract

Neutron scattering, magnetization and transport measurements were performed on single crystals of $Bi_2Sr_2CoO_{6+\delta}$ to study the evolution of the magnetic properties as a function of the oxygen content δ. The oxygen content was varied by annealing single crystals in either a reducing or oxidizing environment to obtain an experimental range of $0.25 \leq \delta \leq 0.5$ and a corresponding average Co valence between +2.5 and +3.

We show that the as-grown samples, which are oxygen rich ($\delta \sim 0.5$) and therefore contain mostly Co^{3+} ions, enter an antiferromagnetic (AF) phase with a Néel temperature $\sim$ 250 K. On the other hand, annealing as-grown crystals in vacuum to reach $\delta \sim 0.25$ destroys the AF phase; these samples exhibit predominantly ferromagnetic (FM) behavior with $T_c \sim 100$ K.

At intermediate doping, $0.25 < \delta < 0.5$, we find evidence for co-existence of FM and AF domains, which are characteristic of the $\delta = 0.25$ and $\delta = 0.5$ phases, respectively. The signature of the co-existence is the presence of simultaneous FM and AF magnetic Bragg peaks in the neutron diffraction pattern. Polarized neutron scattering measurements confirm that the FM and AF peaks do not arise from different components of a canted antiferromagnet.

The FM regions give rise to a ferromagnetic-like peak in the susceptibility at the same temperature as the spins in the AF phase order. In addition, the FM regions exert a random field in the AF phase, above a critical field H_c. We explain the field dependence of the two-phase samples with a microscopic model.

We propose that the FM clusters within the AF phase are the result of regions which are rich in Co^{2+}. Furthermore, we suggest that oxygen facilitates the formation of electronically inhomogeneous regions.

Thesis Supervisor: Marc A. Kastner
Title: Donner Professor of Physics

Acknowledgments

I think that, like myself, most students are shocked by the level of independence which is expected at MIT. The expectation is at once liberating and terrifying, and never becomes completely comfortable. For this reason, I feel extremely fortunate to have been surrounded by wonderful faculty, friends and family for the past five years.

I would like to thank my advisor, Marc Kastner, for his guidance and endless enthusiasm for his students' research. Working as a student in Marc's group has been a true apprenticeship in physics. My happiest moments as a student have been spent discussing physics with Marc, fleshing out "back of envelope" calculations to gain intuition for our results. It never fails to amaze me that even as Department Head, Marc has remained consistently involved with the details of his students' research.

I had the good fortune of actually having a second, unofficial advisor. Two years ago, I asked Young Lee, now a professor at MIT, if I could tag along on his next neutron scattering experiment studying $Bi_2Sr_2CoO_{6+\delta}$. Of course, I didn't think I would actually have to DO any of the experiments (I refer to this time in my life as my "naive" period.) Collaborating with Young and working at NIST really helped pull me out of, what was at the time, a pretty bad graduate student slump. I'm happy to say that I saw the light and didn't chuck my degree to work at a video store. In fact, I enjoyed my initial experience at NIST so much that I kept going back, eventually doing the majority of my PhD work in neutron scattering. More importantly, and I hope this doesn't violate some unspoken student-faculty protocol, I think of Young as one of my closest friends. Over what I estimate to be about 600 hours of beam time, we have talked about physics, politics, and religion. I have learned so much from Young's elegant style of expressing physics and I know that our friendship was a major factor in the success of this research project. That, and the 500 matches of hang-man we played while waiting for our data scans to finish (I contend that I am still one up, for the record). I look forward to many future collaborations with Young.

I could write pages of thanks to Dr. Fang Chou, who grew all of the single crystals studied in this thesis, and never fully express how important his work is to the quality of research here at MIT. Anyone who has tried to grow his or her own crystals knows that you are lucky if after six months you have a single crystal bigger than a grain of sand. Yet, Fang routinely grows enormous, beautiful single crystals. He is, in my mind, both a scientist and

an artist.

I benefited from several discussions with faculty and visiting scientists here at MIT. I would like first to thank the other members of my thesis committee, Eric Hudson and Patrick Lee, for making important comments and suggestions. In particular, Patrick Lee proposed the Two-dimensional Random Field Ising model to describe the unusual field dependence observed in $Bi_2Sr_2CoO_{6+\delta}$. I would also like to acknowledge Senthil Todadri for his comments and questions about my research. I thank Robert Cava of Princeton for initiating interest in this project and for introducing me to Henny Zandbergen, a current collaborator. Finally, I am grateful to have had the opportunity to share my research results with Amnon Aharony. His insightful comments have made me think much more deeply about the results of this thesis.

I have learned much about neutron scattering from working with Dr. Jeffrey Lynn at NIST. His enthusiasm for his work and for helping users at the NIST facility is a great motivator.

In some sense, I should also thank my advisor for attracting such bright and well-rounded students and post-docs to his research group. I have enjoyed many conversations, both on scientific matters and otherwise, with my lab mates. When I arrived, both David Goldhaber and Nicole Morgan helped me get started in the lab, even though we were all working on different projects. I met Joern Goeres, who joined Marc's group at the same time as me, as a prospective student. I remember trading e-mails with him while we were deciding where to go, and convincing each other that MIT would be a good place to go to graduate school. Of course, I am *now* trying to forgive him for heading back to Germany after only a year and a half at MIT. I have had a great time on extended bike trips with Andrei Kogan and his wife, Daria. They share with me the vision that the only true objective in biking 30 miles is the cold beer waiting for you at the end. Ghislain Granger always greets me with a warm smile and I have enjoyed our just barely bi-annual "déjueners français". Sami Amasha is an amazing student who has contributed enormously to the social life of the Physics Department. Under his management, the Building 13 cookie hour has grown from a mere afternoon tea into an enterprise. I have enjoyed many conversations about research and research related "angst" with Marija Drndic. I appreciate her creative and broad approach to research. I was really happy when Boris Khaykovich joined the group as a post-doc three years ago. I felt like I finally had a transition metal-oxide ally. Boris

makes great suggestions and has helped me considerably in my research. Finally, it has been a great boost to work with Maria Schriver, an undergraduate in the MIT Physics Department. She is an extremely quick learner and has made impressive progress in her project. I hope very much that she will stay interested in physics.

I would like to thank the staff of the Center for Material Science and Engineering for keeping our labs safe and running smoothly. I would also like to thank Brian Canavan for working so hard to build a sense of community within the Department.

I have enjoyed meeting many other denizens of Building 13. Rebecca Christianson, a graduate student in the Birgeneau group, and I spent three months one summer trying to grow single crystals of $La_{1.875}Sr_{0.125}CuO_4$. What could have been an enormously frustrating experience (see above on why Fang Chou is amazing) was actually a lot of fun with Rebecca. I have known Peter Falus since Day One and he has remained a wonderful friend. I respect that he, his wife, Predrag Nikolic[1] and Philip Singer all willingly suffered through my first experience cooking a Thanksgiving dinner. Valery Kiryukhin occupied the office next to mine for several years and I was definitely charmed by his blunt, Russian style. Most Americans tell young students that it is OK when they screw up; Valery pretty much says it as it is. On neutron and x-ray excursions, I have enjoyed a good deal of pleasant ribbing from Young's students, Kit Matan and Eric Abel. I will remember fondly the many lunches and physics socials that I shared with Steve Moss, Dan Ripin, Alan Hunt, and Dirk Lumma. I am glad that I had the opportunity to run (and bike and swim...) alongside "mini-team MIT-Physics" Kerwyn Casey Huang and Michelle Povinelli.

In Davis Square, the nexus of hip Cambridge culture at the time of this writing, I was lucky to meet two great couples, Kevin and Emily Qazilbash and Lex and Olivia Mathews (and their beautiful children, Ariana and Damian). I would like to thank Terry and Maria for reintroducing me to the logical intricacies of the board game Clue. Brian Bowers, who I met through my husband's work, has been a wonderful friend. My best friend Rebecca is a constant reminder to me that true friendship ties together even the busiest of lifestyles.

My family has provided so much warmth and love my entire life. In the past year, we have shared many celebrations and I look forward to many more. I would like to thank Irene, Bill, Perlette and Marcel and my husband's family, Tom, Rita, Tom Jr, Julia and Timothy.

[1] Actually, Predrag has dual citizenship in Buildings 12 and 13.

My father, Parke, and his wife, Candy, are the two funniest people I have ever met. They have made me laugh with every visit and celebrated with me even the tiniest of achievements.

My husband Mark has supported me in so many ways, I can not even begin to list them. I guess he knew he was in for the long haul when I dragged him out of a rock concert to check a pressure gauge, but he has never complained about the funny hours or his funny wife. I thank him for making me laugh, eating dinner with me at 11:00 at night, and in what probably earned him a halo, proofreading this thesis.

Finally, I want to thank my mother, Marcelle. I feel blessed to be the recipient of so much love from such a beautiful person.

Contents

List of Figures

List of Tables

Chapter 1

Introduction

Interest in cobalt-based transition metal oxides has emerged from two large areas of research: the study of High T_c superconductivity in the cuprates and the study of the magneto-resistive manganites. In these materials, the interesting physics originates from the strongly-interacting electrons associated with the magnetic cations, copper or manganese. By substituting a different transition metal cation in these materials, one hopes to explore the effects of changing the *local* electronic properties, such as the number of electrons and their spin, on the *collective* properties of all of the electrons in the solid.

In order to appreciate the interest in the cobaltates, it is necessary to briefly review the physics in their precursor compounds. The following is a very condensed description of the physical properties of the hole-doped manganites and cuprates; more extensive reviews may be found in References [1, 2, 3, 4, 5].

The phase diagram of the manganite $La_{1-x}Ca_xMnO_3$ is shown in Figure 1-1. The perovskite manganites are described by the general formula $A_{1-x}B_xMnO_3$, where A is a trivalent rare earth (La, Pr) and B is a divalent ion (Ca, Sr). The magnetism in these materials results from the interaction between the spins on neighboring Mn cations. At $x = 0$, all of the Mn ions are 3+ with a localized spin S = 3/2 and a transition to antiferromagnetic order. Substituting La with divalent Sr introduces holes on the Mn sites, with the result that some of the Mn is 4+. The spins on adjacent Mn^{4+} and Mn^{3+} sites have a ferromagnetic interaction which is mediated by the mobile hole on the Mn^{4+}. This double-exchange interaction, which is explained in more detail below, results in a transition to a ferromagnetic, metallic state below a temperature T_c. Large magneto-resistance is

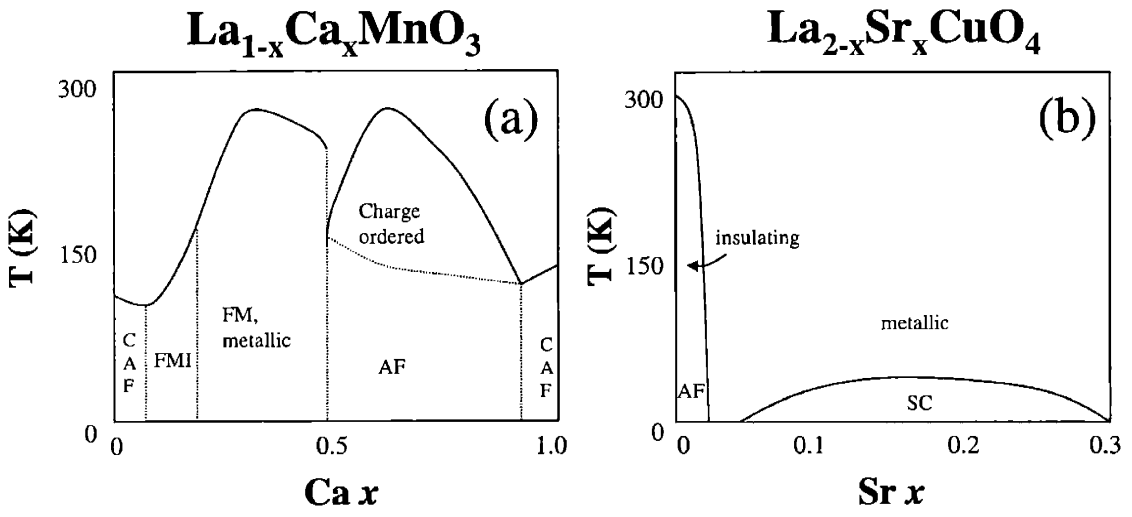

Figure 1-1: Phase diagrams for (a) the hole-doped manganite $La_{1-x}Ca_xMnO_3$ (adapted from [1]) and (b) the hole-doped cuprate $La_{2-x}Sr_xCuO_4$ (adapted from [5]). The dark lines indicate the boundary between different phases as a function of temperature and hole concentration x. The abbreviations are defined as follows: CAF = canted antiferromagnet, AF = antiferromagnet, FMI = ferromagnetic insulator, FM = ferromagnetic, SC = superconducting.

observed at T_c because the paramagnetic phase is insulating. The ferromagnetic phase is stable for a large range of hole densities; however, at $x = 0.5$ a competing charge ordered phase is stabilized at low-temperatures.

The superconducting cuprates exhibit a similarly dramatic evolution with doping. Figure 1-1(b) shows the phase diagram of $La_{2-x}Sr_xCuO_4$, one of the simplest of the High-T_c compounds. In undoped ($x = 0$) $La_{2-x}Sr_xCuO_4$, the electrons are localized on the Cu sites, such that each Cu site has an effective spin S = 1/2. The spin dynamics are governed by the two-dimensional, quantum nature of the spin interactions and the spins undergo a transition to antiferromagnetic order below a Néel temperature $T_N \sim 300$ K. With the addition of a few percent holes, either by doping with strontium or oxygen, the antiferromagnetic phase is completely destroyed. At around 0.06 hole density, $La_{2-x}Sr_xCuO_4$ exhibits unconventional metallic behavior with a transition to superconductivity at $T_c \sim 30$ K.

1.1 Cobalt-based transition metal oxides

Both the cuprates and the manganites have rich phase diagrams as a function of temperature and hole concentration. The complexity in these materials results from the strong interactions between electrons and the fact that the spin, orbital and electronic degrees of freedom on the magnetic ion can not be treated independently. It follows that substituting a *different* magnetic cation does not constitute a small perturbation.

Several Co based compounds, which are similar in structure to either the manganites or the cuprates, have been successfully grown. $La_{1-x}Sr_xCoO_3$ is a Co based derivative of the cubic manganites. This material has received considerable attention following the observation of magneto-resistivity in thin films.[6] Hole-doping with the addition of Sr results in ferromagnetic, metallic behavior, as in the manganites. However, the magnetic behavior in this material has an additional complexity resulting from the spin on the Co^{3+}, which can adopt more than one spin state.[7, 8]

Co based compounds derived from the superconducting cuprates include $La_{2-x}Sr_xCoO_4$, $Bi_2Sr_2CoO_{6+\delta}$ (the subject of this thesis), and $Bi_2M_3Co_2O_\delta$ (M = Ca, Sr, Ba). None of the cobaltates exhibit superconductivity. Indeed, the Bi based cobaltates show semi-conducting behavior over a wide range of temperatures, though lead doping results in increased metallic behavior in the Sr and Ba based $Bi_2M_3Co_2O_\delta$ compounds.[9] In terms of magnetism, neutron studies of the cobaltate La_2CoO_4, which is an insulator with a lattice of spins with S = 3/2, reveal similar two-dimensional behavior above the magnetic transition temperature to that observed in La_2CuO_4.[10] In the Co compound, however, anisotropies play a greater role than in the Heisenberg spin system La_2CuO_4.

Ironically, the cobalt compounds based on the cuprates are now believed to be more closely related to the manganites. $La_{2-x}Sr_xCoO_4$, for example, exhibits charge ordering when $x = 0.5$ and there is an equal concentration of Co^{2+} and Co^{3+}.[11] This is analogous to $x = 0.5$ in the manganites. It should be noted that in $La_{2-x}Sr_xCoO_4$, the spins order at a temperature 20 times *lower* than the charge-ordering temperature, while in the manganites, the magnetic and charge order occur at the same temperature.

1.2 $Bi_2Sr_2CoO_{6+\delta}$

In this thesis, we have studied the magnetic properties of $Bi_2Sr_2CoO_{6+\delta}$ as a function of the oxygen content, δ. Initial work on $Bi_2Sr_2CoO_{6+\delta}$ by Tarascon and co-workers in 1989 was focused on studying the effects on the structure and properties of the High-T_c cuprate $Bi_2Sr_2CuO_{6+\delta}$ upon substitution of magnetic Co for Cu.[12] Although the structure of $Bi_2Sr_2CoO_{6+\delta}$ was found to be nearly identical to its High-T_c precursor, measurements of the temperature dependent conductivity showed that $Bi_2Sr_2CoO_{6+\delta}$ remained insulating for all values of δ.

The crystal structure of $Bi_2Sr_2CoO_{6+\delta}$ is shown in Figure 1-2. $Bi_2Sr_2CoO_{6+\delta}$ has a layered structure, consisting of sheets of Co-O, Sr-O and Bi-O. The cobalt ions in the Co-O sheet form a nearly square array, with each positive cobalt ion surrounded by an elongated octahedron of negatively charged oxygen ions. An orthorhombic distortion along an axis 45° to the cobalt-oxygen bond breaks the in-plane symmetry in the Co-O layers. The orthorhombic axes, with $a \sim b \sim 5.45$ $\AA$ and c ~ 23.6 $\AA$ are indicated in Figure 1-2. In one unit cell, there are two Co-O layers, each separated by two Bi-O and two Sr-O layers.

A long wavelength structural modulation results from the insertion of an extra row of oxygen atoms for every 8 rows of Bi atoms in the Bi-O layer.[12] As a result of the extra row of oxygen, the formula unit of $Bi_2Sr_2CoO_{6+\delta}$ is $Bi_2Sr_2CoO_{6.25}$ and any additional oxygen at interstitial sites results in a $\delta > 0.25$.

The structural modulation results in a four-fold increase of the unit cell along the orthorhombic a-axis, which is indicated in the projection view of the crystal structure along **b** shown in Figure 1-2. The amplitude of the distortion along **c** in the Co-O sheet is about 1 $\AA$ from its equilibrium position.

In this thesis, we have referenced all of the neutron data to the orthorhombic sub-cell, with the lattice parameters indicated above. The long wavelength distortion along the a-axis results in super-lattice reflections in the neutron diffraction pattern; however, most of our measurements are conducted with the a-axis out of the scattering plane, so that we do not observe these reflections.

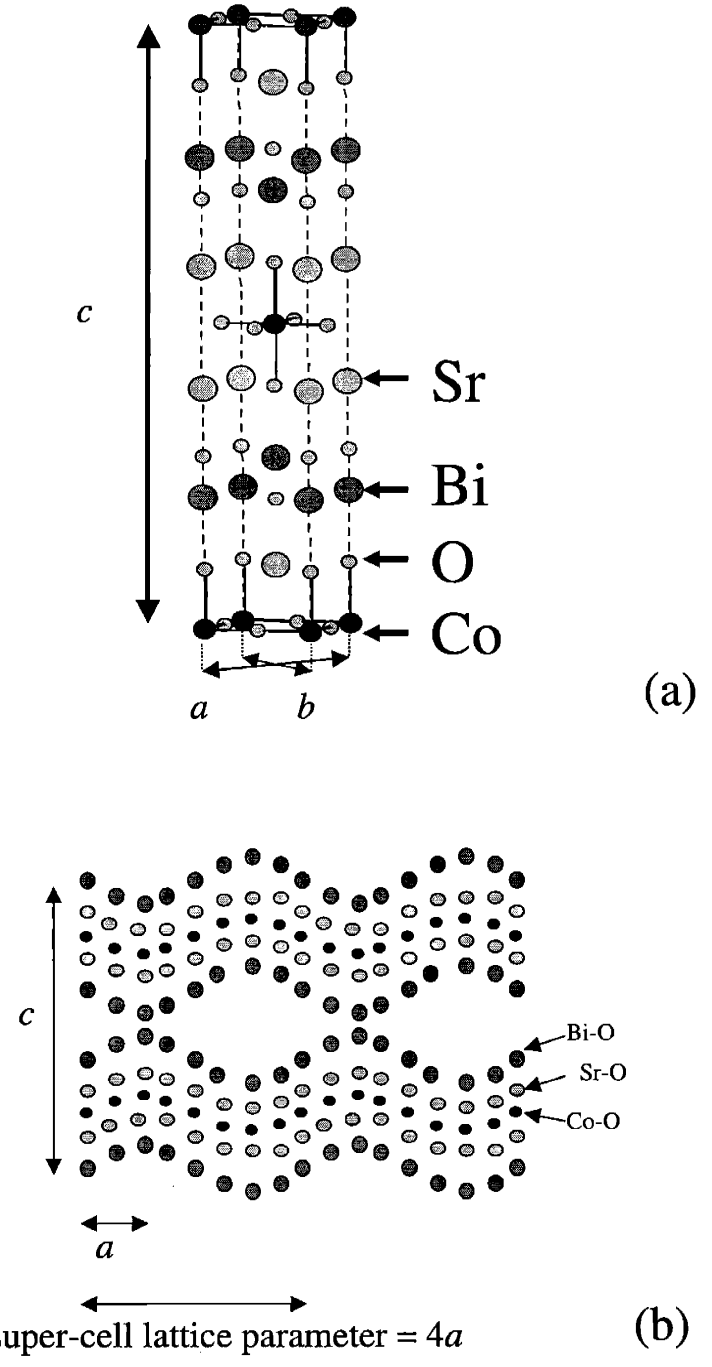

Figure 1-2: (a) Crystal structure of $Bi_2Sr_2CoO_{6+\delta}$, indicating the orthorhombic a, b, and c axes. The structural modulation of the oxide layers along **a** is not shown. (b) Projection of the structure along the b-axis, indicating the structural modulation along **a**, which results in a four-fold increase in the unit cell. The oxygen atoms are not shown for clarity. The orthorhombic sub-cell lattice constant, a, is indicated, as is the true unit-cell lattice constant, $4a$. Adjacent Co atoms in this projection view are actually displaced from one another by $b/2$.

1.3 Magnetic properties of Co

In order to understand why the magnetic properties in $Bi_2Sr_2CoO_{6+\delta}$ change with the oxygen content, we need to look at the local magnetic properties of Co. Co is a transition metal in the iron series, which is found in the fourth row of the periodic table. Oxides based on elements from the iron series derive their magnetic properties from the unfilled $3d$ shells of the transition metal ion. The electrons in the outer-most $3d$ orbitals are unshielded from the strong electric field of the surrounding negative ions. This crystal-field breaks the degeneracy of the electron levels in the $3d$ shell. When the metal ion is surrounded by an octahedron of oxygen ions, the $3d$ levels split into the triply degenerate t_{2g} and doubly degenerate e_g levels (see Figure 1-3). The high lying e_g orbitals have lobes along the bond axes between the metal and oxygen ions and thus feel the repulsive force of the negative oxygen more strongly than the t_{2g} orbitals, which have lobes in between the bond axes. A tetragonal distortion of the octahedron along the z-axis further breaks the degeneracy of the e_g and t_{2g} levels. The t_{2g} levels split into the doubly degenerate xz and yz orbitals and the non-degenerate xy orbital. The e_g levels split into the $3z^2 - r^2$ and $x^2 - y^2$ orbitals.

The crystal-field quenches the orbital angular momentum of the electrons on the metal ion: the t_{2g} and e_g orbitals have $\langle l \rangle = 0$. Thus, the magnetic moment on the cation is due entirely to the total electron spin. The total electron spin depends, in turn, on the lowest energy configuration of the electrons in the $3d$ orbitals. The crystal-field splitting favors filling first the low-energy t_{2g} levels with electrons, while the interaction between electrons, the exchange energy, favors a configuration with electrons in spatially orthogonal orbitals. Therefore, it is the balance between the crystal-field and electron-electron exchange which determines the local spin on the magnetic ion. If the crystal-field splitting is small relative to the exchange energy, the electrons will minimize their total energy by filling distinct orbitals. If the crystal-field is large compared to the electron exchange, the electrons will completely fill the t_{2g} orbitals, each orbital having two electrons with opposite spin, before elevating an electron to the e_g levels. The former maximizes the total spin, while the latter minimizes the total spin.

Co^{2+} with seven electrons in the $3d$ shell, may be in either a high-spin state, with S = 3/2 or a low-spin state, with S = 1/2. The former corresponds to six electrons in the t_{2g} orbitals and one electron in the e_g orbital, while the latter corresponds to five electrons in

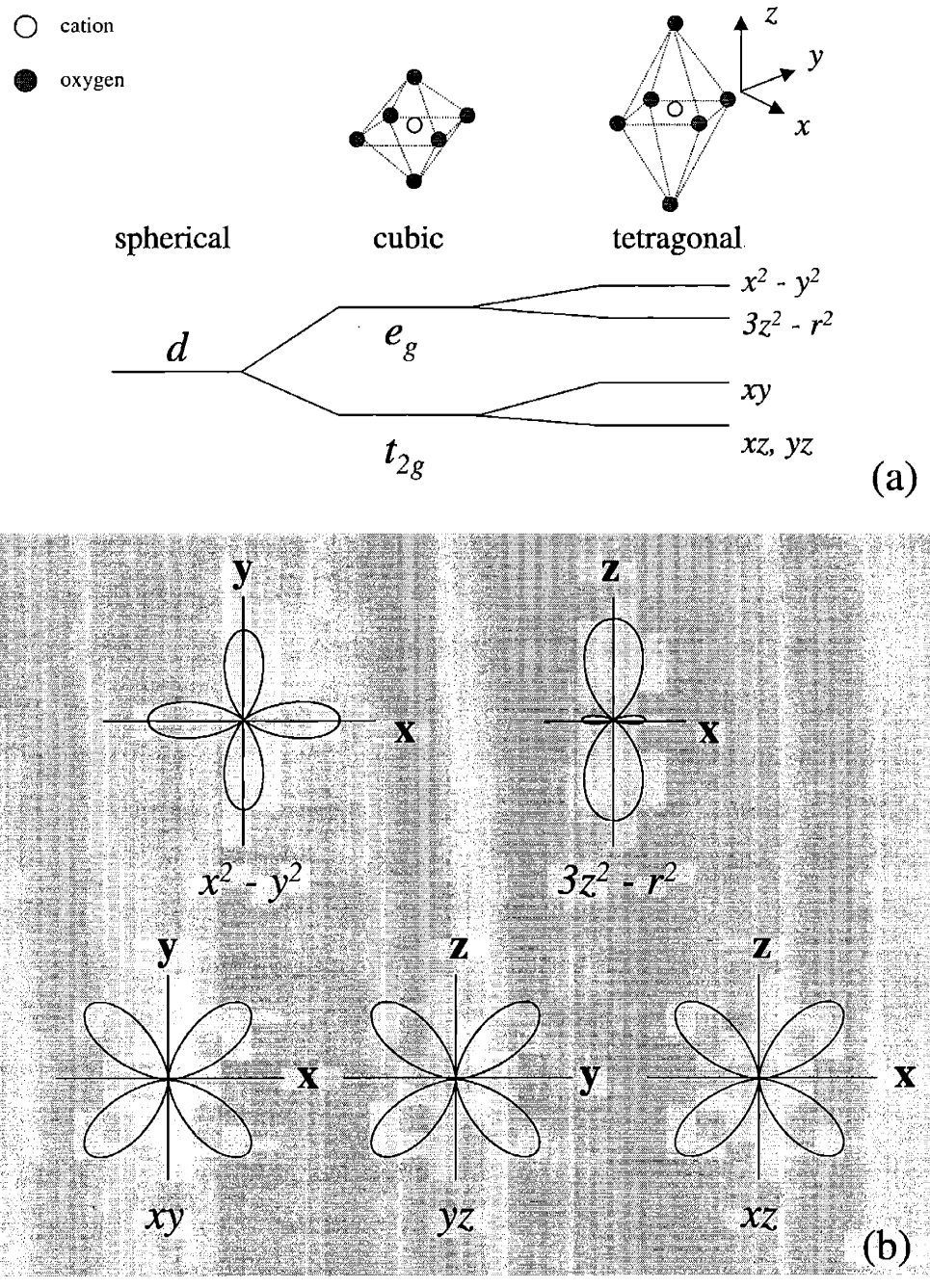

Figure 1-3: (a) Crystal-field splitting of the $3d$-orbitals surrounded by an octahedron of oxygen ions. If the oxygen-cation bonds are equal in all three directions, the crystal-field symmetry is cubic and the d-orbitals split into the triply degenerate t_{2g} orbitals and the doubly degenerate e_g orbitals. A tetragonal distortion along one of the oxygen-cation bond directions further splits the t_{2g} and e_g orbitals. (b) The two-dimensional representations of the $3d$ orbitals split by an octahedral crystal-field are shown as polar plots. The metal-oxygen bond directions are along x, y and z.

the t_{2g} orbitals and two electrons in the e_g orbitals. With one less electron, Co^{3+} may be in the high-spin state with S = 2, the intermediate spin-state with S = 1, or the low-spin state with S = 0. There is, in fact, a very delicate balance between the crystal-field energy and the exchange energy in Co oxides and the low-spin and high-spin states may lay close in energy.[7] The spin on Co is therefore very sensitive to the crystal environment. This is in contrast to the behavior observed in the manganites, in which the Mn ions always prefer the high-spin state.

1.4 Effects of changing oxygen in $Bi_2Sr_2CoO_{6+\delta}$

The valence, and hence the spin, on the Co ion in $Bi_2Sr_2CoO_{6+\delta}$ depends directly on the oxygen content. Bi and Sr prefer an oxidation state of 3+ and 2+, respectively, while the strongly electronegative oxygen is 2^-. In the limit that $\delta = 0$, all of the Co is 2+. Addition of oxygen will raise the average valence on Co and in the limit that $\delta = 0.5$, all of the Co will be 3+. We can therefore relate the Co^{2+} fraction to the oxygen content δ: if n is the number of Co^{2+} sites, then $n = 1 - 2\delta$. A mixed valence state will be obtained when the oxygen content is found to be between 6.0 and 6.5.

Experimentally, we find that the oxygen content is only tunable within the range 6.25 to 6.5. The lower limit is fixed by the structural composition of $Bi_2Sr_2CoO_{6+\delta}$, which has 25 oxygen atoms for every 8 Bi atoms. This results from the insertion of an extra row of oxygen in the Bi-O layer. However, oxygen can be added interstitially, with an experimentally determined upper limit close to $\delta = 0.5$.

As-grown crystals are typically oxygen rich, with $\delta > 0.4$. By annealing as-grown crystals in vacuum or in oxygen, it is possible to prepare samples which have $0.25 \leq \delta \leq 0.5$. It follows that we are able to explore the magnetic properties between the composition with equal amounts of Co^{2+} and Co^{3+} ($\delta = 0.25$) and the composition with 100 % Co^{3+} ($\delta = 0.5$).

The above arguments rest on two assumptions. The first is that all of the oxygen is compensated by the oxidation of Co and not by the further oxidation of Bi^{3+} to Bi^{5+}. In Reference [12], the authors cite photo-emission measurements and band-structure calculations that suggest Bi only adopts the 3+ oxidation state. Furthermore, chemical analysis of the valence of Bi and Cu in the cuprate $Bi_{2.05}Sr_{1.9}Ca_{1.05}Cu_2O_{8+\delta}$ shows that changing

the oxygen content from 0.01 to 0.18 results in a change in the average Cu valence from 1.92 to 2.09, while the average Bi valence of 3.1 changes less than 1%.[13]

The other assumption is that every additional oxygen results in two holes in the Co oxide layer. We do not have direct evidence, for example, that the composition with $\delta = 0.25$ has an exactly equal number of Co^{2+} and Co^{3+} sites. Measurements of the Cu valence as a function of oxygen in the Bi-based cuprates indicates that the valence increase of Cu is less than 2:1 in the addition of oxygen at interstitial sites.[14] However, the oxidation potential of Co^{2+} to Co^{3+} is smaller than Cu^{2+} to Cu^{3+}, so that our samples may show a greater fraction of Co in the high oxidation state. In addition, our confidence in this assumption lies in the magnetic properties, which show dramatic changes in the magnetic interactions between the cobalt spins when the oxygen level is increased or decreased.

1.5 Magnetic interactions: super-exchange and double-exchange

The interactions which result in the magnetic ordering of spins in a solid result primarily from electron-electron interactions. True magnetic dipolar interactions between electron spins are very weak ($\sim \mu$eV) and are only significant in the absence of electronic interactions. To see how electronic interactions determine magnetic properties, two mechanism for magnetic interaction, super-exchange and double-exchange, are shown in Figure 1-4. These interactions are relevant to the magnetism in $Bi_2Sr_2CoO_{6+\delta}$ so I will explain them briefly here.

Figure 1-4(a) shows a Cu-O-Cu bond in which the x^2-y^2 orbital is half-filled on each Cu site and the bonding p_x orbital is completely filled on the oxygen site, as found in undoped La_2CuO_4. This localized picture is a limiting case of the Hubbard model in which the on-site repulsion between electrons, U, is much greater than the hopping integral, t. The electrons therefore prefer to sit on different Cu sites. However, excitations occur in which the electrons on the oxygen spread out onto the neighboring Cu. Since the Pauli exclusion principle forbids double occupancy of the same quantum state by two electrons, an electron on the oxygen p-orbital can only hop to the neighboring Cu site if its spin is anti-parallel to the spin on the Cu site. This antiferromagnetic interaction between the spins on the oxygen and the copper sites mediates an effective "super-exchange" antiferromagnetic interaction between the copper spins. The effective antiferromagnetic interaction between neighboring

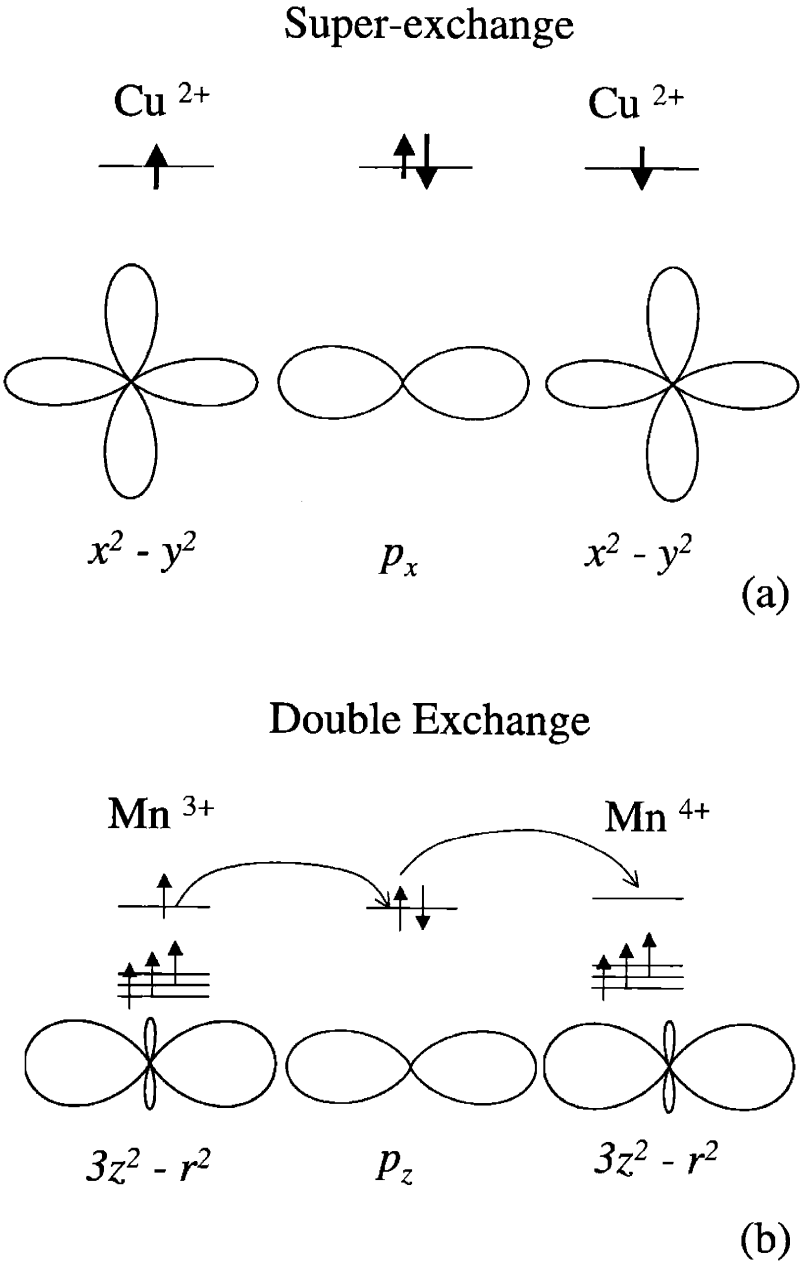

Figure 1-4: (a) Super-exchange occurs between localized spins in half-filled orbitals which have a direct overlap with the bonding oxygen orbital. The diagram shows the specific case of the half-filled $x^2 - y^2$ orbitals on Cu^{2+} cations, bridged by an oxygen p_x orbital. (b) Double-exchange between Mn^{3+} and Mn^{4+} cations is mediated by the delocalized electron in the e_g orbital.

spins S on the Cu^{2+} sites is contained in the spin Hamiltonian,

$$H_{AF} = \sum_{i,j} J_{AF} S_i \cdot S_j$$

The sum is over all nearest-neighbor spins and J_{AF} is positive since the spins minimize their energy when they are antiparallel. In La_2CuO_4, the exchange J_{AF} between nearest-neighbor Cu spin in the plane is much greater than the exchange between Cu spins in adjacent layers, resulting in predominantly two-dimensional magnetic behavior.

The ferromagnetic interaction between neighboring Mn^{3+} and Mn^{4+} ions in the hole-doped manganites is explained qualitatively by the double-exchange interaction. Figure 1-4(b) shows neighboring Mn^{3+}, with one electron in the e_g orbitals, and Mn^{4+}, with empty e_g orbitals, separated by a bridging oxygen. Double-exchange is a two-step process by which the electron on the Mn^{3+} hops to the oxygen site at the same time that an electron hops from the oxygen to the empty orbital on the Mn^{4+}. The transfer of the e_g electron in the process Mn^{3+}-O-Mn^{4+} $\rightarrow$ Mn^{4+}-O-Mn^{3+} costs zero energy, provided that the spins in the t_{2g} levels on neighboring Mn sites are parallel to each other. This is because of the large ferromagnetic exchange between the e_g and t_{2g} electrons on the same site (the Hund's coupling J_H). Since the ferromagnetic interaction in the double-exchange model results from the delocalized e_g electron, double-exchange is associated with metallic behavior. The ferromagnetic double-exchange interaction is described by the following spin Hamiltonian,

$$H_{FM} = \sum_{i,j} -J_{FM} S_i \cdot S_j \tag{1.1}$$

The minus sign in front of a positive J_{FM} indicates that neighboring spins lower their energy when they are parallel to one another.

1.6 Phase separation in transition metal oxides

In the study of the manganites, there is growing theoretical interest in the tendency toward phase separation between different electronic and magnetic phases.[1, 15] Calculations indicate that certain hole densities are unstable, resulting in phase separation into regions with different density, x. These distinct regions are necessarily microscopic, since large scale electronic phase separation is prevented by long-range Coulomb interactions.

There is considerable experimental evidence for phase separation in the manganites. For example, neutron scattering indicates the presence of distinct magnetic phases at $x = 0.5$, which is at the phase boundary between the ferromagnetic, metallic phase and the charge-ordered insulating phase.[16] Similarly, electron diffraction techniques indicate the existence of charge-ordered regions within the ferromagnetic background of $La_{5/8-y}Pr_yCa_{3/8}MnO_3$.[17]

Co-existence of distinct electronic phases in the manganites may explain the large magneto-resistance observed at T_c. The large MR occurs because the paramagnetic phase above T_c is insulating, while below T_c the ferromagnetic phase is metallic. The competition between insulating and conducting phases may explain why the system never becomes metallic above T_c.

There is substantial evidence for the presence of electronic inhomogeneities in the cuprates, as well. In strontium and oxygen doped $La_{2-x}Sr_xCuO_4$, neutron scattering measurements reveal antiferromagnetic order, characteristic of the hole-free state, well below the transition temperature to the superconducting state.[18, 19] The antiferromagnetic regions are believed to occur in the vicinity of the vortex cores of the superconductor. The re-emergence of antiferromagnetic correlations above $x = 0.05$ has been modeled as the formation of "stripe" phases in which the conducting holes are expelled from an antiferromagnetic region. The extra holes form rivers of charge, separating regions of undoped antiferromagnet.

In the Bi-based cuprates, tunneling measurements indicate inhomogeneities in the local density of states as the STM tip is scanned over the surface. A "checkerboard" pattern of quasi-particle states, which is perhaps related to the stripe phases found in $La_{2-x}Sr_xCuO_4$, is observed in the vicinity of the vortex cores in superconducting $Bi_2Sr_2CaCu_2O_{8+\delta}$.[20]

There has been little evidence for magnetic or electronic phase separation occurring in the cobalt-oxides. One exception may be $La_{1-x}Sr_xCoO_3$, where recent susceptibility and electron diffraction results suggest electronic phase separation. [8, 21, 22] In $La_{1-x}Sr_xCoO_3$, hole-rich FM clusters form near the Sr ions and leave behind a hole poor matrix with $LaCoO_3$ character.

The formation of distinct phases with different hole densities is limited by long range Coulomb interactions. However, when compounds are doped with oxygen, electronic phase separation may be accommodated by oxygen inhomogeneity. We believe that the presence of *microscopic* inhomogeneities of the oxygen content accommodate the formation of distinct

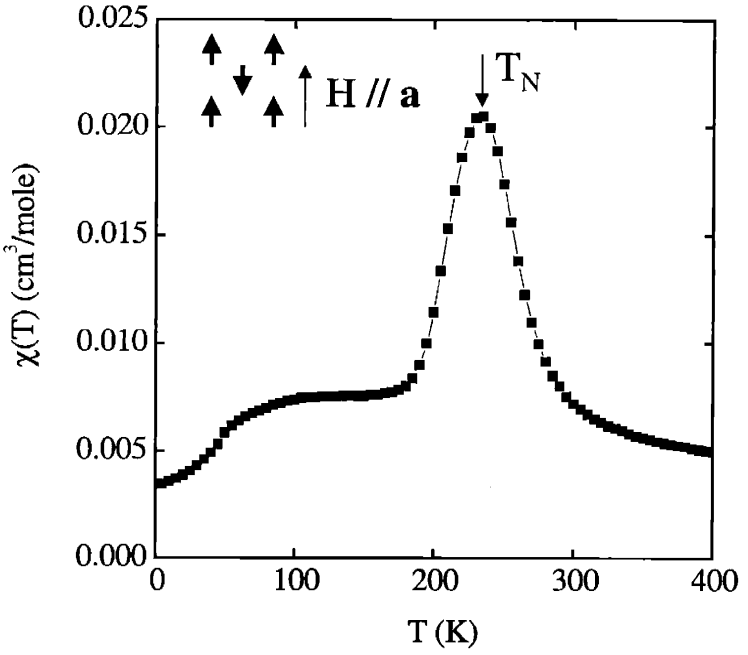

Figure 1-5: The susceptibility in an as-grown sample of $Bi_2Sr_2CoO_{6+\delta}$. The field is applied along the orthorhombic a-axis, which is the direction of the spins below the antiferromagnetic transition temperature, T_N. The susceptibility shows a large ferromagnetic-like peak at T_N. Since the field is applied along the spin direction, a canting model can not explain the observed ferromagnetic-like peak.

phases with different hole densities in $Bi_2Sr_2CoO_{6+\delta}$.

In this thesis, we studied the magnetic properties of oxygen doped $Bi_2Sr_2CoO_{6+\delta}$ in the range $0.25 \leq \delta \leq 0.5$. $Bi_2Sr_2CoO_{6+\delta}$ with $\delta = 0.5$ is an antiferromagnet below $T_N \sim 250$ K with a sub-lattice magnetization of S = 1. However, the susceptibility shows a large ferromagnetic peak at the transition to antiferromagnetic order when the field is along the a-axis (See Figure 1-5). When $Bi_2Sr_2CoO_{6+\delta}$ was first studied, the spin direction was wrongly determined to be along the b-axis.[12] The susceptibility was therefore attributed to a canting of the spins along **a**. In this thesis, we have found that the spins in the antiferromagnetic phase are directed along the a-axis. Thus, the ferromagnetic-like peak can not be explained by a simple canting model. More importantly, the ferromagnetic-like peak is enhanced when antiferromagnetic ordering is suppressed by the removal of oxygen. This indicates that the peak is not intrinsic to the antiferromagnetic order.

Using neutron diffraction techniques, we have characterized the magnetic behavior of $Bi_2Sr_2CoO_{6+\delta}$, focusing, in particular, on the enhancement of the ferromagnetism as the oxygen content, δ, is decreased from $\delta > 0.4$ to $\delta \sim 0.25$. We find that the ferromagnetic peak

grows rapidly in magnitude as the oxygen content is reduced toward $\delta = 0.25$. In addition, we find that application of a magnetic field along **a** results in a large uniform moment above a critical field H_c. We show evidence that the ferromagnetic susceptibility and field induced uniform moment result from ferromagnetic clusters within the antiferromagnet. The clusters grow larger when oxygen is removed from the crystal and dominate the magnetic behavior in samples in which T_N is reduced below $\sim$ 100 K. In the limiting case that $\delta = 0.25$, the samples are completely ferromagnetic.

To explain the observation of distinct magnetic regions, we argue that phase separation into domains which are hole rich (mostly Co^{3+}) and domains which are hole poor (equal numbers of Co^{2+} and Co^{3+}) occurs at intermediate doping, $0.25 < \delta < 0.5$. Phase separation into hole rich and hole poor regions at high temperatures is presumably allowed by mobile oxygen, for which an miscibility gap between the $\delta = 0.5$ and $\delta = 0.25$ compositions may exist. In addition, we suggest that the FM phase is a charge-ordered checkerboard structure with alternating Co^{3+} and Co^{2+} ions.

The arguments for phase separation are based not only on the observation of magnetically distinct phases, but on the observation of an irreversibility in the addition of oxygen. Annealing studies suggest that the removal of oxygen is not reversible, unless the samples are annealed at high temperature in oxygen.

An additional finding of this work is that the distinct phases interact. Evidence for this can be found in the field dependence, which shows dramatic changes in the magnetic structure in both phases occurring at the same field. We have developed a microscopic model which describes the interaction. As we show, this model can be mapped onto a form of the two-dimensional random-field Ising model.

1.7 Structure of this thesis

This thesis is divided into five chapters. Chapter 2 explains the theory and experimental details related to the neutron diffraction technique. Chapter 3 discusses sample preparation, namely characterization of the oxygen content and the details of measuring the bulk susceptibility and resistivity. Chapter 4 is a long chapter presenting the experimental results in three sections. Prior to the work in this thesis, there has been little characterization of the magnetic properties in $Bi_2Sr_2CoO_{6+\delta}$ using neutron diffraction techniques. Therefore,

Chapter 4 describes the various magnetic phases in $Bi_2Sr_2CoO_{6+\delta}$ in detail. In Section 4.1, we show how the structure of the AF Co^{3+} phase is determined using neutron scattering and discuss the susceptibility. In Section 4.2, we discuss the ferromagnetic behavior in samples with $\delta \sim 0.25$. We also present evidence for charge ordering in these samples. In Section 4.3, we look at samples with $0.25 < \delta < 0.5$ and present evidence for phase separation. In Chapter 5, results from oxygen annealing measurements of $Bi_2Sr_2CoO_{6+\delta}$ samples are presented. These results indicate that the signature of phase separation, namely the presence of ferromagnetic clusters, is only seen when samples are annealed in oxygen at high temperatures. Finally, in Chapter 6, we develop a microscopic model for the magnetic interactions occurring at all values of δ.

Chapter 2

Neutron Diffraction

2.1 Overview

Neutron diffraction measurements were performed on single crystals of $Bi_2Sr_2CoO_{6+\delta}$ to probe the magnetic properties as a function of δ. An analysis of the diffraction peaks allowed us to determine the magnetic structure, the size of the ordered moment in the magnetically ordered state and the effective length scale of magnetically correlated regions. In addition, neutron diffraction measurements were performed to look for distortions in the crystal structure resulting from charge ordering.

The purpose of this chapter is to explain the basic theory of neutron diffraction and describe the technique for measuring diffraction peaks. The chapter is organized as follows. Section 2.2 is a brief introduction to the properties of thermal neutrons. In Section 2.3, the cross-sections for nuclear and magnetic diffraction are calculated. In Section 2.4, the magnetic cross-section is extended to include polarized neutron scattering. The experimental details of the triple-axis spectrometer are presented in Sections 2.5-2.7. Finally, in Section 2.8, I show a sample calculation of the local moment in a magnetically ordered crystal.

I have tried to keep the presentation very basic and I have included only those formulas which I felt were necessary for understanding the final results. A very complete derivation of the neutron scattering cross-section is given in Squires [23] and most of what that I include here is based on this text. Other good overviews are given in References [24, 25, 26].

2.2 Properties of thermal neutrons

The neutrons generated in an experimental reactor have an average energy of 2 MeV. These neutrons are thermalized with a 300-400 K moderator which slows the neutrons down to an energy range of 5-100 meV. The de Broglie wavelength of thermal neutrons is therefore 1-3 $\AA$, which is comparable to the spacing between atoms in a solid.

There are two primary interactions via which neutrons scatter from the atoms in a solid. The first interaction is the nuclear strong-force, which results in scattering from the atomic nuclei in a solid. The second interaction is a magnetic interaction between the neutron spin and the magnetic field resulting from the atomic spin and orbital angular momentum. Thus neutron scattering techniques may be applied to the study of both structural and magnetic order. Since the neutron has no charge, it penetrates deeply into materials, probing bulk properties. This is in contrast to x-rays and electrons, which interact strongly with the electrons in a solid and only penetrate 1-10 μm into a material. The energy of thermal neutrons is comparable to the structural and magnetic excitation energies in condensed matter systems. When a neutron is inelastically scattered by a phonon or magnon, the change in energy is comparable to the incident neutron energy and thus easily measured. Finally, it should be noted that the amplitudes for neutron scattering from the atomic nuclei are uncorrelated with the atoms' positions in the periodic table. As a consequence, light atoms such as oxygen and hydrogen, which are practically invisible to x-rays, are fairly strong scatterers of neutrons. In the study of transition metal oxides, where the positions and dynamics of the oxygen ions determine many of the interesting magnetic properties, neutron scattering plays a fundamental role.[27, 28]

Neutron *diffraction* is an elastic scattering process which results from the coherent scattering of the periodic nuclei and magnetic moments in a solid. Diffraction is described phenomenologically by Bragg's Law in which the atomic planes in a crystal are treated as "mirror" surfaces.(see Figure 2-1) When a neutron with wavelength λ is incident on the crystal, each atomic plane partially reflects and partially transmits the wave. For constructive interference to occur between the reflected waves of two adjacent atomic layers separated by lattice spacing d, the difference in the waves' path length, $2d\sin(\theta)$, must be an integer multiple of wavelengths:

$$2d\sin\theta = n\lambda \tag{2.1}$$

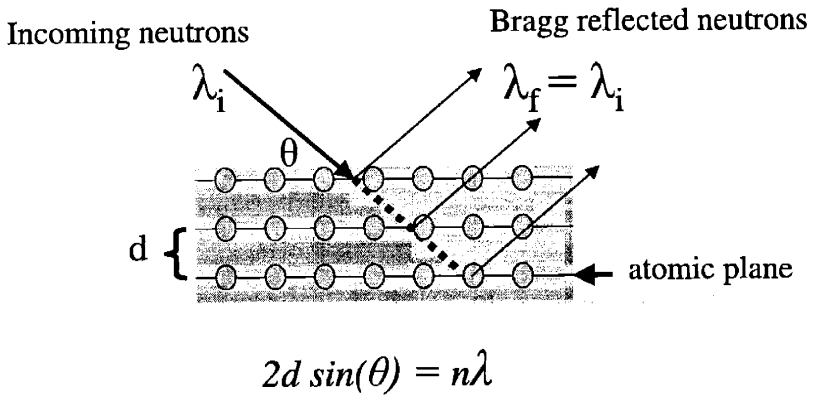

Figure 2-1: Bragg's law describes coherent, elastic scattering of x-rays or neutrons from the atomic planes of a crystal. If the atomic planes are separated by a lattice spacing d, then reflected waves from adjacent layers will be in phase when the difference in the waves' path length, $2d\sin(\theta)$, is equal to an integral number of wavelengths.

By fixing λ and scanning in θ, it is possible to determine the periodicity of the nuclei in a solid. A diffraction measurement therefore functions as an atomic scale microscope. More importantly, neutron diffraction functions as a *magnetic* microscope, since the technique can be applied to measuring the periodicity of magnetically ordered materials.

2.3 The scattering cross-section

Although Bragg's law predicts the scattering condition correctly, it does not provide a recipe for calculating the scattering amplitude. In this section, we will calculate the cross-section for elastic, coherent scattering. The scattering condition is the same as Bragg's Law, but we will show that the amplitudes depend on the local nuclear and magnetic structure of the atoms in the scattering system.

In a scattering measurement, we are interested in measuring the probability that a neutron with initial wave vector k_i and energy E_i, will scatter from the system under study into a final state with wave vector k_f and E_f. In this way, we can extract information on the positions and dynamics of the atoms in the system. The *partial differential cross-section*, $\frac{d\sigma}{d\Omega dE_f}$ is the probability that the system under study will scatter a neutron into a cone

with solid angle $d\Omega$ about k_f and in the energy window dE_f about $E_f = E_i + \hbar\omega$. For concreteness, we might imagine that a detector sits at Ω and measures the final neutron energy, E_f within an energy window dE_f. We denote the initial and final states of the scattering system by s_i and s_f. The cross-section is proportional to the transition rate of the process k_i to k_f, which is given by Fermi's Golden Rule

$$Rate(\mathbf{k_i} \rightarrow \mathbf{k_f}) = \frac{2\pi}{\hbar} \mid \langle k_f s_f \mid V_{int} \mid k_i s_i \rangle \mid^2 \delta(\Delta E_{system} + \hbar\omega) \tag{2.2}$$

The potential V_{int} is the total potential due to the interaction of the neutron with the N molecules which make up the scattering system,

$$V = \sum_j V_j(\mathbf{r} - \mathbf{R_j}) \tag{2.3}$$

$\mathbf{R}_j$ is the coordinate of the j^{th} site and $\mathbf{r}$ is the neutron position. If the interaction is weak, then the scattered wave may be approximated by a plane-wave of the form $e^{i\mathbf{k_f}\cdot\mathbf{r}}$. Therefore, the expectation value in Eq. 2.2, integrated over the neutron coordinates, is just a Fourier transform of the single site potential V:

$$\mid \langle s_f \mid \sum_j V_j(\mathbf{Q}) \exp(i\mathbf{Q}\cdot\mathbf{R_j}) \mid s_i \rangle \mid^2 \delta(\Delta E_{system} + \hbar\omega) \tag{2.4}$$

In Eq. 2.4, $\mathbf{Q} = \mathbf{k}_f$ - $\mathbf{k}_i$ is the scattering vector and $V_j(\mathbf{Q})$ is the Qth component of the Fourier transform of the potential at site j. In fact, the expression in 2.4 is quite general and can be used to describe all (weak) scattering processes in which the incident wave vector changes from k_i to k_f. The physics describing a *particular* system lies in the expectation value in Eq. 2.4, which depends on the space and time coordinates of the N particles in the scattering system as well as the interaction term, $V_j(\mathbf{Q})$. For this reason, Eq. 2.4 is deceptively compact. Van Hove showed that an equivalent way of writing Eq. 2.4 is,

$$\frac{d\sigma}{d\Omega dE_f} = N\frac{k_f}{k_i}(\frac{m}{2\pi\hbar^2})^2 S(\mathbf{Q},\omega) \tag{2.5}$$

$$S(\mathbf{Q},\omega) = \frac{1}{2\pi\hbar N}\sum_{jj'} V_j(\mathbf{Q})V_{j'}^*(\mathbf{Q}) \int_{-\infty}^{\infty} \langle e^{-i\mathbf{Q}\cdot(\mathbf{R_j(t)}-\mathbf{R_{j'}(0)})}\rangle e^{-i\omega t} dt d\mathbf{r} \tag{2.6}$$

In 2.6, the expectation value is a thermal average over the initial state of the scattering system. In this form, we see that the scattering amplitude is proportional to the space and time Fourier transform of the correlation between particles.

Eq. 2.6 can be separated into a *coherent* and an *incoherent* part,

$$S(\mathbf{Q},\omega) = S_{coh}(\mathbf{Q},\omega) + S_{inc}(\mathbf{Q},\omega) \tag{2.7}$$

$$S_{coh}(\mathbf{Q},\omega) = \frac{1}{2\pi\hbar N}\sum_{jj'}\overline{V_j(\mathbf{Q})}\;\overline{V_{j'}^*(\mathbf{Q})}\int_{-\infty}^{\infty}\langle e^{-iQ\cdot(R_j(t)-R_{j'}(0))}\rangle e^{-i\omega t}dt \tag{2.8}$$

$$S_{inc}(\mathbf{Q},\omega) = \frac{1}{2\pi\hbar N}\sum_{j}(\overline{V_j^2(\mathbf{Q})} - \overline{V_j(\mathbf{Q})}^2\int_{-\infty}^{\infty}\langle e^{-iQ\cdot R_j(t)}\rangle e^{-i\omega t}dt \tag{2.9}$$

The coherent cross-section depends on the correlation between different sites, at the same time and at different times, and as we will see, it is the part of the cross-section which describes interference between waves scattered from different atoms. The incoherent cross-section depends only on the deviations from the average potential at a single site and typically results in Q-independent scattering. A good way to think about the incoherent contribution is as a "correction" for having assumed that the neutron sees the same (average) potential at each site.

Let us now consider the form of $S_{coh}(\mathbf{Q},\omega)$ for elastic ($\omega = 0$) scattering from a crystal with N atoms at *fixed* positions $\mathbf{l_j}$ and the same potential $V(\mathbf{Q})$ at each site. This corresponds to taking the limit t $\rightarrow \infty$ in the scattering amplitude,

$$S(\mathbf{Q},\omega)_{coh} = \overline{V(\mathbf{Q})}^2\sum_{jj'}\frac{1}{N}\left\langle e^{-iQ\cdot(R_j(\infty)-R_{j'}(0))}\right\rangle\delta(\hbar\omega) \tag{2.10}$$

$$= \overline{V(\mathbf{Q})}^2\sum_{j}\left\langle e^{iQ\cdot l_j}\right\rangle\delta(\hbar\omega) \tag{2.11}$$

The above states that in the limit of infinite time, the positions of the atoms in a crystal are uncorrelated. Of course, in an artificial crystal in which the atoms are fixed, the atomic positions are always uncorrelated; however, in a real crystal, the atoms jiggle around their equilibrium positions and the position of an atom is given by $\mathbf{R}_j(t) = \mathbf{l}_j + \mathbf{u}_j(t)$, where $\mathbf{l_j}$ is the equilibrium position of site j and $\mathbf{u}_j$(t) is the displacement from that position. If we

assume these displacements are small ($Q \cdot u_j << 1$), then,

$$e^{i\mathbf{Q}\cdot R_j} = e^{i\mathbf{Q}\cdot l_j} e^{i\mathbf{Q}\cdot u_j(t)} \tag{2.12}$$

$$= e^{i\mathbf{Q}\cdot l_j}(1 + i\mathbf{Q}\cdot u_j(t) - 1/2(\mathbf{Q}\cdot u_j(t))^2 + ...) \tag{2.13}$$

Again taking the limit $t \to \infty$, if we now take a thermal average over Eq. 2.13, the second term will be zero because the average displacement is zero. The first order correction for the "jiggling" atoms is therefore,

$$\langle 1 - \frac{1}{2}(\mathbf{Q}\cdot u_j)^2 \rangle \simeq e^{-\frac{1}{2}(\mathbf{Q}\cdot u_j)^2} \tag{2.14}$$

$$= e^{-W} \tag{2.15}$$

This correction term is called the Debye-Waller factor. As the temperature increases, the atoms' mean displacements from their equilibrium positions grow larger and the amplitude for coherent scattering decreases. Including the Debye-Waller factor, the scattering amplitude for elastic scattering is,

$$S(\mathbf{Q},\omega)_{coh} = \overline{V(\mathbf{Q})}^2 e^{-2W} \sum_j \left\langle e^{iQ\cdot l_f} \right\rangle \delta(\hbar\omega) \tag{2.16}$$

$$= \frac{(2\pi)^3}{v_0} \overline{V(\mathbf{Q})}^2 e^{-2W} \sum_{\mathbf{G}} \delta(\mathbf{Q}-\mathbf{G})\delta(\hbar\omega) \tag{2.17}$$

where $\mathbf{G}$ is a reciprocal lattice vector. We therefore arrive at the final expression for the coherent cross-section for elastic scattering,

$$\frac{d\sigma_{coh}}{d\Omega dE_f} = N\overline{V(\mathbf{Q})}^2 e^{-2W} \sum_G \delta(\mathbf{Q}-\mathbf{G})\delta(\hbar\omega) \tag{2.18}$$

Note that the scattering condition k_f - $k_i = \mathbf{G}$ is equivalent to Bragg's Law, since

$$\mid k_f \mid = \mid k_i \mid = \frac{2\pi}{\lambda} \tag{2.19}$$

and

$$\mathbf{G} = \frac{2\pi}{d} \tag{2.20}$$

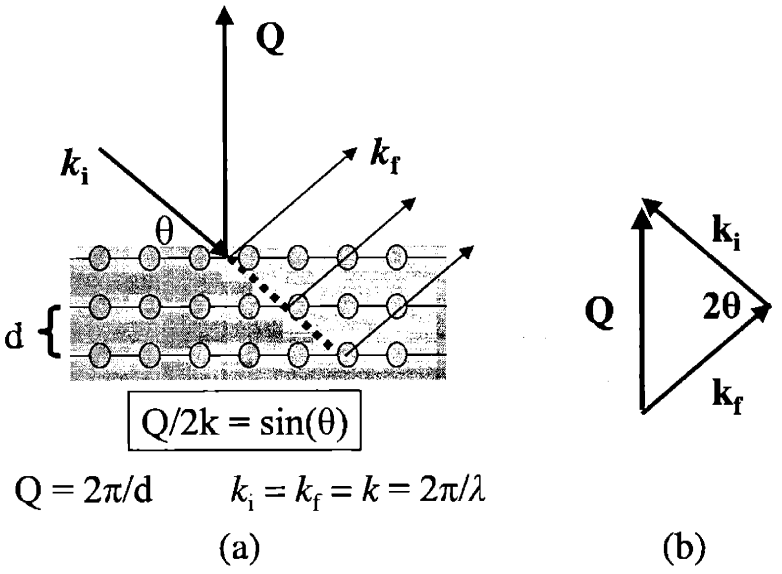

Figure 2-2: (a) The Bragg scattering condition in terms of the scattering vector **Q** and the neutron momentum, k. When the Bragg condition is satisfied, $\mathbf{Q} = \mathbf{k_f} - \mathbf{k_i}$ is equal to a reciprocal lattice vector. (b) The scattering triangle for elastic diffraction.

where d is the spacing between atomic planes stacked perpendicular to **G**. The scattering triangle is indicated in Figure 2-2.

The expression in Eq. 2.18 is for a Bravais lattice. For a non-Bravais lattice, we replace $\mathrm{V}(\mathbf{Q})e^{-W}$ with

$$F(Q) = \sum_d V_d e^{-W_d} e^{iQ \cdot R_d} \tag{2.21}$$

The sum over d is over all of the atoms in the unit cell and is called the structure factor. For some crystal structures, the sum over the scattered waves in a single unit cell may be close to zero.

2.3.1 Nuclear scattering

The neutron interacts with each of the atomic nuclei in the scattering system via the nuclear strong-force. The interaction is short range ($\sim 10^{-13}$ cm) with respect to the neutron wavelength ($\sim 10^{-8}$ cm) and the nuclear potentials can be treated as spherically symmetric δ-functions,

$$V_{nuc} = \sum_j \frac{2\pi\hbar^2}{m} b_j \delta(\mathbf{r} - \mathbf{R_j}) \tag{2.22}$$

The scattering length, b_j, is the strength of the nuclear potential at the j^{th} atom and is typically of order 1-10 $\times$ 10^{-13} cm. Although b can be complex, we will consider only the real, non-absorptive part in the cross-section. The Fourier transform of the δ-function in Eqn. 2.22 is independent of $\mathbf{Q}$ and therefore the cross-section for nuclear scattering is given by,

$$\frac{d\sigma_{coh}}{d\Omega} = \sum_j b_j^2 e^{-2W} e^{i\mathbf{Q}\cdot\mathbf{R_j}} \tag{2.23}$$

2.3.2 Magnetic scattering

The spin and orbital motion of the unpaired electrons on an atom result in a magnetic dipole field. This magnetic field is felt by the neutron spin via the dipole-dipole interaction and results in additional scattering at the magnetic atomic sites.

The neutron magnetic moment operator is given by,

$$\mu_\mathbf{N} = -\gamma\mu_N\sigma \tag{2.24}$$

where σ is the neutron spin operator with eigenvalues of +1 or -1, $\mu_N = \frac{e\hbar}{2m_n}$ is the neutron magneton number and $\gamma = 1.913$ is the gyromagnetic ratio. The total $\mathbf{B}$-field resulting from the electron spin $\mathbf{S}$ and orbital momentum $\mathbf{p}$ is,

$$\begin{aligned} \mathbf{B} &= \mathbf{B_S} + \mathbf{B_L} \\ &= \frac{\mu_0}{4\pi}\{\nabla \times (\frac{-2\mu_b \mathbf{S}\times\hat{\mathbf{R}}}{R^2}) - \frac{2\mu_b}{\hbar}\frac{\mathbf{p}\times\hat{\mathbf{R}}}{R^2}\} \end{aligned} \tag{2.25}$$

We will consider here only the spin part of Eq. 2.25.

The interaction of the neutron spin with the spin part of the B field on a single site is,

$$V_{spin} = -\mu_\mathbf{N}\cdot\mathbf{B_S} \tag{2.26}$$

The Fourier transform of the dipole interaction is much more complicated than that of the nuclei and is equal to,

$$\overline{V_{spin}(\mathbf{Q})} = (\frac{g}{2})(\gamma r_0) f(\mathbf{Q})(\sigma\cdot(\hat{\mathbf{Q}}\times(\langle\mathbf{S_j}\rangle\times\hat{\mathbf{Q}}))) \tag{2.27}$$

Here $\langle S_j \rangle$ is the average spin at site j, r_0 is the classical electron radius, $\frac{\mu_0 e^2}{4\pi m_e} = 2.818 \times 10^{-13}$ cm and $f(\mathbf{Q})$ is the Fourier transform of the normalized, unpaired spin density ($f(\mathbf{Q}) \leq 1$). For a magnetically ordered crystal, $\langle \mathbf{S_j} \rangle$ is the same for every site.

For unpolarized neutrons, the elastic-scattering cross-section is,

$$\frac{d\sigma_{coh}}{d\Omega} = \langle S_j \rangle^2 (\frac{g}{2})^2 (\gamma r_0)^2 f^2(Q)(1 - \hat{Q} \cdot \hat{S})^2 \tag{2.28}$$

Note the difference between the magnetic scattering amplitude and the amplitude for nuclear scattering: the dipole field is a long-range vector field in contrast to the short range, spherically symmetric potential of the nuclei. However, if we make a rough comparison between the cross-sections for nuclear and magnetic scattering, taking $b \sim 1 \times 10^{-12}$,

$$\frac{V^2_{spin}(Q)}{V^2_{nuc}(Q)} \sim \frac{(\gamma r_0)^2}{b^2} \sim 0.2 \tag{2.29}$$

The $\mathbf{Q}$ dependence of the magnetic cross-section appears in both the form factor, $f(\mathbf{Q})$, and the geometric factor $1 - \hat{\mathbf{Q}} \cdot \hat{\mathbf{S}}$. The form factor, $f(\mathbf{Q})$, causes the magnitude of the magnetic scattering to fall off in amplitude with respect to the nuclear scattering at higher $|Q|$. This occurs because the electron density, and hence the spin density, is not localized in space. The more spread out the electron is, the more rapidly $f(\mathbf{Q})$ falls off with increasing $|Q|$. This has a simple physical interpretation. When the wavelength of the scattering vector is large compared to the dimensions of the electron cloud, the entire electron cloud looks like a "point particle" and all parts of it scatter in phase. When the scattering vector has a wavelength similar to or less than the dimension of the electron cloud, scattering from different parts of the electron cloud are no longer in phase. The Q dependence of the form factor for magnetic scattering is in fact one of the ways to distinguish magnetic peaks from Q-independent structural peaks.

The geometric factor is a consequence of the dipolar nature of the atomic magnetic field. When the scattering vector, $\mathbf{Q}$, is parallel to the ordered spins, the scattering is zero. By changing the orientation of $\mathbf{Q}$ with respect to $\mathbf{S}$, it is possible to determine the spin direction.

2.4 Polarized neutron scattering

In the previous section, we neglected the dependence of the magnetic cross-section on the neutron's spin. However, we can extract additional information about the spin state of the ions in a magnetically ordered solid by using polarized neutrons. One reason is that the interaction between the neutron spin and the atomic magnetic field is dipolar and therefore depends on the orientation of the neutron spin with respect to the atomic spin. In addition, the neutron spin-state is not necessarily an eigenstate of the neutron-dipole interaction. To see how the spin-dependence may be exploited, we need to go back to the magnetic scattering cross-section and consider the cross-section for various neutron spin-states.

For a quantum mechanical spin, we can define the spin direction with respect to an arbitrary axis. We will take this axis to be the $\hat{z}$ direction and denote the spin-up state by $|\uparrow\rangle$ and the spin-down state by $|\downarrow\rangle$. For an unpolarized beam, the $|\uparrow\rangle$ and $|\downarrow\rangle$ states occur with equal probability. When the neutron scatters from a magnetic atom, there are four possibilities for the change in the neutron spin,

$$\begin{aligned} |\uparrow\rangle &\rightarrow |\uparrow\rangle \\ |\downarrow\rangle &\rightarrow |\downarrow\rangle \\ |\uparrow\rangle &\rightarrow |\downarrow\rangle \\ |\downarrow\rangle &\rightarrow |\uparrow\rangle \end{aligned}$$

The first two processes correspond to non-spin flip (NSF) processes, while the latter two are spin-flip (SF) processes.

The total scattering cross-section, nuclear plus magnetic, with the neutron spin-state written explicitly before and after scattering is,

$$\frac{d\sigma}{d\Omega} = \sum_{\sigma} P(\sigma_i) \mid \langle \sigma_f s_f \mid \sum_j (b_j - \sigma \cdot \mathbf{C_j}) e^{i\mathbf{Q}\cdot\mathbf{R_j}} \mid \sigma_i s_i \rangle \mid^2 \tag{2.30}$$

$$\mathbf{C_j} = \frac{g}{2}(\gamma r_0) f(\mathbf{Q})(\hat{\mathbf{Q}} \times (\langle \mathbf{S_j} \rangle \times \hat{\mathbf{Q}}) \tag{2.31}$$

In Eqn. 2.30, $\mathrm{P}(\sigma_i)$ is the probability that the spin of the neutron before scattering is σ_i. The sign convention for the nuclear term is that b is positive for a repulsive potential. The sign on the magnetic term depends on the orientation of the neutron spin with respect to

the atomic spin and is negative for an attractive potential. Carrying out the dot product in Equation 2.30 we see that we need to take the following quantum expectation value,

$$P(\sigma_i)\langle\sigma_f \mid b + \sigma_x C_x + \sigma_y C_y + \sigma_z C_z \mid \sigma_i\rangle \tag{2.32}$$

In the above expression, $P(\sigma_i) \mid \sigma_i\rangle$ is the initial state of the neutron, which is controlled by the preparation of the neutron beam. If the beam is unpolarized, then there are an equal number of $|\uparrow\rangle$ and $|\downarrow\rangle$ neutrons in the incident beam. On the left side of the expression, $\mid \sigma_f\rangle$ is the spin-state of the neutron after scattering. If the analyzer does not differentiate between up and down spins, then the sum in Eqn. 2.30 is over all possible final states $\mid \sigma_f\rangle$. On the other hand, if the analyzer accepts only spin-up neutrons, then we only need calculate the projection of $(b_j - \sigma \cdot \mathbf{C}) \mid \sigma_i\rangle$ onto the state $|\uparrow\rangle$

The effects of the σ_l operators on the neutron spin-state are summarized as follows,

$$\begin{aligned} \sigma_x |\uparrow\rangle &= |\downarrow\rangle & \sigma_x |\downarrow\rangle &= |\uparrow\rangle \\ \sigma_y |\uparrow\rangle &= i |\downarrow\rangle & \sigma_y |\downarrow\rangle &= -i |\uparrow\rangle \\ \sigma_z |\uparrow\rangle &= |\uparrow\rangle & \sigma_z |\downarrow\rangle &= - |\downarrow\rangle \end{aligned}$$

From this we see that spin-flip processes only occur when $\mathbf{C}$ has a component perpendicular to $\hat{z}$.[1] On the other hand, the non-spin-flip processes depend on the sign of the neutron spin with respect to the atomic spin. There are several important applications of these results which are relevant for the work in this thesis.

2.4.1 Half-polarized set-up and ferromagnetic scattering

The reflections resulting from ferromagnetism are at the same positions in reciprocal space as the nuclear reflections. Since magnetic reflections are generally weak with respect to the nuclear reflections, the ferromagnetic signal may only be a few percent of the total nuclear signal.

The spin dependence of the magnetic cross-section can be exploited to increase the sensitivity to ferromagnetic scattering. We will consider the case of a ferromagnet which is completely polarized (i.e. single domain). The polarization direction of the ferromagnet determines the polarization of the neutron, P, which is up or down with respect to the

[1]The scattering length also has a spin-dependent component, but this only affects the incoherent scattering.

ferromagnetic moment. For the case that $\mathbf{Q}$ is perpendicular to $\mathbf{S}$ and P, there are two spin-dependent cross sections for magnetic plus nuclear scattering,

$$\langle\uparrow| b_j + \sigma_z C_z |\uparrow\rangle = b_j - C_z \quad (2.33)$$

$$\langle\downarrow| b_j + \sigma_z C_z |\downarrow\rangle = b_j + C_z \quad (2.34)$$

The ratio of the $|\uparrow\rangle$ to the $|\downarrow\rangle$ intensity is therefore, $\frac{(b_j - C_j)^2}{(b_j + C_j)^2} = r$. For $\frac{C_j}{b_j} << 1$, $\frac{4C_j}{b_j} = 1 - r$ and this measurement provides a sensitive means of measuring the ferromagnetic scattering. This result should be compared to the unpolarized measurement for which the total intensity is $b_j^2 + C_j^2$.

The polarization of neutrons is accomplished by making use of the dependence of the cross-section on the spin-state of the neutron. For example, in the Heusler alloy Cu_2MnAl, there is nearly perfect cancellation between the nuclear and magnetic terms for one spin-polarization in the cross-section at the (1, 1, 1) reflection.

2.4.2 Full polarization analysis

Another important case is when the polarization and scattering vector are parallel to one another, but $\mathbf{Q}$ and P are perpendicular to $\mathbf{S}$. In this case, the scattering is entirely SF. Namely,

$$\langle\downarrow| b_j - \sigma \cdot C |\uparrow\rangle = -(C_x + iC_y) \quad (2.35)$$

$$\langle\downarrow| b_j - \sigma \cdot C |\uparrow\rangle = -(C_x - iC_y) \quad (2.36)$$

If a polarizer is placed before the sample and before the analyzer, both the spin-flip and non-spin flip cross-sections can be measured. Polarization analysis thus provides a sensitive means of measuring a canted moment.

2.5 The triple-axis spectrometer

All of the neutron measurements in this thesis were performed at the BT2 triple-axis spectrometer at the NIST Center for Neutron Research. This spectrometer can also be outfitted to perform polarized neutron measurements.

A schematic diagram of the triple-axis spectrometer is shown in Figure. 2-3. Neutrons

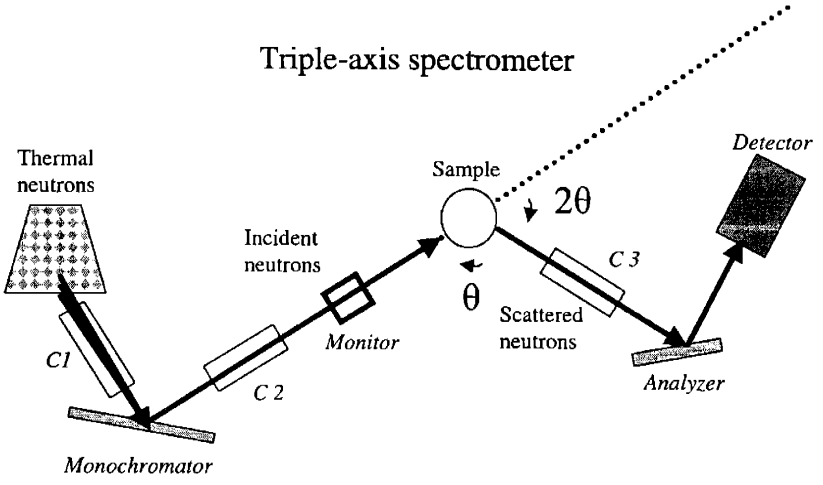

Figure 2-3: The triple-axis spectrometer viewed from above. The incident neutrons and sample to analyzer arm determine the scattering plane. Two tilt motors (not shown) rotate the sample perpendicular to the scattering plane. Once oriented with the tilts, the sample is rotated along θ through the scattering condition set by 2θ. Collimators are indicated by a C.

from the reactor are brought to thermal equilibrium with a moderator. The resulting spectrum of neutrons has a Maxwellian distribution of velocities, which is peaked at the temperature of the moderator (typically 300-400 K). The neutrons are then monochromated using the (0, 0, 2) reflection of pyrolytic graphite (PG). Pyrolytic graphite is an ideal monochromator crystal because the crystal planes are only well correlated along the c-axis, thus reducing the possibility of multiple scattering. The reflectivity of the PG at the (0, 0, 2) reflection can be as high as 90%.

The incident neutron beam and diffractometer arm determine the scattering plane. The crystal itself is then rotated on two perpendicular tilt motors until the chosen 2D cut through the crystal intersects the scattering plane. Bragg peaks are located by first setting the diffractometer arm to 2θ, where θ is the Bragg angle, and then rotating the crystal on the θ-stage. For Bragg scattering, the scattering vector bisects the incident and final wave vectors. Thus one can always look at the spectrometer to see that it is set up appropriately for the measurement of a particular reflection.

PG filters are often put in the beam path to remove the small amount of contamination from higher order reflections from the monochromator. Collimators are placed before the

monochromator (C1) and before and after the sample (C2 and C3). A collimator C4 can also be placed before the detector, though we did not do so in any of our measurements. The collimators are made of thin blades coated with Cd which slide into a grooved rectangular tube. The FWHM of the collimators at NIST are 22 minutes for every blade inserted, 41 minutes for every other blade inserted, 62 minutes for every third blade inserted and 83 minutes for every fourth blade inserted. The conventional notation for describing the collimators along the beam path is C1-C2-sample-C3-C4.

For the polarized neutron measurements, a Heusler alloy is used as the monochromator (half-polarized set-up) and as the analyzer (fully-polarized set-up). A "flipper" coil, which generates a horizontal field for a segment of the neutron beam's flight path, attaches to the spectrometer rail before the sample. The magnitude of the flipping field is chosen so that the neutron spin rotates by exactly 180 degrees during the time that it is in the horizontal field. The flipper also has a vertical compensating field, to correct for stray magnetic fields. Permanent magnets maintain the vertical field down the flight path to prevent the neutron from depolarizing.

In a polarized neutron scattering measurement, the neutron polarization P must be determined experimentally. This is done using the full polarization set-up and rotating the crystal to a sizeable Bragg reflection. The intensity with the flipper uncharged and charged is measured to obtain a flipper ratio. The flipper ratio in our measurements was typically 25-30, indicating that greater than 96% of the spins were in the polarization direction. The flipper ratio showed a decrease with field above about 1 T, so all of the polarized neutron scattering measurements were performed in 1 T or lower.

A monitor after the monochromator counts the number of neutrons per second, so that all measurements can be normalized to the monitor rate. Typical counting times for Bragg peaks are about 1 s for nuclear reflections and a few seconds for magnetic reflections. In a polarized neutron scattering measurement, the count times are slightly increased because the Heusler monochromator and analyzer reduce the intensity by about a factor of five.

The sample conditions are controlled using a He-4 cryostat with a 7 Tesla, split-coil magnet. The sample is sealed in an Al can containing He exchange gas and attached to the cold finger of the cryostat.

One important consideration when using the magnet is the tilt angles on the θ-stage. If the tilts are off by more than a degree, it is necessary to manually adjust the crystal on the

sample holder rather than using the tilts. Two problems with the magnet are encountered when the tilts exceed a few degrees. The first is the danger that the top-heavy magnet will rip out the screws attaching it to the spectrometer. The second is that a large tilt may bring the magnet coils into the beam path and attenuate the intensity.

2.6 Reciprocal lattice units

The reciprocal lattice of $Bi_2Sr_2CoO_{6+\delta}$ is defined by the vectors $\mathbf{a}^* = \frac{2\pi}{a}$, $\mathbf{b}^* = \frac{2\pi}{b}$, and $\mathbf{c}^* = \frac{2\pi}{c}$, where a, b and c are the lattice constants of the orthorhombic unit cell. We may write the scattering vector for the allowed nuclear and magnetic reflections in terms of integer multiples of the reciprocal lattice vectors, $\mathbf{Q} = H\mathbf{a}^* + K\mathbf{b}^* + L\mathbf{c}^*$. The face-centered orthorhombic structure of $Bi_2Sr_2CoO_{6+\delta}$ results in nuclear reflections only at reflections defined by H, K and L all even or all odd, while magnetic reflections may occur at other positions in reciprocal space.

All of the neutron data in this thesis are presented in terms of reciprocal lattice units. For example, one reciprocal lattice unit along $\mathbf{a}^*$ is equal to $\frac{2\pi}{a} = 1.155\mathring{A}$. Thus, a scan along H through the (2, 0, 0) reflection corresponds to scanning along $\mathbf{a}^*$ through the reflection at $(\frac{4\pi}{a}, 0, 0)$.

2.7 Resolution

Although the Bragg reflections occur at δ-functions in reciprocal space, the Bragg peaks measured in a spectrometer have a finite width. This is because the incident wave vector is not perfectly well defined in energy or direction. In addition to the imperfect collimation, the monochromator and analyzer, as well as the sample, have a finite mosaic. The measured peak is therefore a convolution of the spectrometer resolution function, $R(\mathbf{Q},\omega)$ and $S(\mathbf{Q},\omega)$. To perform the convolution, we use a fit routine which convolves the calculated resolution function $R(\mathbf{Q}, \omega)$ of a triple-axis spectrometer with $S(\mathbf{Q},\omega)$.

For our diffraction measurements, $S(\mathbf{Q},\omega)$ is essentially $\delta(\mathbf{Q} - \mathbf{G})\delta(\hbar\omega)$ and the peak width is simply determined by the resolution function. However, short-range order broadens the peaks. Physically, this results from a cut off of the region over which spins or structural features are correlated so that the periodicity, and hence $\mathbf{Q}$, are no longer well defined.

As a *crude* rule of thumb, the resolution of longitudinal (parallel to Q) scans is determined by the spread in the directions of $\mathbf{k}_i$ and $\mathbf{k}_f$, and hence the collimation, while the resolution for transverse (perpendicular to $\mathbf{Q}$) scans is strongly dependent on the sample mosaic and is coupled to the energy resolution. Transverse scans often have structure as a result of the mosaic, which can lead to an asymmetric line-shape. As a reference, the effects of changing the collimation on both transverse and longitudinal scans through a structural peak in a high-quality crystal are shown in Figure 2-4. The inset shows the fitted HWHM of the peaks for the different collimation settings. The peaks are normalized to the same amplitude, which masks the fact that increasing the resolution results in a loss of intensity. In Fig. 2-4, increasing the resolution by a factor of 2 results in a decrease in the intensity by nearly a factor of 3.

The effect of mosaic on transverse scans in evident in Figure 2-5 which shows scans through (0, 2, 0) along L in xtals 1974b and 2002b. Xtal 1974b has a much narrower mosaic (with very little structure) compared to xtal 2002b.

Although it is possible to determine the resolution widths fairly accurately with the convolution program, the task of determining the intrinsic width of $S(\mathbf{Q})$ is at best approximate. This is because the mosaic does not necessarily make a simple contribution to the line-shape. In the fits shown in this thesis, the mosaic is assumed to have a Gaussian shape.

2.8 Neutron peak intensities: extracting absolute units from neutron peaks

In this thesis, we are interested in obtaining the magnitude of the local moment on the Co site in $Bi_2Sr_2CoO_{6+\delta}$ as a function of δ. In theory, one can do this in a given sample by normalizing the *integrated intensity* of a magnetic Bragg peak to the integrated intensity of a nuclear Bragg peak, since the structure factors for the nuclear peak are known from powder neutron measurements (see Appendix).

The integrated intensity of a Bragg peak is obtained by rotating the crystal through the Bragg condition and taking the area under the peak. The integrated intensity is given by

$$I = \Phi \frac{N\lambda^3}{v_0} \frac{F^2(Q)}{\sin(2\theta)} \tag{2.37}$$

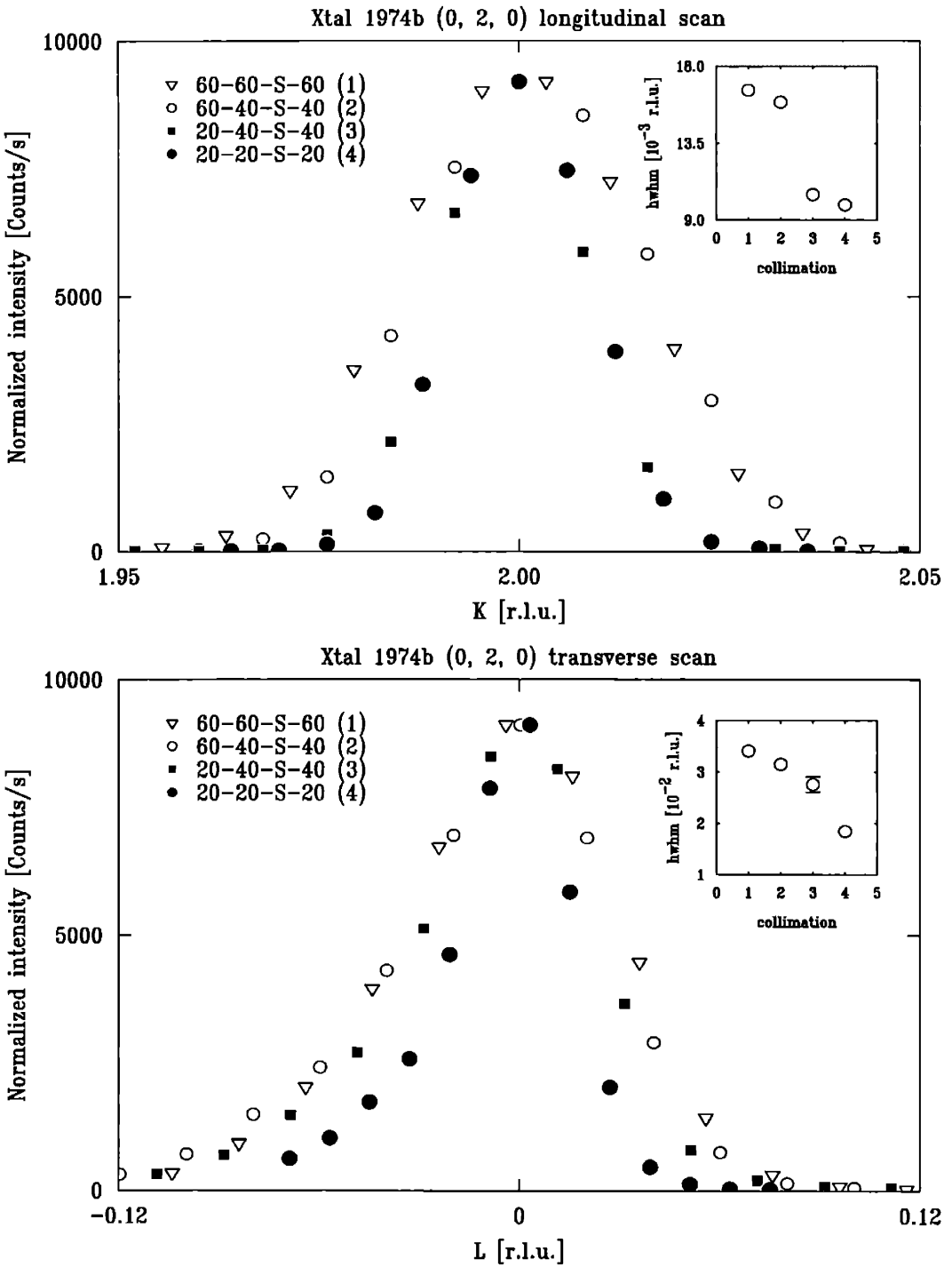

Figure 2-4: The effects of changing the collimation on the (0, 2, 0) peak width in xtal 1974b, which has a narrow mosaic ($< 15'$). The top panel shows longitudinal scans; the bottom panel shows transverse scans. All of the peaks are normalized to the same amplitude, to emphasize the change in width. The inset shows the fitted HWHM in r.l.u., assuming a Gaussian line-shape. 1 r.l.u. along K = 1.155 $\AA^{-1}$; 1 r.l.u. along L = 0.266 $\AA^{-1}$.

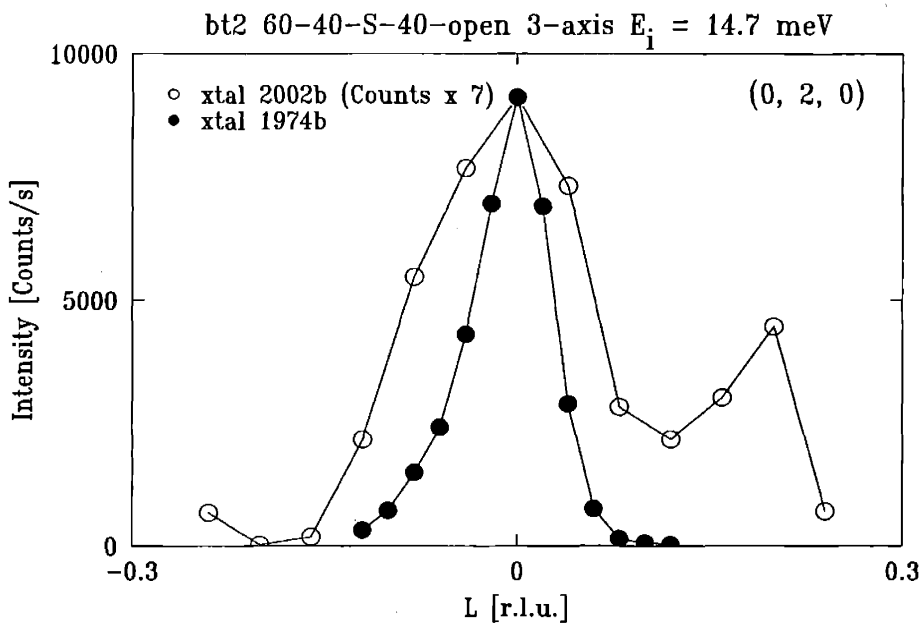

Figure 2-5: Transverse scans through the (0, 2, 0) reflection in different crystals. Crystal 2002b has a poorer mosaic than crystal 1974b. The scan through (0, 2, 0) in the 2002b crystal is multiplied by a factor of 7.

In Equation 2.37, Φ is the neutron flux, v_0 is the volume of the unit cell, $\sin(2\theta)$ is the Lorentz factor and $F(Q)$ is the structure factor for nuclei or magnetic spins:

$$\begin{aligned} F_{nuc}(\mathbf{Q}) &= \sum_p b_p e^{i\mathbf{Q}\cdot\mathbf{p}} \\ F_{spin}(\mathbf{Q}) &= \frac{g}{2}(\gamma r_0)\sum_d f_d(\mathbf{Q})\mathbf{S_d}(1-\hat{\mathbf{Q}}\cdot\hat{\mathbf{S_d}})e^{i\mathbf{Q}\cdot\mathbf{d}} \end{aligned}$$

If we take the ratio between the intensity in a magnetic peak and a nuclear peak, all of the extrinsic pre-factors (such as sample volume and neutron flux) cancel and we are left with

$$\frac{I_{spin}\times\sin(2\theta_{mag})}{I_{nuc}\times\sin(2\theta_{nuc})} = \frac{\mid F_{spin}(Q)\mid^2}{\mid F_{nuc}(Q)\mid^2} \tag{2.38}$$

In a triple-axis spectrometer, Eqn. 2.37 is only strictly correct for a θ-2θ scan in which the crystal is rocked through the Bragg condition in steps of θ and the diffractometer arm is stepped in increments of 2θ. The crystal mosaic contributes to the spread in the diffracted beam, so the presence of the analyzer does not allow all of the diffracted neutrons to enter

the detector unless a θ-2θ scan is performed.

Another caveat is that the integrated intensities may be affected by extinction effects, which are most pronounced at strong reflections. On the other hand, the strong reflections in $Bi_2Sr_2CoO_{6+\delta}$ are least sensitive to small changes in the structure resulting from changing the oxygen content. In consideration of this, most of the magnetic peaks are normalized to several structural peaks.

The following is a simple calculation which should serve as a reference for the measurements discussed in this thesis. In this calculation, we are interested in extracting the size of the local moment on Co in the antiferromagnetically ordered state from measurements of the magnetic and nuclear Bragg peaks. The details of the antiferromagnetic order in $Bi_2Sr_2CoO_{6+\delta}$ are discussed in Section 4.1; we will simply state the results here. A single structural unit-cell is shown in Figure 2-6, indicating only the Co ions and the spins on these ions. In the ordered state, the spins lie along the a-axis. Nearest neighbor spins in the plane are antiferromagnetically ordered, while in adjacent layers, all spins in the same ac plane lie in the same direction. In the orthorhombic structural unit cell, there are four spins at the positions $d_1 = 000$, $d_2 = \frac{1}{2}\frac{1}{2}0$, $d_3 = \frac{1}{2}0\frac{1}{2}$ and $d_4 = 0\frac{1}{2}\frac{1}{2}$. The spins on these sites are represented by the vectors $S_1 = S\hat{a}$, $S_2 = -S\hat{a}$, $S_3 = S\hat{a}$, and $S_4 = -S\hat{a}$ respectively.

Let us consider the (0, 1, 0) antiferromagnetic reflection, which is indicated schematically in Figure 2-6. At the (0, 1, 0) reflection, $\mathbf{Q}$ and $\mathbf{S}$ are perpendicular and $(1 - \hat{\mathbf{Q}} \cdot \hat{\mathbf{S}}) = 1$. Therefore,

$$F_{spin}(\mathbf{Q}) = \frac{g}{2}(\gamma r_0) f_{spin}(Q)(\sum_d S_d e^{i\mathbf{Q}\cdot\mathbf{d}}) \tag{2.39}$$

$$= \frac{g}{2}(\gamma r_0) f_{spin}(Q)(4S) \tag{2.40}$$

From the Appendix, $f_{mag}(Q) = 0.94$ and $\sin(2\theta)$ for 14.7 meV neutrons is 0.42 at (0, 1, 0). We will normalize to the (0, 0, 4) nuclear reflection, for which the structure factor is 5.6 $\times 10^{-12}$ cm and $\sin(2\theta)$ is 0.39. It should be noted that the nuclear structure factor in the Appendix corresponds to the *entire* unit cell, which is four times the orthorhombic sub-cell we are considering here. The theoretical ratio of the integrated spin intensity at the (0, 1, 0) reflection to the integrated nuclear intensity at the (0, 0, 4) reflection is

$$\frac{I_{spin}}{I_{nuc}} = 1.92\ S^2 \tag{2.41}$$

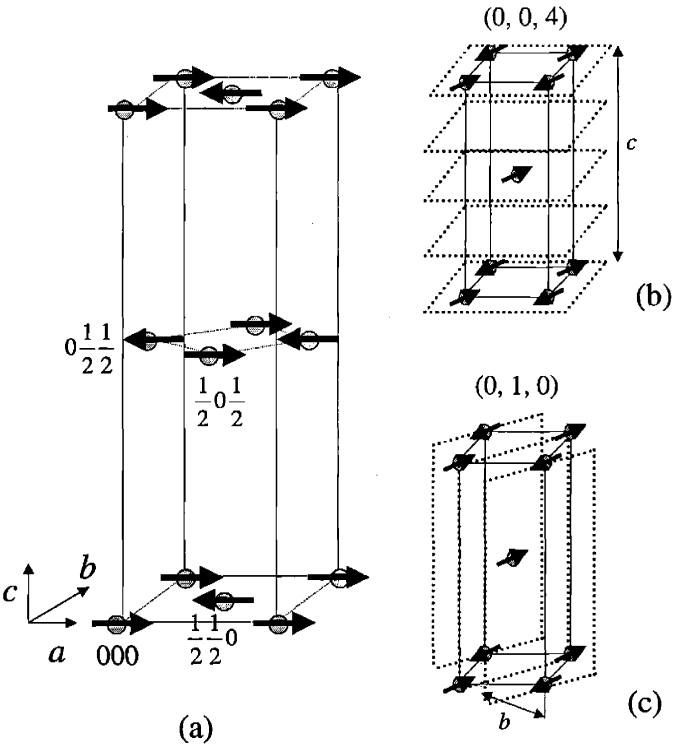

Figure 2-6: (a) Antiferromagnetic structure in $Bi_2Sr_2CoO_{6+\delta}$ indicating the four unique spins in the orthorhombic unit cell. Figures (b) and (c) are graphical representations of the (0, 0, 4) and (0, 1, 0) reflections, respectively.

Thus, for S = 1, the magnetic scattering is approximately twice the intensity of the nuclear scattering at the (0, 0, 4) reflection.

Chapter 3

Preparation and characterization of single crystal $Bi_2Sr_2CoO_{6+\delta}$

3.1 Single crystal growth

Large, single crystals of $Bi_2Sr_2CoO_{6+\delta}$ were necessary for our magnetic neutron scattering measurements. I am grateful to Dr. Fang Chou for having grown all of the beautiful crystals which were studied in this thesis.

The $Bi_2Sr_2CoO_{6+\delta}$ crystals studied in this thesis were grown in an Optical Floating-Zone Crystal Furnace (Figure 3-1). In the floating-zone method, the crystal grows on a "seed", which is pulled from a molten zone of raw material and flux. The molten zone is held by surface tension between the raw material feed rod and the seed. Since no crucible is needed, the crystals grown in a floating-zone furnace are free of contaminants.

The three material components necessary for crystal growth in a floating-zone furnace are the feed rod, the seed and the flux. The feed rod and seed have the desired stoichiometry of the final crystal, while the flux has a composition off-stoichiometry to lower the melting point of the molten zone. To prepare the feed rod for $Bi_2Sr_2CoO_{6+\delta}$ crystals, Bi_2O_3, $SrCO_3$, and CoO powders are finely ground and annealed in air at 850 C for 12 hours. The purpose of this process, called calcining, is to evolve the CO_2 from the powders. After calcining, the powder is re-ground, pressed into a tight rod, and annealed at 900 C, in air, to drive forward the solid state reaction. The resulting feed rod is polycrystalline $Bi_2Sr_2CoO_{6+\delta}$. Either a piece of the polycrystalline feed rod or the end of a previously grown single crystal

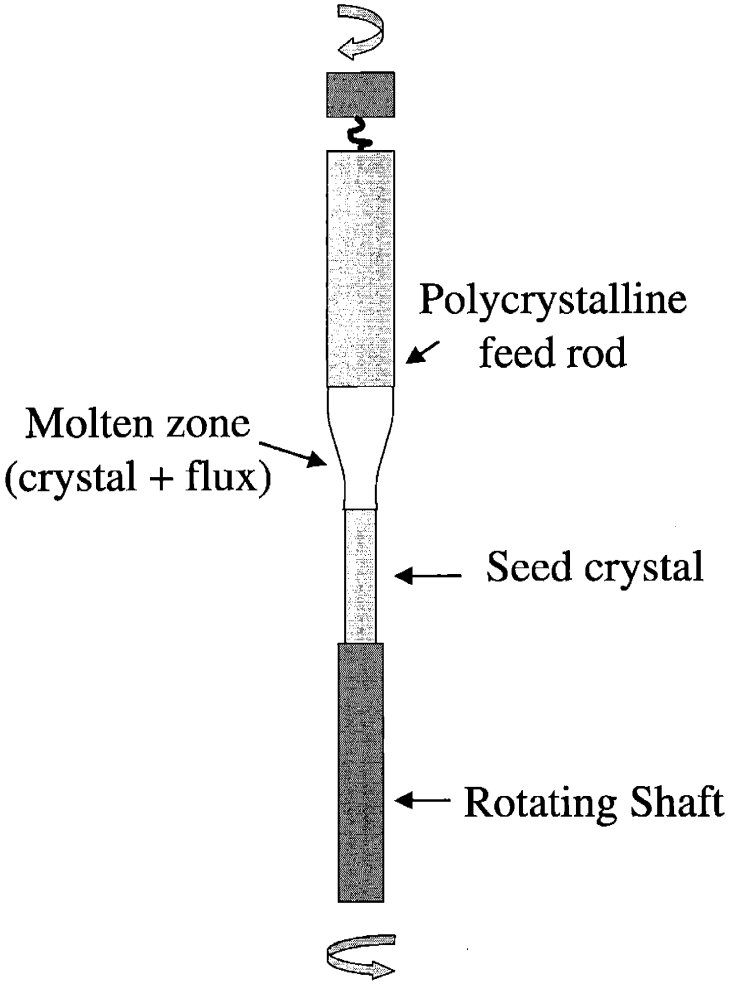

Figure 3-1: Schematic of the vertical column in a floating-zone furnace. The crystal rod is thinner than the polycrystalline feed rod because it is of a higher density. Two elliptical mirrors (not shown) focus Xenon lamps onto the molten zone, providing homogeneous heating. The counter-rotation of the upper and lower shafts serves to mix the material in the molten zone.

can serve as the seed crystal. Seeding with a single crystal provides more control over the growth direction than seeding with a polycrystalline rod. In addition, single crystal seeds expedite the formation of a single grain. Finally, the optimal flux composition is a Bi_2O_3 rich flux with a molar ratio of 4:1 $Bi_2Sr_2CoO_{6+\delta}$:Bi_2O_3.

The crystals are grown in air or a flow of 5-10 cc/min O_2 at a pulling rate of $\sim$ 2 mm/hour. The resulting crystal rods are typically 3-4 cm in length and a few mm in diameter.

Six different single crystal rods were studied with neutrons. The mosaic widths of these crystal rods varied from 15 to 60′.[1] The crystals with the narrowest mosaic widths were xtal 1974b, xtal 2043 and xtal 2043an800C. The latter two were from the same rod, but xtal 2043an800C was from the end stage of the growth and showed an improved mosaic over xtal2043. Xtal 1974b consisted of a single crystallite and had a mosaic of $\sim$ 15′. Xtal 2043 and xtal 2043an800C each contained several crystallites, but the crystallites were narrow and well separated so that it was possible to choose one for all of the measurements. Xtals 2002b and 1974C had much poorer mosaics ($\sim$ 60 ′).

3.2 Crystal orientation with Laue

$Bi_2Sr_2CoO_{6+\delta}$ crystals cleave easily along the c-axis because of the weakly coupled Bi-O layers. As a result, it is easy to locate the c-axis by finding a flat face on the surface of the crystal rod. A razor blade can then be used to flake off smaller pieces for transport and susceptibility measurements. The crystals cleave naturally into rectangles, with **a** and **b** along the edges, and are typically less than 0.5 mm perpendicular to the faces.

A Laue reflection photo of a cleaved piece is taken to distinguish **a** from **b**. A Laue camera is available in the CMSE Shared Facility. In the Laue geometry, the single crystal is fixed in space and a broad-band x-ray source is directed at the crystal surface (Figure 3-2). Since there is a continuum of wavelengths in the x-ray beam, the Bragg condition is satisfied for a number of reflections even though the crystal has a fixed orientation. The Bragg reflected x-rays are recorded with photographic film.[2] The Laue pattern is a snapshot of the crystal's reciprocal lattice as seen looking down the x-ray beam axis. Since the crystal lattice and reciprocal lattice have the same symmetry, the crystal is rotated in a goniometer

[1] The mosaic is the spread in orientation of the crystallites within the entire sample rod.

[2] A fluorescent screen is placed in front of the film to convert the x-rays into lower energy photons.

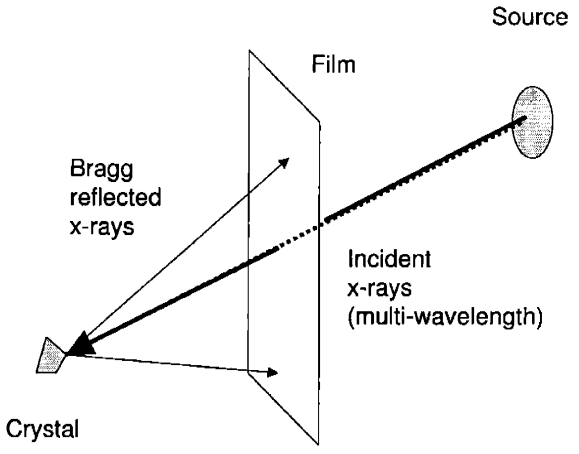

Figure 3-2: Set-up for a Laue reflection photograph

until the photograph reveals the correct symmetry and pattern. For example, to distinguish the a-axis from the b-axis in $Bi_2Sr_2CoO_{6+\delta}$, the crystal should be oriented with the c-axis parallel to the x-ray beam. The Laue photo shows more closely spaced reflections along **a** than along **b** because of the superstructure.

In practice, a Laue photo is not necessary for each new sample because several features allow one to distinguish **a** from **b** by eye. We find that the crystals always grow along **b** and cleaved rectangular pieces tend to have **b** along the long direction. Often, the buckling of the Bi-O layer is manifested by lines on the surface of the crystal, which are perpendicular to **a**. More importantly, the in-plane anisotropy of the susceptibility is also sufficiently large that **a** is easily distinguished from **b**.

3.3 Susceptibility measurements

The magnetization of single crystals of $Bi_2Sr_2CoO_{6+\delta}$ is measured from 5-400 K and in fields up to 5 Tesla using a Quantum Design Super-conducting QUantum Interference Device (SQUID) magnetometer in conjunction with a He4 cryostat (Figure 3-3). The SQUID device senses the flux from the magnetic dipole field of the sample as it is pulled vertically through the SQUID coil. The inner and outer coils of the SQUID are counter-wound (Figure 3-4a) to cancel the flux resulting from the applied field and any stray fields, which are constant along **z**. The magnetic flux through the SQUID as a function of the sample's distance from the center of the coil has the shape shown in Figure 3-4(b). As the sample is pulled

through the coil, a feedback circuit generates a current to cancel the magnetic flux in the SQUID. The amplitude of the voltage required to produce this current is proportional to the magnetic moment of the sample and is calibrated to a standard palladium sample. The total magnetic moment of the sample, **m**, is therefore measured in absolute units of **emu**. (The **emu** is the cgs unit for moment; the cgs unit of magnetic field is **Gauss**.)

The important thermodynamic quantities measured in a magnetometer are the magnetization $\mathbf{M} = \mathbf{m}/\mathrm{V}$ and the parallel susceptibility χ_x defined as $\mathrm{dM}_x/\mathrm{dH}_x$ as H approaches zero. In linear materials, χ_x is constant in field so that $\chi_x = \mathrm{M}_x/\mathrm{H}_x$. Since the SQUID measures the magnetic moment in **emu** (1 **emu** = 1 **erg/gauss**), χ is unitless. (It is useful to remember that $\mathbf{M}\cdot\mathbf{H} = \chi\ \mathrm{H}^2$ should have units of energy density, or **erg/cm**^{3}, in cgs units.)

The magnetic moment is more often normalized to the mass or molar mass of the sample than the sample volume. The susceptibility is therefore presented in units of **cm**^{3}**/g** or **cm**^{3}**/mole** of material. For example, the Curie susceptibility of one mole of non-interacting spins with spin S is given by,

$$\begin{aligned} \chi_{Curie} &= \frac{N_A(g\mu_b)^2 S(S+1)}{k_b T} \\ &= \frac{C}{T} \end{aligned}$$

where $\mu_b = 9.27 \times 10^{-21} \frac{erg}{gauss}$, $k_b = 1.38 \times 10^{-16} \frac{erg}{K}$, and $N_A = 6.02 \times 10^{23} \frac{spins}{mole}$. For spins with $S = 1$ and $g = 2$, the Curie constant C is equal to 3 $\frac{cm^3 K}{mole}$. The susceptibility data in this thesis are reported in **cm**^{3}**/mole**. There is one Co spin per formula unit of $Bi_2Sr_2CoO_{6+\delta}$ and the mass of one mole of $Bi_2Sr_2CoO_{6.25}$ is 752 g.

The susceptibility of $Bi_2Sr_2CoO_{6+\delta}$ depends strongly on the direction of the magnetic field with respect to the crystalline axes. To measure the susceptibilities χ_a, χ_b, or χ_c, small rectangular pieces (1-20 mg) are oriented with either **a**, **b** or **c** parallel to the magnetic field in the SQUID. A plastic drinking straw, as well as any structure that can be built from a drinking straw, supports the sample in the SQUID. To mount the sample with either **a** or **b** vertical, we fold a straw in half and line up either **a** or **b** with the fold. The sample is then secured in place by crimping the straw with a hot iron on either side of the sample. To measure the *c*-axis susceptibility, the sample is pressed between the ends of two straws and wedged into a third straw. We typically achieve better than 5° alignment

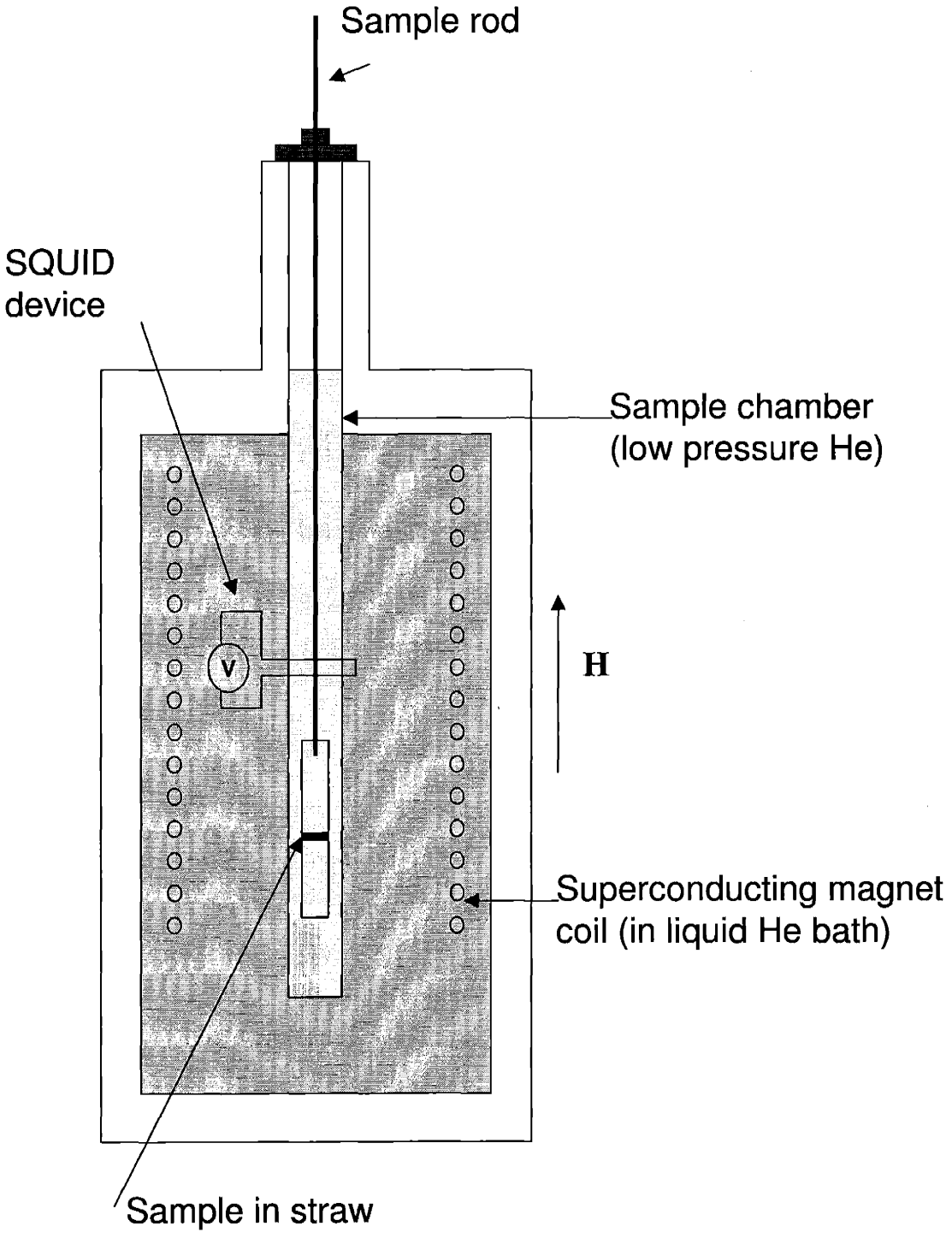

Figure 3-3: Cross-section of the SQUID and He4 cryostat. The magnetic field is supplied by the superconducting coils and is co-axial with the z-axis of the SQUID coil. A drinking straw holds the sample.

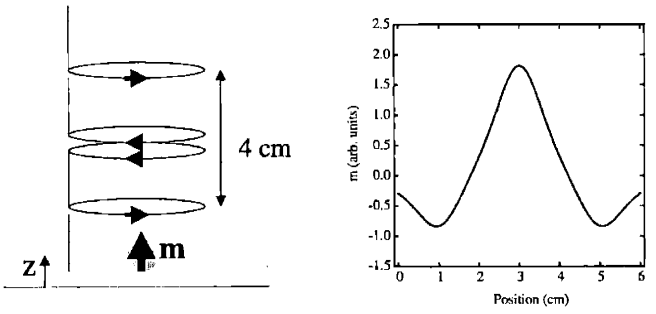

(a) (b)

Figure 3-4: (a) Schematic of the SQUID coil. The SQUID voltage is proportional to the total magnetic flux through the coil. The inner and outer coils are counter-wound in order to cancel the contribution from any field that is constant along **z**. (b) Voltage curve for a 6 cm scan through the coils. The center of the coil is at 3 cm

of the desired crystal axis with the field. The contribution from the susceptibility along a perpendicular axis is therefore of order $\chi \sin^2(\theta)$, where θ is the angle of misalignment and χ is the susceptibility along the perpendicular direction. For a 5° alignment error, $\sin^2(\theta)$ is less than 1%. However, since both χ_a and χ_b can be more than 10 times the magnitude of χ_c, even a 5° error in alignment of the c-axis with the field can lead to a substantial contribution from either χ_a or χ_b.

3.4 Transport measurements

The temperature dependent resistivities of single crystals were measured from $\sim$ 100 K to 400 K. For most of the samples, the resistivity was measured in the four-probe geometry, in which a fixed current was passed between two outer leads and the voltage drop across the sample was measured between two inner leads (see Figure 3-5). The four-probe configuration removed the contribution of the contact resistance, which was 1-10 times as large as the sample resistance. However, to measure the resistivity with the current parallel to **c**, the 2-probe geometry was used because the samples were too thin in the c-direction to permit the application of voltage contacts.

For the resistivity measurements, we use pieces with thickness $t \sim$ 100-300 μm and area

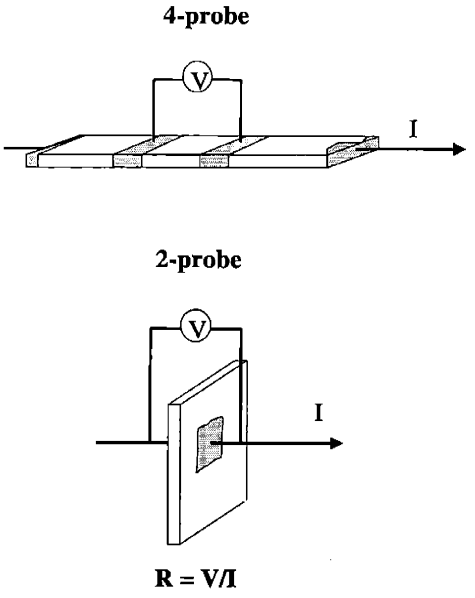

Figure 3-5: Geometry for resistivity measurements. The 4-probe geometry removes the contacts' contribution to the resistivity. The 2-probe geometry must be used for measurements of ρ_c because the sample dimension is so thin in this direction.

0.25-4 mm^2. The lowest contact resistance is achieved when contact pads are evaporated onto the crystal surface. A thin (300-500 $\AA$) layer of Cr is evaporated first, followed by a thicker (1000-1500 $\AA$) layer of Au. Au is used instead of silver because it does not form an oxide over time. Thin pieces of aluminum foil are used to mask the samples during evaporation. Thin Cu or Au wires are attached to the contact pads using Epotek H20E Ag epoxy. The epoxy is cured for approximately 1 hr in air at 90-100 C. The low curing temperature is important since the oxygen in $Bi_2Sr_2CoO_{6+\delta}$ starts to evolve from the sample around 300 C. Evaporated contacts typically have a resistance of 0.5-3 kΩ and can last for several years.

The resistance is measured by applying a DC current through the current leads and measuring the voltage drop between the voltage contacts. To remove any constant offset in the voltage (e.g. thermoelectric voltage), the voltage is measured for both positive and negative current such that,

$$R = \frac{V(+I) - V(-I)}{2I} \tag{3.1}$$

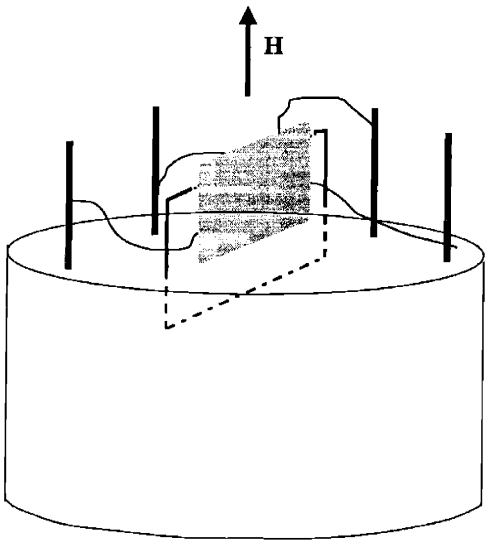

Figure 3-6: Geometry for magneto-resistance measurements. The sample holder (white cylinder) is a Teflon chip carrier. The grey patch indicates the sample, which is attached to a glass slide.

If the sample is in the shape of a rectangular parallelepiped with cross-sectional area A and the voltage contacts are separated by distance l, the resistivity ρ is related to the measured resistance by $\rho = \mathrm{R(A/l)}$. In practice, the samples do not have a perfect rectangular shape and the contacts may not evenly cover the ends and sides. However, we find similar values of the resistivity for measurements made on different pieces cleaved from the same sample.

The temperature dependence of the resistivity is measured in a SQUID equipped with an electronic feed through. The sample sits on an Augut 8058-1G32 circular 8-pin Teflon chip carrier. The as-purchased chip carrier is about 10 mm in diameter and it is necessary to shave the edges of the chip carrier in order to fit it into the 9 mm SQUID chamber. For zero-field resistivity measurements, the sample can lie flat on the base of the chip carrier. However, for magneto-resistance measurements, the field is applied along the a-axis and the sample must sit on a thin edge (Figure 3-6). To support the crystal in the chip carrier, the sample is first glued to a thin microscope slide using either PMMA (a photoresist) or GE varnish. Both of these adhesives thermally cycle well and are easily removed with acetone. A "trench" is cut into the chip carrier and the sample is glued into the trench. Both the PMMA and the GE varnish can remain in tact after the 100 C anneal of the Ag epoxy used to attach the wires to the sample.

xtal name	annealing procedure	final T_{peak}
1974C	annealed 12 hrs. 800 C EQT; re-ox 900 C and slow cool	295 K
1955	as-grown	235 K
1955	annealed 12 hrs. 600 C QT	170 K
2043	annealed 12 hrs. 650 C QT	148 K
1949	annealed 0.5 hrs. 700 C QT	95 K
2043an800c	annealed 12 hrs. 800 C QT	25 K
2002b	annealed 1 hr. 800 C EQT	40 K
1974C	annealed 12 hrs. 800 C EQT	48 K

Table 3.1: Annealing history of the single crystals shown in Figure 3-7. EQT indicates the sample was annealed in an evacuated quartz tube with Cu powder as a reducing agent. QT indicates annealing in vacuum in a quartz tube evacuated to below 30 mTorr with a turbo pump.

3.5 Vacuum annealing

As we show in Chapter 4, as-grown crystals have a transition to antiferromagnetic order below a temperature $T_N \sim 250$ K. The susceptibility of these samples measured with the field along **a** has a peak at $T_{peak} \sim T_N$. Annealing the as-grown crystals in vacuum reduces the oxygen content and suppresses both T_N and T_{peak}. The higher the temperature of the anneal, the lower the resulting T_N and T_{peak}. When crystals are reduced at very high temperatures ($\sim$ 800 C), the antiferromagnetic phase is destroyed. However, a peak in the susceptibility remains, at around 25-30 K. Figure 3-7 shows the susceptibility curves for samples which have been exposed to different annealing conditions.

To prepare most of the oxygen deficient samples, a quartz tube furnace connected to a turbo pump is used to anneal as-grown samples in 10-30 mTorr and between 400 and 800 C. An alternative method used to achieve samples with low T_N is to place the sample in an evacuated quartz tube with a small amount of Cu powder. The sample is then heated for 1 hr at 800 C. The Cu powder acts as a reducing agent to the $Bi_2Sr_2CoO_{6+\delta}$. We find that a lower T_{peak} can be obtained by annealing in the turbo pumped tube furnace than using the Cu powder. The annealing procedure for each of the samples shown in Fig. 3-7 is summarized in Table 3.1.

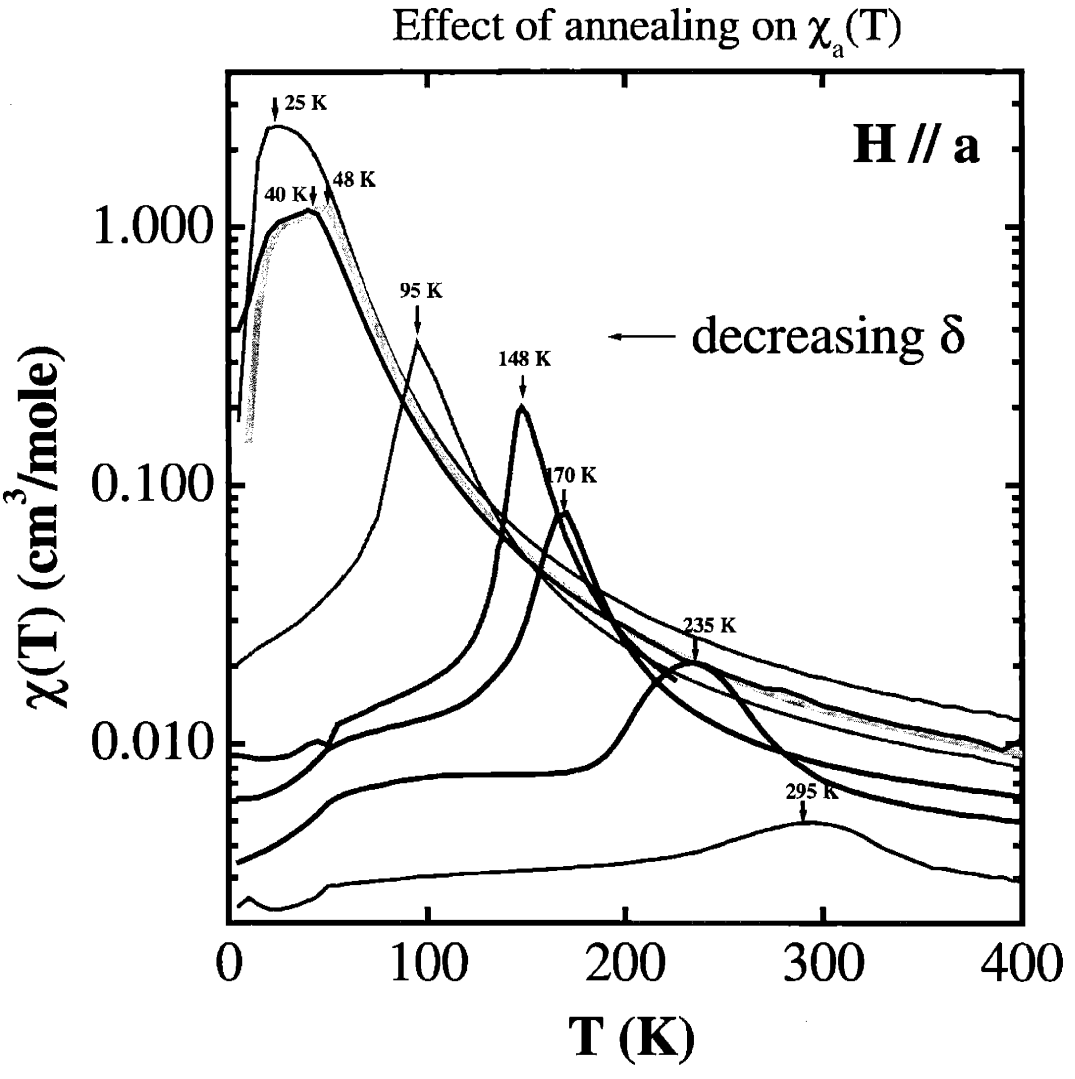

Figure 3-7: Susceptibility of $Bi_2Sr_2CoO_{6+\delta}$ single crystals for different annealing conditions. The arrows indicate the temperature of the peak in the susceptibility, T_{peak}. The annealing history of each sample is given in Table 3.1.

3.6 Determining the oxygen content, δ

An important part of this thesis is showing the relationship between the magnetic properties of $Bi_2Sr_2CoO_{6+\delta}$ and δ. Namely, we would like to parameterize the peak in the susceptibility, T_{peak}, with the oxygen content, δ. Unfortunately, measuring the absolute value of δ in $Bi_2Sr_2CoO_{6+\delta}$ for a given sample is quite difficult. For example, electron probe microanalysis (EPMA), which is fairly sensitive to the relative composition of Bi, Sr and Co, is a poor probe of the oxygen content.

An accepted means of determining the oxygen content is with thermo-gravimetric analysis (TGA). The TGA is a sensitive balance, which measures small changes in sample mass (of the order of 1 μg in 50 mg) as a function of temperature. Different gases, such as H_2, He, Ar, and O_2, may be chosen to change the ambient conditions. The sample is placed on a platinum pan and a background measurement with an empty pan is always performed prior to a measurement with the sample in the TGA.

We use TGA to measure changes in the mass of samples of $Bi_2Sr_2CoO_{6+\delta}$ resulting from the loss or gain of oxygen while changing temperature. The difficulty is that the TGA only measures *changes* in the oxygen content as the sample is either oxidized or reduced. Thus, it is necessary to make assumptions about the *absolute* value of δ for either the starting or final point of a TGA trace. Here, I discuss two methods of determining δ using TGA analysis, the decomposition method and the reduction-oxidation method.

3.6.1 Decomposition method

In this method, based on experiments described in Zinkevich *et al.* [29] a piece of an as-grown crystal is heated in the TGA in a strongly reducing hydrogen environment until the sample decomposes. When the sample is decomposed, only Bi and Co metal and SrO are left behind; the extra oxygen leaves in the form of a gas. The measured weight loss is therefore equated to the loss of $(4+\delta)$ moles of oxygen per formula unit:

$$Bi_2Sr_2CoO_{6+\delta} \rightarrow 2Bi + 2SrO + Co + (4+\delta)O_g \tag{3.2}$$

This measurement provides an *absolute* measurement of the oxygen content of the decomposed sample. The mass loss is also well within the sensitivity of the TGA: for a 50 mg sample, the mass loss corresponding to the loss of 4.5 oxygen atoms per formula unit is

about 4.8 mg (or 10% of the total mass).

For our measurements, as-grown samples with masses 2-20 mg were heated to 560-625 C in the TGA under a flow of 5% H_2/95% He gas. In several attempts at measuring the oxygen content in this way, we obtained δ ranging from 0.23 to 0.5.

These results agree with previous reports [12, 29] of δ using TGA, and are consistent with a formula unit of $Bi_2Sr_2CoO_{6+\delta}$ with δ greater than 0.25. However, the error is too large in these measurements to provide useful information. One likely source of error is incomplete decomposition. When a sample with $\delta \sim 0.5$ is decomposed, 90% of the weight loss is structural oxygen and incomplete decomposition leads to an underestimate of δ. On the other hand, Bi may evaporate slightly during the annealing process, leading to an overestimate of δ. These two factors are difficult to control and can contribute to a large variation in the measured δ.

3.6.2 Oxidation-reduction method

In the oxidation-reduction method, the sample environment in the TGA is controlled so that only interstitial oxygen atoms enter or leave the crystal. We define a sample with a particular T_N as the "reference" sample with an assumed δ. If the reference sample is oxidized, the mass gain is equated to an increase in δ. Similarly, if the reference sample is reduced, the mass loss is equated to a decrease in δ. The challenge is to choose an appropriate reference sample. We choose a crystal which is annealed at 800 C in vacuum and has a $T_{peak} \simeq$ 25 K in the susceptibility as the reference sample. Experimentally, we find that 25 K is the lowest T_{peak} which can be obtained by vacuum annealing. This suggests that samples with $T_{peak} \sim 25$ K are depleted of interstitial oxygen and only structural oxygen remains. Therefore, these samples should be closest to the formula unit of $Bi_2Sr_2CoO_{6.25}$ determined by neutron powder diffraction.

Experimentally, the oxidation-reduction method yields more reproducible results than the decomposition method. More importantly, we are able to obtain several points on the T_{peak} vs. δ curve without destroying the sample.

For the measurements described above, as-grown crystals (xtals 2017 and 2043) were annealed in vacuum at 800 C. The resulting T_{peak}s of these annealed samples were 25-30 K.

Oxidation

For the oxidation step, we prepare a sample with $T_{peak} \simeq 25$ K and define δ for this sample to equal 0.25. This sample is then heated to $\approx$ 900 C in the TGA under oxygen flow, held at 900 C for 30 minutes, and cooled down to room temperature. The heating and cooling rates are 2 C/min. The TGA trace of the sample mass as a function of temperature is shown in Figure 3-8(a). The trace shows a characteristic increase in the mass around 400 C and then a decrease above 700 C. Upon cooling the mass again increases. This behavior is seen in all samples which are heated up to 900 C.

To calculate δ of the re-oxidized sample, let m equal the initial mass of the sample, Δm equal the change in mass of the sample, and $\Delta\delta$ equal the increase in δ upon annealing. Then

$$\Delta\delta = \frac{\Delta m}{m} \times \frac{752\ g/mole}{16\ g/mole} \tag{3.3}$$

The mass of one formula unit of $Bi_2Sr_2CoO_{6.25}$ is 752 g/mole and the mass of one mole of oxygen is 16 g/mole. The total percent change in sample mass in the measurement shown in Figure 3-8 is 0.57 %, which corresponds to a change in δ of 0.26. Thus, the re-oxidized crystal has $\delta = 0.51$. The susceptibility of the reference crystal before and after the 915 C oxygen TGA anneal is shown in Figure 3-8(b). The oxygen anneal of the reduced sample results in an increase in T_{peak} from 25 K to 270 K.

The re-oxidized crystal exhibits a similar susceptibility to that of an as-grown crystal with similar T_{peak}. This is an important result because it says that it is possible to reversibly remove and re-introduce oxygen into $Bi_2Sr_2CoO_{6+\delta}$.

Reduction

The oxidation process described above provides two end-points for the T_{peak} vs. δ phase diagram. To determine intermediate points, it is necessary to either reduce the re-oxidized crystal or more incompletely oxidize the $\delta \sim 0.25$ crystals. It turns out that the latter method does not result in crystals with the same magnetic properties as as-grown crystals (I will discuss this in Chapter 5). In the former method, the re-oxidized crystal is heated in the TGA in a reducing environment of either argon gas or a 5%H_2/95%He mixture. We find that annealing the sample in the TGA in argon up to 700 C results in only a small decrease

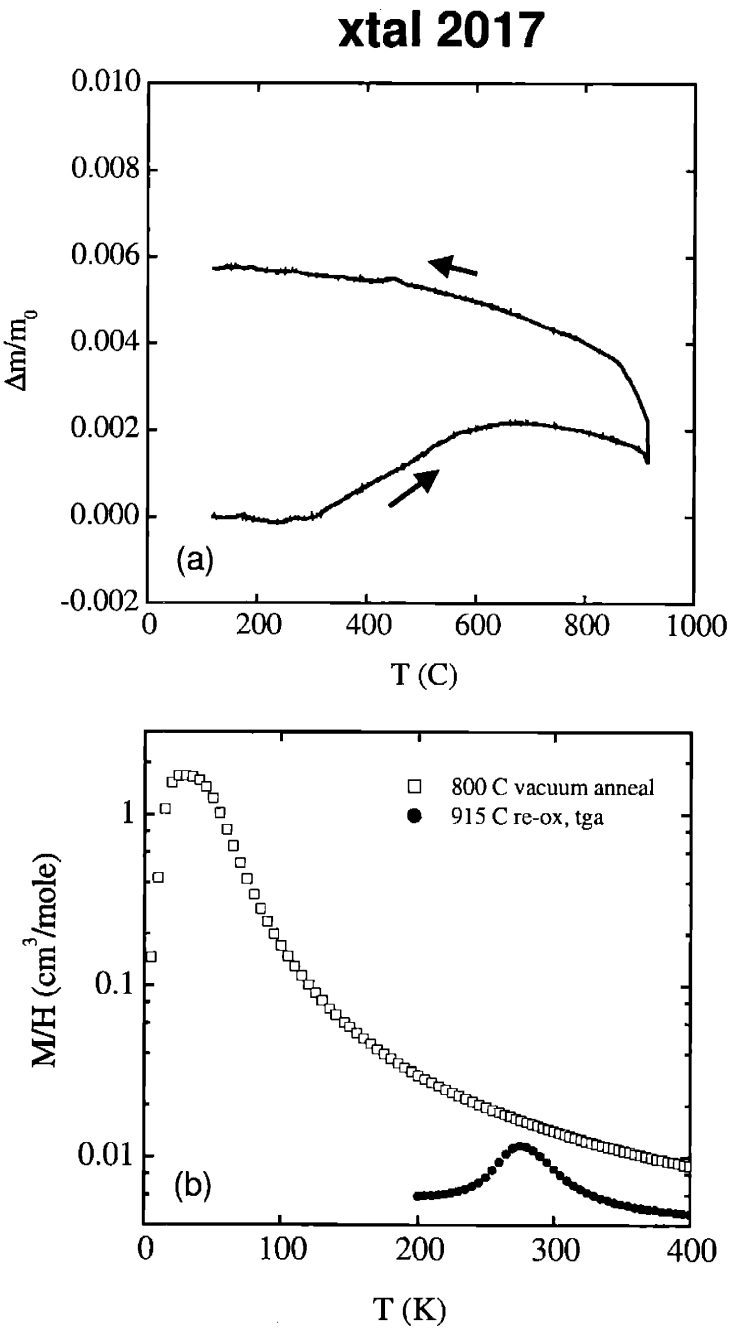

Figure 3-8: (a) TGA trace showing the change in mass during re-oxidation of a reduced crystal. (On this plot, 0.001 on the y-axis corresponds to a change of 0.1 %.)The heating and cooling rates are 2 C/min and the sample is held at 900 C for 30 minutes. (b) Comparison of the susceptibility before (open squares) and after (closed circles) the re-oxidation. The susceptibility is plotted on a semi-logarithmic scale.

in T_{peak} in the susceptibility and a negligible mass change. As shown in Figure 3-9, there is little difference between Δm measured with the sample and without the sample (empty pan). Annealing in hydrogen (Figure 3-10) results in a substantial mass loss; however, the hydrogen annealed samples tend to partially decompose. In addition, the susceptibility of the sample reduced in hydrogen shows a very broad transition at $T_{peak} \simeq 100$ K, which has a peak amplitude much smaller than that expected for a sample with $T_{peak} = 100$ K.

The above results suggest that Argon does not provide a sufficiently reducing atmosphere compared to vacuum annealing in the tube furnace, while hydrogen is too destructive. As shown in the previous section, vacuum annealing is very effective at removing oxygen from $Bi_2Sr_2CoO_{6+\delta}$. Unfortunately, the TGA is not designed for vacuum measurements. Therefore, we use the TGA only as a sensitive balance for measuring the mass of samples before and after they are annealed in the tube furnace.

The temperature and ambient conditions in the TGA furnace can be maintained over long periods of time, providing an accurate balance. To test the reproducibility of the TGA balance, mass measurements were made of the same sample at 1 hour, 6 hour and 24 hour time intervals. For each measurement, the sample was loaded into the balance, the mass was measured at 120 C and then the sample was removed. Argon gas was flowed through the furnace to keep the sample and furnace dry. The mass measurements had a standard deviation of 0.003 mg for a 71.088 mg sample. For reference, the mass loss expected for a 71 mg, $\delta = 0.4$ sample reduced to a $\delta = 0.25$ sample is about 0.23 mg. Thus, the fluctuations of the TGA balance were relatively small compared to the expected change in mass resulting from oxygen loss.

The TGA was maintained at 120 C in a flow of argon gas for the duration of the anneal. Small pieces of single crystal, with a total mass of 30-70 mg, were first rinsed in isopropanol to remove any loose particles. After the samples were dry, they were loaded into the TGA balance with a rubber suction tip. (The suction tip was used to avoid chipping the delicate crystals with tweezers.) It was important to wait about 15 minutes after loading the sample to allow the TGA balance to stabilize. The samples were then placed in an alumina crucible and annealed in vacuum in either the quartz tube furnace or the CMSE carbon furnace. When the carbon furnace was used, it was best to sandwich the samples between "sacrificial" layers of $Bi_2Sr_2CoO_{6+\delta}$. These layers prevented the surface of the inner samples from reacting during the anneal. For example, we found that the mass loss

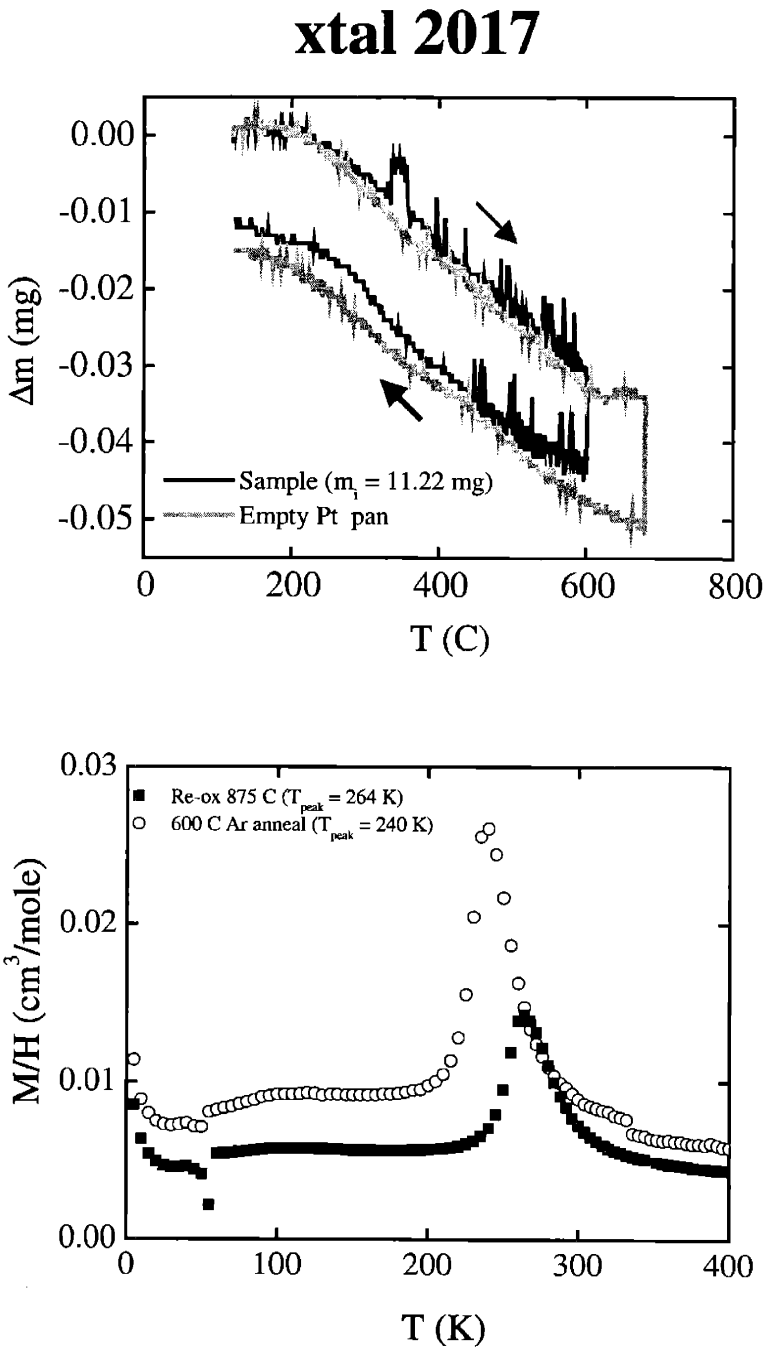

Figure 3-9: (a) TGA trace of a re-oxidized crystal annealed in argon. The heating and cooling rates are 10 C/min and the sample is held at 675 C for two hours. (b) Comparison of the susceptibility before (closed squares) and after (open circles) the argon anneal.

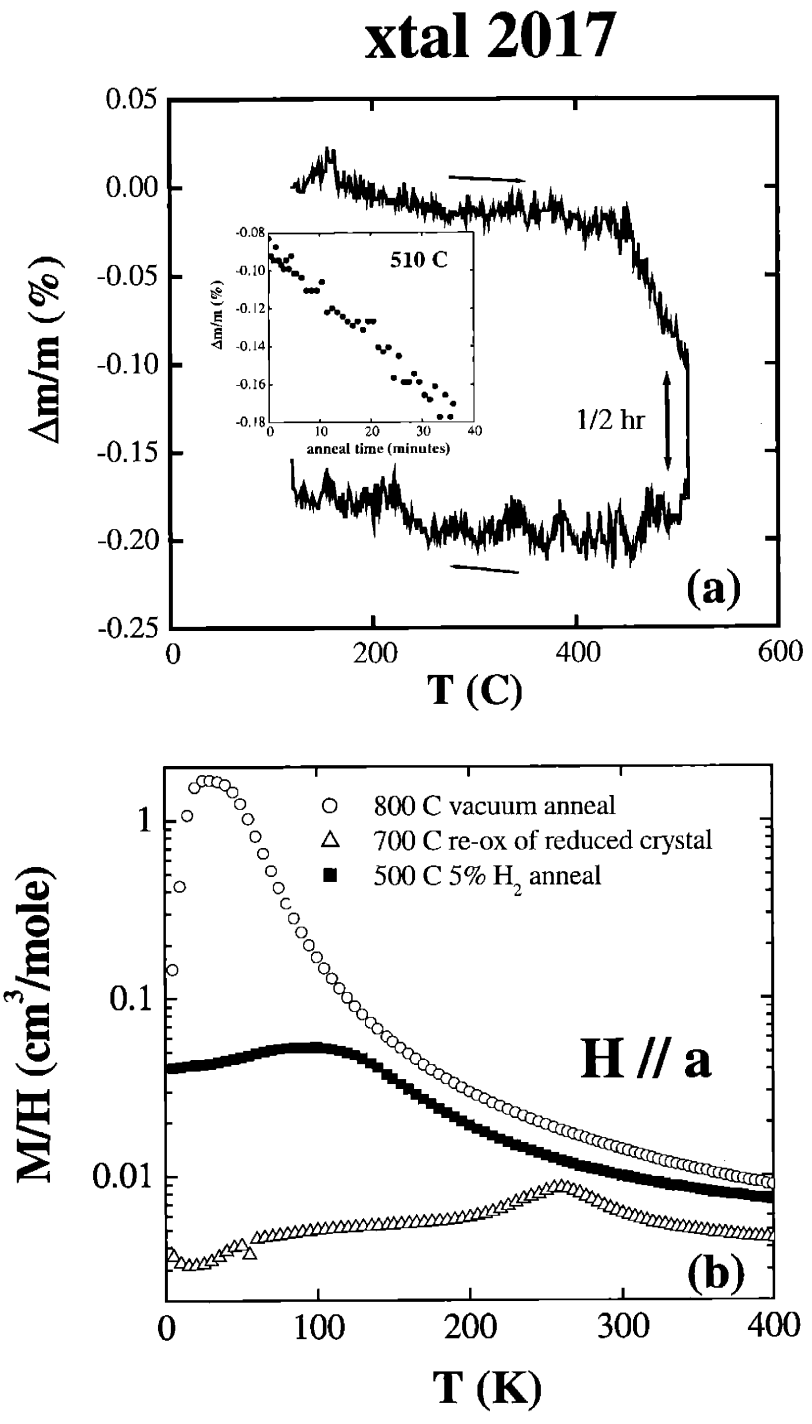

Figure 3-10: (a)TGA trace in 5%H_2/95% He of a re-oxidized crystal. The inset shows the mass as a function of time during the constant temperature anneal. (b) Comparison of the susceptibility before (open circles) and after the re-oxidation (open triangles) and after the reduction (closed squares) in hydrogen. The susceptibility is plotted on a semi-logarithmic scale. The susceptibility of the sample reduced in hydrogen is much smaller than expected for a sample with a magnetic transition near 100 K.

xtal name	initial T_{peak} (K)	final T_{peak}	% mass loss	Comments
S0	240	240	0	-
S1	240	150	0.12	600 C, 12 hrs. QT
S2	240	30	0.60	C furnace 700 C; discolored
S3	240	30	0.49	C furnace 700 C; sac. layers

Table 3.2: Percent mass losses for different vacuum anneals. C indicates the anneal was performed in the carbon furnace and QT indicates annealing in the turbo-pumped quartz-tube furnace.

was nearly 20% larger in samples for which no sacrificial layers were used. In addition, these samples showed discolored surfaces, indicating reaction on the surface.

Table 3.2 shows the percent mass decrease after the vacuum anneal for each of the samples used in these measurements for each annealing profile.

In the reduction measurements, we obtain the reference sample with $\delta \sim 0.25$ (sample S3 in Table 3.2 by annealing an as-grown sample at 700-800 C in vacuum. The oxygen content, δ, of the as-grown crystal is therefore,

$$\delta = 0.25 + \Delta\delta$$

Let m_i and m_f equal the mass of the sample before and after the vacuum anneal and let $\Delta m = m_i - m_f$. Then, $\Delta\delta$ is related to the mass-loss resulting from the vacuum anneal by,

$$\Delta\delta = \frac{\Delta m}{m_f} \times \frac{752 g/mole}{16 g/mole} \tag{3.4}$$

The percent mass loss measured in sample S3 is 0.49%. This yields $\Delta\delta$ equal to 0.23 moles of oxygen. Therefore, the as-grown crystal with $T_N = 240$ K has $\delta = 0.48$. This is close to the value of $\delta = 0.51$ determined for a sample with $T_{peak} = 270$ K in the oxidation method. Once δ of the as-grown crystal is known, the δ of samples obtained by annealing the as-grown sample in vacuum can be determined as well. Figure 3-11 shows T_{peak} as a function of δ. The experimental error bars correspond to the standard deviation in the mass measured above.

In this thesis, we use T_{peak} as the primary indicator of oxygen content. This is because T_{peak} is easier to measure than δ, and samples which have the same T_{peak} share, qualitatively and quantitatively, the same magnetic properties. Based on the above analysis, our

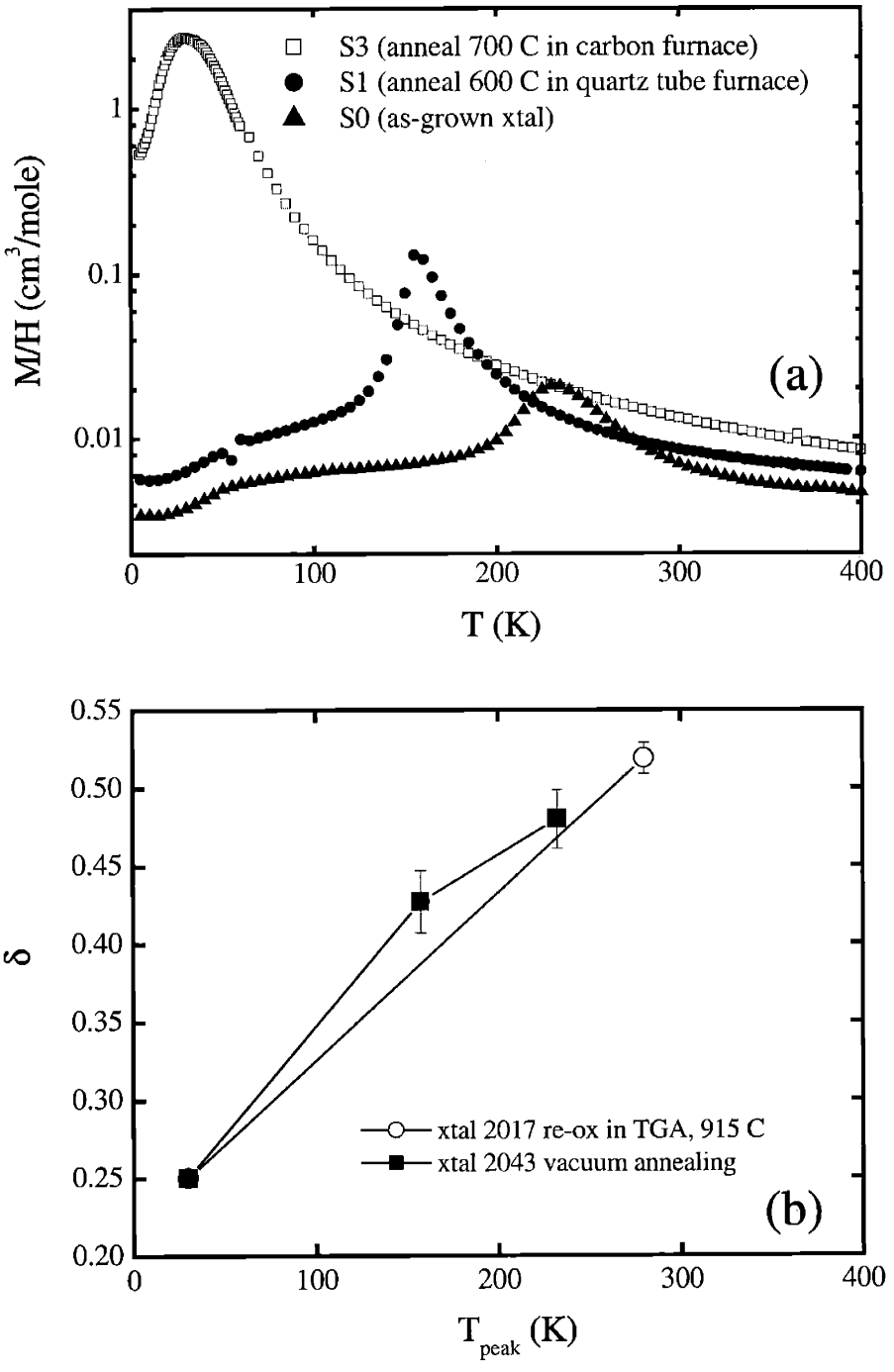

Figure 3-11: (a) Susceptibility curves for different vacuum annealing temperatures. (b) δ as a function of T_{peak}.

assumption is that a sample with T_{peak} close to 25 K has a $\delta \sim 0.25$ and a sample with $T_{peak} \sim$ 240-270 K has a $\delta \sim 0.5$.

Chapter 4

Magnetic properties of $Bi_2Sr_2CoO_{6+\delta}$ as a function of δ

In this chapter, I present the results of susceptibility and neutron scattering measurements performed on single crystals of $Bi_2Sr_2CoO_{6+\delta}$ with $0.25 \leq \delta \leq 0.5$. The chapter is divided into three sections: Sections 4.1 and 4.2 describe the details of the magnetic order occurring in samples with $\delta > 0.4$ and $\delta \simeq 0.25$, respectively. Specifically, we discuss the *antiferromagnetic* order of Co^{3+} spins in samples with $\delta > 0.4$ and the *ferromagnetic* order found in the 50% Co^{2+} - 50% Co^{3+} samples with $\delta \simeq 0.25$. In the third section, we will look at the evolution of the magnetic behavior in samples with δ ranging from 0.25 to 0.5. The results of our neutron scattering measurements suggest co-existence of antiferromagnetic and ferromagnetic regions in these samples. The reason for dividing the chapter up in this way is to make clear which features are unique to the antiferromagnetic, $\delta \simeq 0.5$ phase and ferromagnetic $\delta \simeq 0.25$ phase, and which features result from the co-existence and interaction between the two phases in samples with $0.25 < \delta < 0.5$.

4.1 Antiferromagnetic order in $Bi_2Sr_2CoO_{6+\delta}$, $\delta > 0.4$

As discussed in Chapter 3, as-grown crystals of $Bi_2Sr_2CoO_{6+\delta}$ are oxygen rich with $0.4 < \delta < 0.5$ and the average oxidation state of the Co ions in these samples is therefore close to 3+. In these samples, a transition to antiferromagnetic order of the Co^{3+} spins occurs at $T_N \sim 250$ K. The precise T_N depends on the oxygen content, which varies slightly with the sample preparation.

Prior to our work, only powder samples of $Bi_2Sr_2CoO_{6+\delta}$ were studied with neutron diffraction.[12] The powder data indicated an antiferromagnetic ordering of nearest-neighbor spins in the ab plane. However, the authors suggested that the spin direction in the magnetically ordered phase below T_N was along the orthorhombic b-axis.[12]

Our measurements of single-crystals show that the spins in the ordered phase are instead aligned along the a-axis.[1] Since the result that the antiferromagnetic spin lies along **a** and not **b** is critical to our interpretation of the magnetic properties, I will spend some time explaining how the antiferromagnetic structure is determined through a series of neutron scattering measurements.

The analysis is based on the results of neutron scattering measurements performed in zero-field in the (0KL) and (H0L) scattering planes. Although field dependence measurements indicate that these samples contain finite amounts of the ferromagnetic phase, the magnetic properties are dominated by the antiferromagnetic phase. Therefore, we will assume that these samples closely approximate the "pure", Co^{3+} free antiferromagnet.

4.1.1 Determining the spin structure

In an antiferromagnet, the magnetic moments order such that there is zero microscopic moment below the transition temperature. Although the magnetic susceptibility may indicate the transition temperature and the presence of any magnetic anisotropies in the spin ordering, neutrons are necessary to determine the microscopic structure in the antiferromagnetic phase.

In Chapter 2, we showed that the cross-section for magnetic scattering in a non-Bravais lattice is proportional to

$$[\sum_d \langle \mathbf{S_d} \rangle f_d(\mathbf{Q}) e^{i\mathbf{Q}\cdot\mathbf{d}} (1 - \hat{\mathbf{Q}} \cdot \hat{\mathbf{S}})]^2 \tag{4.1}$$

The sum in 4.1 is over the four spins in the structural unit cell, which are at the positions 000, $\frac{1}{2}\frac{1}{2}0$, $\frac{1}{2}0\frac{1}{2}$ and $0\frac{1}{2}\frac{1}{2}$ with respect to the orthorhombic axes. The schematic in Figure 4-1 indicates the orthorhombic unit cell and the four unique Co spin positions.

To determine the particular spin arrangement occurring in $Bi_2Sr_2CoO_{6+\delta}$, one compares the measured positions of the magnetic Bragg peaks with those allowed for a particular spin

[1] Since a and b are nearly equal in $Bi_2Sr_2CoO_{6+\delta}$, it is difficult to distinguish them in a powder measurement. This is particularly true at the low values of 2θ where magnetic scattering is most prominent.

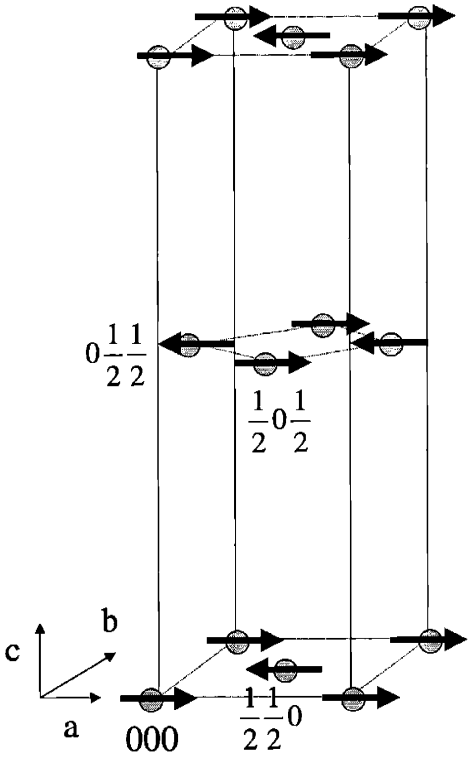

Figure 4-1: Spin structure in the antiferromagnetic phase. One orthorhombic unit cell is shown, indicating only the Co sites.

arrangement. Figure 4-2 shows the intensity of the magnetic Bragg peaks in the *ac* [Figure 4-2(a)] and *bc* [Figure 4-2(b)] planes. The data in (a) are from a measurement of xtal 1955, which has a T_N of 235 K and the data in (b) are from xtal 2043, which has a T_N of 225 K. In Fig. 4-2(a), there are only peaks at the positions (1, 0, L = *odd*) while in Fig. 4-2(b), there are only peaks at the positions (0, 1, L = *even*). (The intensity of the peaks also has an L dependence, which I will discuss below.) Thus, the allowed reflections are H, L = *even* and K = *odd* and H, L = *odd* and K = *even*. The allowed reflections are consistent with a model in which nearest neighbor spins in the plane are anti-parallel and nearest neighbor spins out of the plane are parallel. This spin arrangement is shown in Figure 4-1.

The geometric factor, $(1-\hat{\mathbf{Q}}\cdot\hat{\mathbf{S}})$, allows one to determine the *direction* of the spins. The geometric factor is maximal when **Q** and **S** are 90° with respect to one another and equals zero when **Q** and **S** are parallel. Looking at Figures 4-2(a) and (b), we see that in the scan along L through (1, 0, L), the scattering amplitude approaches zero as the component of **Q** along the *a*-axis increases, while in the scan along (0, 1, L), the intensity is greatest when **Q** and **b** are parallel. The data confirms that the spins point along **a**.

There is an additional effect on the Q dependence of the intensity which results from

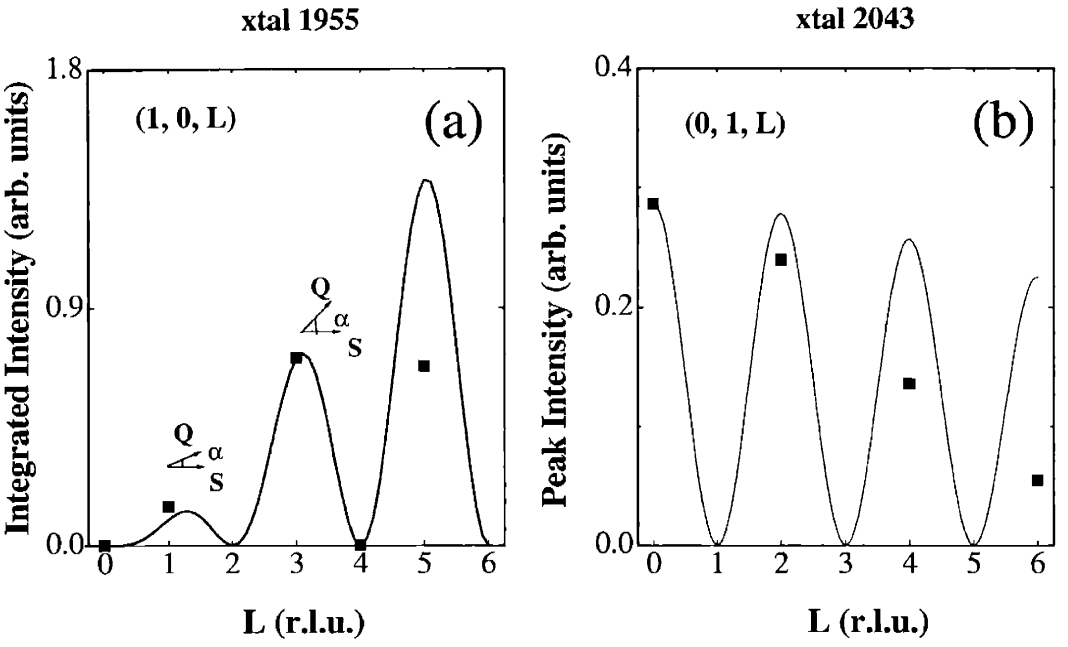

Figure 4-2: Scan through the antiferromagnetic reflections in the (a) *ac* (xtal 1955, T_N = 235 K) and (b) *bc* (xtal 2043, T_N = 225 K) planes. In (a), α is the angle between **Q** and **S**, which increases with increasing L. The data in (a) are *integrated* intensities, while the data in (b) are *peak* intensities. The dark lines are curves proportional to $\frac{1}{sin(2\theta)}[f_d(Q)\sum_d\langle\hat{\mathbf{S}}\rangle(1-\hat{Q}\cdot\hat{S})e^{i\mathbf{Q}\cdot\mathbf{d}}]^2$.

the form factor, *f(***Q***)* and the Lorentz factor, $\frac{1}{\sin(2\theta)}$. *f(***Q***)* decreases from about 0.9 at the (0, 1, 0) reflection to 0.7 at the (0, 1, 5) reflection. On the other hand, $\sin(2\theta)$ increases from 0.4 to 0.7.

The dark lines in Figures 4-2 (a) and (b) are curves proportional to

$$\frac{1}{sin(2\theta)}[f_d(\mathbf{Q})\sum_d\langle\hat{\mathbf{S}}\rangle(1-\hat{\mathbf{Q}}\cdot\hat{\mathbf{S}})e^{i\mathbf{Q}\cdot\mathbf{d}}]^2 \tag{4.2}$$

where *f(***Q***)* is the form factor calculated for Co^{3+}.[30]

One final point regarding the data in Figure 4-2 (a) is the sharp drop off in the intensity at the position (1, 0, 5). This is probably due to an incomplete vertical integration of the scattered neutrons at this high Q position. Incomplete integration is most pronounced for samples, such as xtal 1955, which have a large mosaic. On the other hand, the data in 4-2(b) correspond to the peak heights of the (0, 1, L) scans, since we do not have measurements of the integrated intensity for these reflections. The drop off in intensity with increasing L reflects a worsening of the resolution in the plane due to the mosaic.

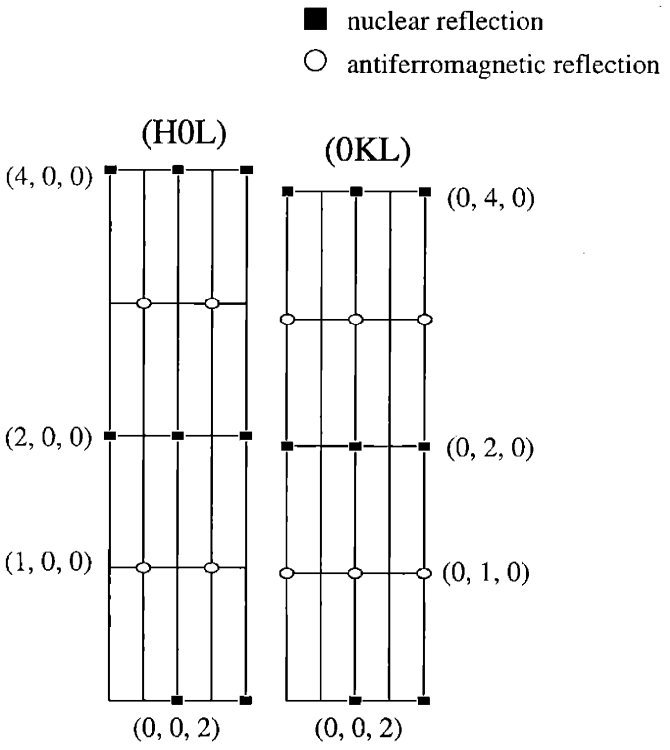

Figure 4-3: Allowed nuclear and antiferromagnetic Bragg reflections in the (H0L) and (0KL) scattering planes. The super-lattice reflections resulting from the structural modulation along **a** are not shown.

The allowed nuclear and magnetic reflections in the (0KL) and (H0L) scattering planes are summarized in Figure 4-3. Note that antiferromagnetic and nuclear peaks occur at different positions in reciprocal space.

4.1.2 Temperature dependence of the antiferromagnetic order

The integrated intensity of the (1, 0, 1) antiferromagnetic Bragg peak in xtal 1955 as a function of temperature is shown in Figure 4-4a. The intensity of the Bragg peak is proportional to the square of the ordered moment, $\langle S_{AF} \rangle$ on a Co site. In the vicinity of the transition, the curve should follow a power law behavior, $\langle S_{AF} \rangle^2 \simeq \mid T_c - T \mid^{2\beta}$, where the exponent β depends on the details of the spin Hamiltonian. To account for the rounding of the data near the transition temperature, an order parameter fit function with a Gaussian distribution of transition temperatures is used to fit the data for temperatures greater than 150 K.[2] Unfortunately, the substantial rounding at the transition prevents a

[2]At temperatures well below T_N, extinction effects cause the order parameter data to appear to flatten rapidly with temperature. This will lead to an artificially low β

precise fit of the exponent, β. Therefore, three fits, all of which have $\chi^2 \leq 1$, are shown in the figure. The dark solid line is the result of a fit with β fixed at 0.25, the value observed in many 2D square-lattice Heisenberg systems[31], and a fitted T_N of 218 $\pm$ 2. The dotted line is a fit with β fixed at 0.12, the value for the 2D Ising model, and a fitted T_N = 208 $\pm$ 1. Finally, the dashed line is a fit with T_N fixed at 235 K, the transition temperature determined from the susceptibility, and a fitted value of $\beta = 0.425 \pm 0.031$. All of the fits have a Gaussian distribution of Néel temperatures with variance $\sim$ 30 K. For comparison, a simulated curve with $\beta = 0.425$ and $T_N = 235$ K and $\sigma = 1$ K is also shown.

The magnitude of the ordered Co^{3+} moment, $\langle M_{AF} \rangle$, is estimated by normalizing the AF peak to the nuclear (0, 0, 2) reflection, which has a known cross-section.[12] We estimate $\langle M_{AF} \rangle = 2.5 \pm 0.8\ \mu_b$/Co resulting in $\langle S_{AF} \rangle = 1.3 \pm 0.4\ \mu_b$/Co, assuming $g = 2$. The estimated moment is therefore closest to the intermediate spin state, $S = 1$, of the Co^{3+} ion in an octahedral crystal field. Preliminary spin wave measurements provide an estimate of $\sim$ 13 meV for the in-plane AF exchange interaction (using $\langle S_{AF} \rangle = 1.3$).

At temperatures above T_N, neutrons reveal the two-dimensional nature of the magnetic order in $Bi_2Sr_2CoO_{6+\delta}$. If the magnetic interaction between nearest-neighbor spins in the plane, J_{NN}, is much greater than the inter-plane coupling, $J_\perp$, then the spin interaction may be described as two-dimensional. True long-range order will not occur except at T = 0 in a purely two-dimensional system. However, the presence of a small inter-plane coupling or anisotropy will break the pure two-dimensionality of the spin interaction and the spins will order at finite temperature.

In a 2D system, the correlation length in the plane will start to grow at temperatures greater than the transition temperature to long range order. Roughly, the in-plane correlation length will grow above one lattice constant when $k_bT \sim J_{NN}S^2$. Recalling that the neutron cross-section is proportional to the spatial Fourier transform of the magnetic order, 2D magnetic correlations in real space will appear as rods of scattering in reciprocal space. When the in-plane correlation length is sufficiently large, the effective interaction between layers will result in long range order of the spins. As the temperature approaches T_N from above, the growth of the in-plane correlation length is reflected by a narrowing of the rod in Q. At the Néel transition, the rod breaks up into Bragg "points", reflecting true long range order.

Figure 4-4(b) shows the peak intensity of a scan through the 2D rod of antiferromagnetic

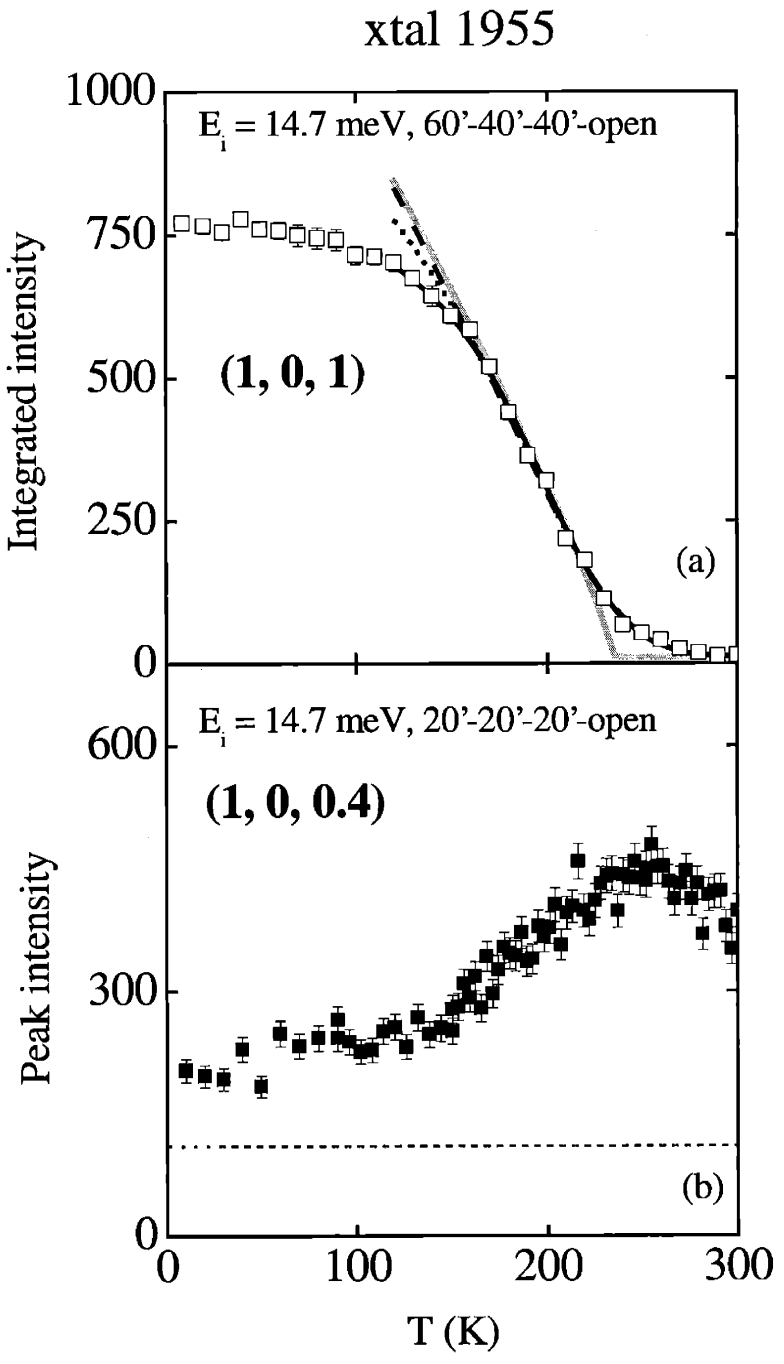

Figure 4-4: (a) Integrated intensity at the (1, 0, 1) antiferromagnetic reflection measured as a function of temperature. The three dark curves are fits of the data, for T > 150 K, to an order parameter function with a Gaussian distribution of transition temperatures. The curves correspond to a fit with β fixed at 0.12 (solid dark line), β fixed at 0.25 (dotted line), and T_N fixed at 235 K (dashed line). The solid gray line is a simulated curve with T_N = 235 K and β = 0.425, with the Gaussian distribution forced to equal 1 K. (b) Peak intensity of a scan through the rod of 2D AF scattering as a function of temperature; the dashed line is the background, measured at (1.077, 0, 0.4) at 30 K.

scattering. The spectrometer geometry is chosen so that the detector integrates over all energy transfers from the fluctuating spin system[32]. Thus, the measurement in Figure 4-4(b) constitutes a "snapshot" in time of the 2D spin-correlations. The intensity of the rod increases with decreasing temperature above T_N because of the growing in-plane correlation length. Below the transition to 3D order, the fluctuations are frozen out and the intensity of the 2D rod decreases.

The slow decrease in intensity with decreasing temperature is similar to that found in the Heisenberg antiferromagnet La_2CuO_4.[31] In a Heisenberg system, the transition to long-range order is driven by the coupling between the layers, while in an Ising system, such as K_2NiF_4, long-range order is driven by the spin anisotropy.[33] As a result, the reduction in the quasi-elastic intensity in Ising systems is a more rapid function of temperature than in Heisenberg systems. However, it should be stressed that the rounding of the data at the Néel transition in our samples prevents us from making definitive statements about the symmetry of the spin Hamiltonian.

The observation of 2D correlations in $Bi_2Sr_2CoO_{6+\delta}$ is not surprising considering the crystal structure. The large c-axis lattice constant should result in a smaller exchange coupling between nearest-neighbor spins in adjacent layers than in the same layer. This is due to the fact that the super-exchange depends on the overlap of the electron orbitals with the bridging oxygen ions. This overlap will be much smaller perpendicular to the layers than within the layers. An additional factor contributing to the two-dimensionality of $Bi_2Sr_2CoO_{6+\delta}$ is the nearly tetragonal crystal structure, which frustrates the spin interaction between adjacent layers.

4.1.3 Susceptibility

The temperature dependent susceptibility of the same sample used for the neutron studies is shown in Figure 4-5. Since the susceptibility measurements are performed on a single crystal, it is possible to separately measure χ_a, χ_b and χ_c.

The susceptibility exhibits a large in-plane anisotropy: both χ_a and χ_b are much greater than χ_c. The anisotropy is consistent with our observation that the spin lies along the a-axis. In addition, χ_a and to some extent χ_b exhibit glassy behavior at low temperatures.

The most prominent feature in the susceptibility is the ferromagnetic-like peak in χ_a, occurring at $T_{peak} = 235$ K in this sample. The peak in the susceptibility coincides with

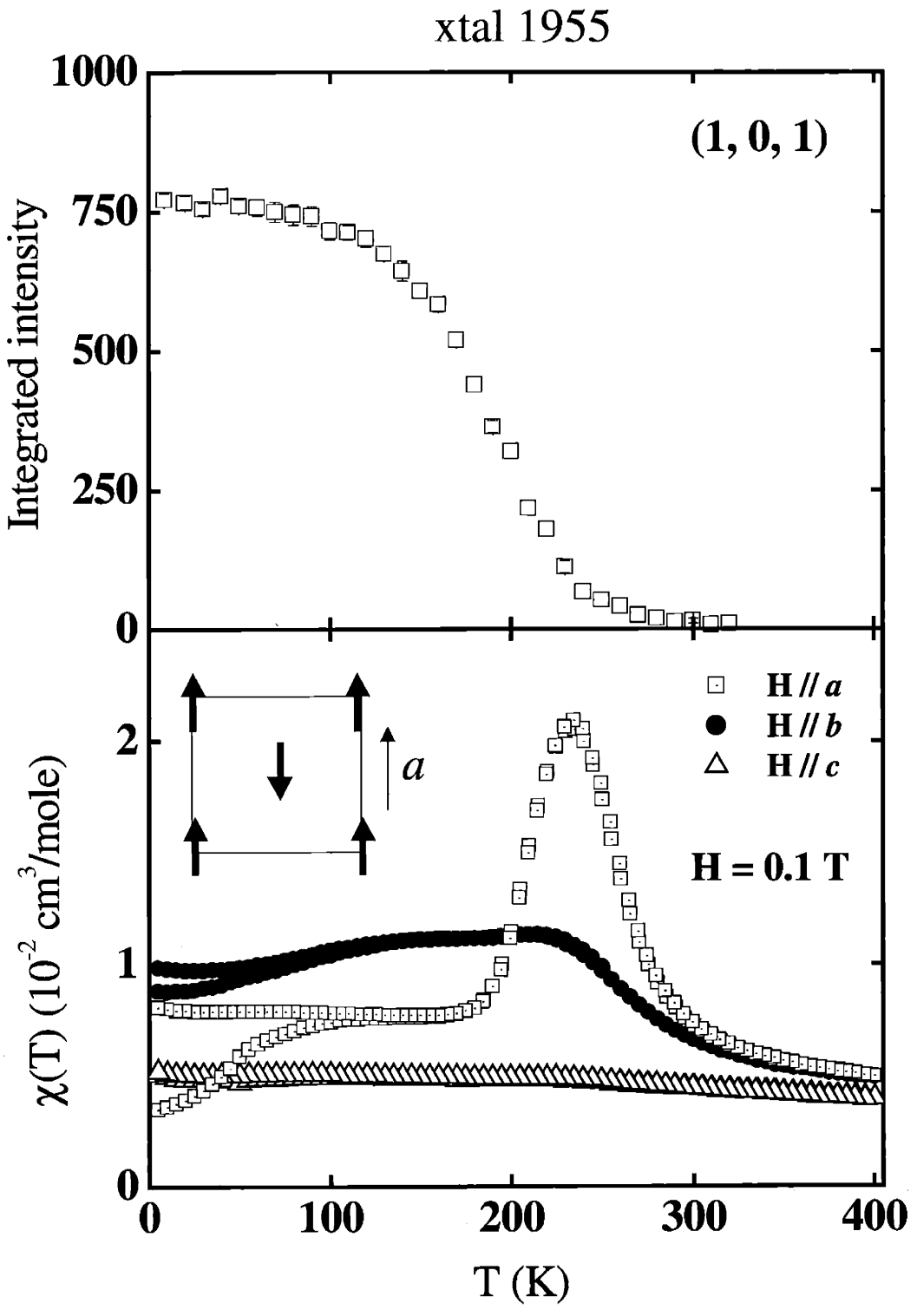

Figure 4-5: Comparison between the temperature dependent magnetic susceptibility along **a**, **b**, and **c** (bottom panel) and the onset of ordering of the antiferromagnetic sub-lattice in xtal 1955. The graphical inset shows the a-axis relative to the antiferromagnetic spin direction. The susceptibility for field cooling and zero-field cooling is shown for all of the samples, but the thermal hysteresis is most pronounced when the field is along **a**.

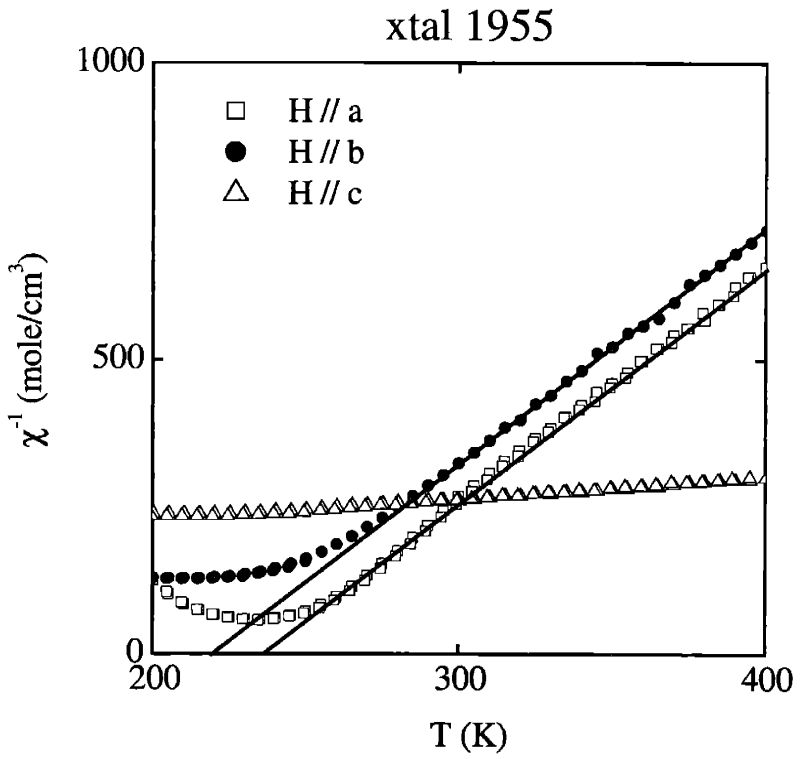

Figure 4-6: The inverse susceptibility of xtal 1955 is plotted as a function of temperature, after subtracting the temperature independent susceptibility, χ_0. The fitted χ_0s from the 300-400 K range fits are used. The curves are linear above the transition temperature, suggesting that the susceptibilities follow the Curie-Weiss temperature dependence. Note that χ_a and χ_b have the same slope, but slightly different (negative) Curie-Weiss temperatures, while χ_c has a much smaller slope than χ_a or χ_b and a positive Curie-Weiss temperature.

the transition temperature observed with neutrons. This can be seen in a comparison of the susceptibility curve with the order parameter data measured with neutrons, which is shown in the top panel of Figure 4-5. In addition, fixing T_N at 235 K results in a good fit of the data in Figure 4-4 to the order parameter fit function. Therefore, we will identify T_{peak} as T_N.

It is instructive to fit the susceptibility for $T > T_{peak}$ to a Curie-Weiss form,

$$\chi(T) = \frac{C}{T - T_c} + \chi_0 \tag{4.3}$$

where χ_0 is a temperature independent susceptibility and C is the Curie constant.

$$C = \frac{N_A \mu_b^2 \mu_{eff}^2}{3k_b} \tag{4.4}$$

For magnetism resulting from uncorrelated spins with spin S, $\mu_{eff} = gS(S+1)$. A fit of χ_a and χ_b to a Curie-Weiss form is quite good and the fit parameters are shown in Table

axis	Fit range (K)	C (cm^3 K /mole)	μ_{eff}	χ_0 (cm^3/mole)	Θ (K)
a	300-400	0.257 ± 0.008	1.434 ± 0.008	0.00343 ± 0.00004	231.5 ± 1.9
	350-400	0.23 ± 0.06	1.35 ± 0.06	0.0035 ± 0.0002	241 ± 17
b	300-400	0.25 ± 0.01	1.41 ± 0.01	0.00348 ± 0.00005	219 ± 2
	350-400	0.39 ± 0.3	0.8-1.8	0.0031 ± 0.0008	181 ± 72
c	300-400	2.5 ± 0.3	4.54 ± 0.1	0.0006 ± .0002	-375 ± 42

Table 4.1: Parameters from the fits of the susceptibility of xtal 1955 (T_N = 235 K) to a Curie-Weiss form.

4.1. The susceptibility along **c** is also fit, though the fitting is difficult because the data show little variation with temperature above T_{peak}.

To show the quality of the fits, the data are plotted in Figure 4-6 as $1/\chi$ vs T, after subtracting the fitted temperature independent susceptibility, χ_0. The fits of χ_a and χ_b yield ferromagnetic Curie-Weiss temperatures, T_c, which have magnitudes $\approx T_{peak}$. The fit of χ_c yields an antiferromagnetic (T_c ¡ 0) Curie-Weiss temperature. In addition, the fluctuating moment μ_{eff} determined by the fit of χ_c is much larger than that found for either χ_a or χ_b. This may indicate an anisotropy in the g-factor of Co, though the in-plane g factor is usually larger than that for the out-of plane g-factor.[34]

The Curie-Weiss fits should be interpreted carefully, however, because the range of the fit is quite close to the transition temperature. In addition, the Curie-Weiss susceptibility is a mean field expression which ignores the correlations between spins. Given the observation that 2D correlations exist above T_N, it is surprising that the Curie-Weiss form fits the data so well. Note also the difference in sign between the fitted Curie temperature and that expected for AF exchange and the small magnitude of μ_{eff} in the fits of χ_a and χ_b (for S = 1 and g = 2, one expects μ_{eff} = 2.8). Only χ_c has a Curie-Weiss temperature which is antiferromagnetic.

The most surprising observation, however, is that the ferromagnetic peak is largest when the field is along **a**, the antiferromagnetic spin direction. In some antiferromagnets, the antiferromagnetic spins cant, forming a small FM moment *perpendicular* to the staggered moment. The fluctuation of the canted moment at high temperatures results in a cusp-like peak in the susceptibility at T_N. This is observed, for example, in antiferromagnetic La_2CuO_4 and results in a pronounced cusp in the susceptibility at T_N.[35] However, the canting resulting from such a mechanism is perpendicular to the AF spin direction, while

in $Bi_2Sr_2CoO_{6+\delta}$, the enhanced susceptibility is strongest *along* the AF spin direction. Furthermore, for ferromagnetism resulting from canting, the size of the canted moment should be intrinsic to the antiferromagnetic order. As I will show in Section 4.3, the size of the FM peak grows as T_N is suppressed, whereas one would expect the staggered moment, and therefore the canted moment, to decrease as T_N decreases.

In section 4.3, I will present evidence that the FM peak results from the presence of a distinct FM phase, which co-exists with the AF phase and orders at T_N.

4.2 Ferromagnetism in $Bi_2Sr_2CoO_{6+\delta}$ with $\delta \simeq 0.25$

In this section, we discuss the magnetic order in the most oxygen depleted samples. These samples have $\delta \simeq 0.25$ and are therefore expected to have an equal concentration of Co^{2+} and Co^{3+}. The transition to antiferromagnetic order, characteristic of the $\delta \sim 0.5$ samples, is not observed in these samples. This is indicated by the absence of temperature dependent magnetic Bragg peaks at the (0, 1, L) positions. Rather, these highly reduced samples exhibit predominantly ferromagnetic behavior.

In the next section, we will see that understanding the field dependence of the pure, $\delta \simeq 0.25$ ferromagnetic phase is important for interpreting the field dependence of samples with intermediate doping ($0.25 < \delta < 0.5$). The zero-field state of the $\delta \simeq 0.25$ samples is not a true ferromagnet with a uniform moment on each Co site. Although the in-plane coupling between neighboring spins is ferromagnetic, the coupling between layers appears to be antiferromagnetic. As a result of the inter-plane antiferromagnetic coupling, the uniform moment vanishes at zero-field. The inter-plane coupling appears to be weak and is easily destroyed in a small magnetic field (< 0.5 Tesla). In addition, the weak coupling results in only short-range correlations perpendicular to the layers.

4.2.1 $\delta \simeq 0.25$ samples

Susceptibility and field dependent neutron scattering measurements were performed on two single crystals with $\delta \simeq 0.25$. Xtal 1974C had a $T_{peak} = 48$ K and showed no trace of the antiferromagnetic Bragg peaks found in samples with $\delta \sim 0.5$. Unfortunately, we did not do a complete search in Q for FM peaks at zero-field in this sample. In addition, this crystal had a fairly poor mosaic. In a later experiment, we looked at xtal 2043an800C, which had

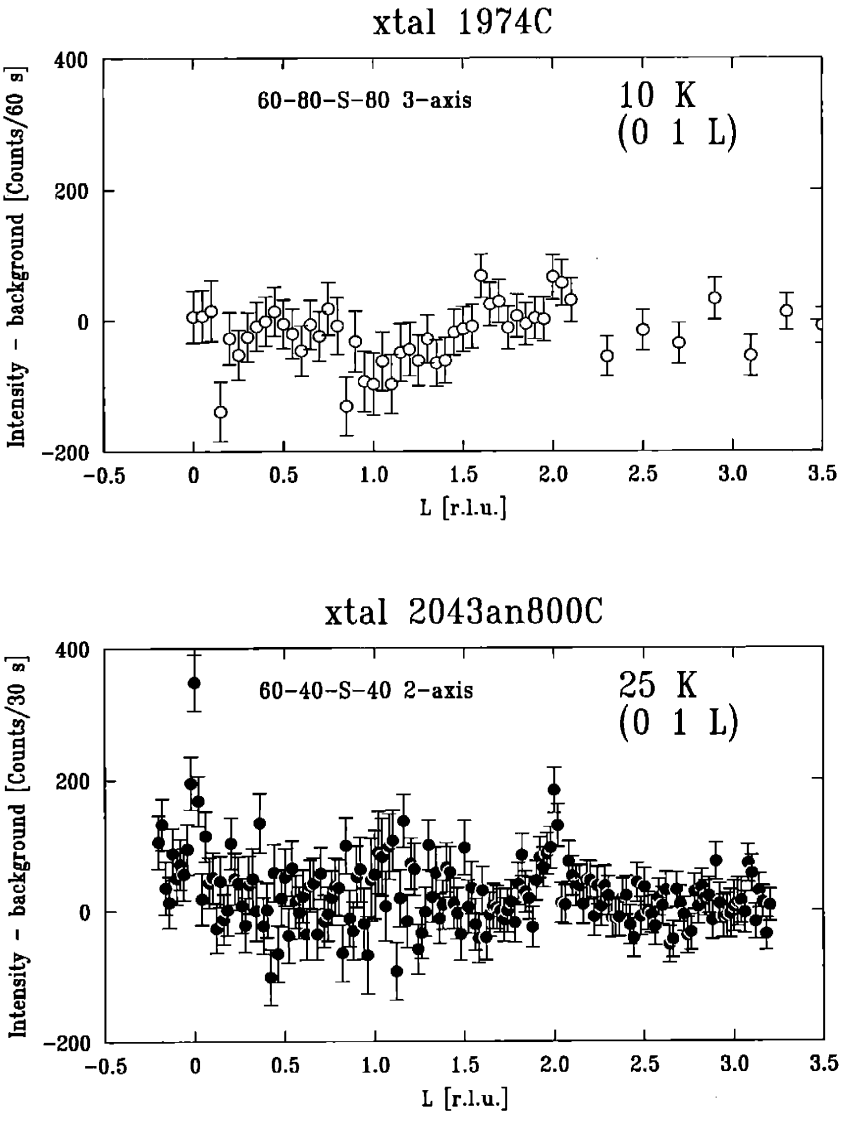

Figure 4-7: Scans at zero-field along (0, 1, L) in crystals 1974C (top panel) and 2043an800C (bottom panel). A temperature independent background has been subtracted from both scans. In xtal 1974C, no peaks are observed at the AF positions (0, 1, L = *even*). In xtal 2043an800C, small peaks are observed at (0, 1, L = *even*).

an excellent mosaic. This sample had a T_{peak} equal to 25 K, which is the lowest T_{peak} we have been able to obtain by vacuum annealing. However, this sample may have contained traces of the antiferromagnetic, $\delta \sim 0.5$ phase.

Neutron scattering scans along L through (0, 1, L) are shown for both xtals 1974C and 2043an800C in Figure 4-8. The plots show the difference between scans taken at a temperature below T_{peak} and at a temperature above T_{peak}. There are no antiferromagnetic Bragg peaks along (0, 1, L) in xtal 1974C, while in xtal 2043an800C, there is some weak scattering at the (0, 1, 0) and (0, 1, 2) reflections. The scattering at these peaks is about 100 times smaller than the scattering resulting from the antiferromagnetic order in samples with $\delta \sim 0.5$.

4.2.2 Susceptibility

The temperature dependent magnetic susceptibilities, χ_a, χ_b, and χ_c of crystals 1974C and 2043an800C are shown in Figure 4-8. The susceptibilities of the reduced samples are qualitatively similar to the susceptibility measured in the sample with $\delta \sim 0.5$ and $T_{peak} =$ 235 K (Figure 4-5): there is a large in-plane anisotropy with χ_a and χ_b both exhibiting a cusp-like peak and ferromagnetic-like behavior above the peak.[3] However, the magnitude of the susceptibility at the peak in χ_a in xtals 1974C and 2043an800C is nearly two orders of magnitude greater that that observed in the sample with $T_{peak} = 235$ K. In addition, the peak is no longer associated with an in-plane AF order of the spins.

The susceptibility, χ_a, above the peak is well fit to a Curie-Weiss form, $C/(T - T_c) + \chi_0$, in both samples. The data are fit above 200 K and the fit parameters C, T_c and χ_0 are summarized in Table 4.2. Note that in both samples, the T_c is ferromagnetic ($T_c > 0$) and close to 100 K. In addition, μ_{eff} is 3.93 for xtal 1974C and 5.12 for xtal 2043an800C, which is much larger than what we found in the sample with $T_N = 235$ K. The fluctuating moment, μ_{eff}, is slightly higher in xtal 2043an800C than in xtal 1974C, which may be related to the lower value of T_{peak} found in this sample.

The fitted value of μ_{eff} should be compared to the expected value of μ_{eff} for an equal mixture of Co^{2+} and Co^{3+} ions. We will model the $\delta = 0.25$ system as a two sub-lattice ferromagnet with Co^{3+} ions with spin S_1 on one sub-lattice and Co^{2+} ions with spin S_2 on the other sub-lattice. For a ferromagnetic nearest-neighbor interaction, the spin susceptibility

[3] A peak is also observed in χ_c, but this may result from imperfect alignment.

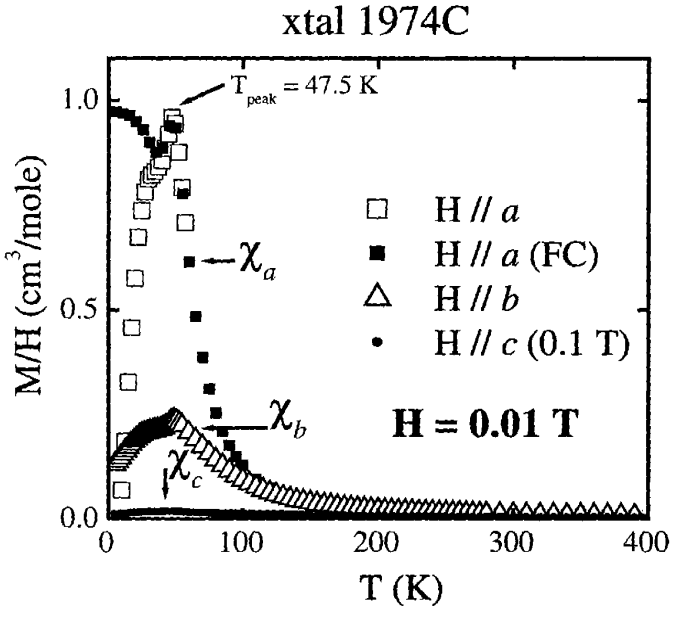

Figure 4-8: Temperature dependent susceptibility of samples with $\delta \simeq 0.25$. The top panel shows χ_a, χ_b and χ_c after cooling in zero-field for xtal 1974C, which has a T_{peak} at 47.5 K. The field-cooled (FC) data are also shown for χ_a. The bottom panel shows the zero-field-cooled (ZFC) susceptibility in xtal 2043an800c, with $T_{peak} = 25$ K. Curves measured in 0.01 T (closed symbols) and 0.1 T (open symbols) fields are shown for each direction to demonstrate the rounding at the transition which occurs with higher field. Note that the 2043an800c xtal has nearly three times the magnitude of the susceptibility at the peak as xtal 1974C.

Sample	C (cm^3 K /mole)	μ_{eff} (μ_b/Co)	T_c (K)	χ_0 ($10^{-4}cm^3$/mole)
xtal 1974C	1.94 ± 0.05	3.93 ± 0.05	99 ± 2	-4 ± 1.7
xtal 2043an800C	3.28 ± 0.05	5.12 ± 0.04	100 ± 1	14 ± 1

Table 4.2: Parameters from the fits of χ_a above 200 K to a Curie-Weiss form, C/(T - T_c) + χ_0.

above T_c reduces to,

$$\chi(T) = \frac{C_1 + C_2}{T - T_c} \tag{4.5}$$

$$= \frac{N\mu_{eff}^2}{3k_b(T - T_c)} \tag{4.6}$$

Where[4],

$$C_i = \frac{N}{2}(g\mu_b)^2(S_i)(S_i + 1) \tag{4.7}$$

$$\mu_{eff}^2 = \frac{g^2}{2}(S_1(S_1 + 1) + S_2(S_2 + 1)) \tag{4.8}$$

The spin on the Co^{2+} can be either S = 1/2 or S = 3/2, while the spin on the Co^{3+} ion can be either 0, 1 or 2. Table 4.3 summarizes the expected values of μ_{eff} for all possible combinations of the Co^{2+} and Co^{3+} spin states, assuming a g-factor of 2. In xtal 1974C, the fitted value of μ_{eff} thus falls between that of the S = 2 and S = 1/2 mixture and the S = 2 and S = 3/2. The fitted value of μ_{eff} for xtal 2043an800C is actually closest to the equal mixture of Co^{3+} in the S = 2 state and Co^{2+} in the S = 3/2 state. We note that the μ_{eff} expected for Co^{2+} in the S = 1/2 state and Co^{3+} in either the S = 0 or S = 1 state is significantly smaller than the fitted values of μ_{eff} found in either sample.

The susceptibilities of these reduced samples exhibit thermal hysteresis below 20 K, which is qualitatively similar behavior to that observed in the sample with T_N = 235 K. The hysteresis is only pronounced at small fields and low temperatures; consequently, most of the field dependence measurements described below are performed above 20 K to avoid the hysteresis.

[4]It should be noted that if S_1 or S_2 = 0, the mean field picture above should be replaced by C/(T-T_c), where C is the Curie susceptibility of the non-zero spin and the interaction results from next-nearest neighbor interactions.

S_1	S_2	$\mu_{eff} = \frac{g}{\sqrt{(2)}}((S_1)(S_1+1)+(S_2)(S_2+1))^{1/2}$	$M_{sat} = \frac{g}{2}(S_1+S_2)$
0	1/2	1.22	1/2
1	1/2	2.35	3/2
0	3/2	2.73	3/2
1	3/2	3.39	5/2
2	1/2	3.67	5/2
2	3/2	4.42	7/2

Table 4.3: Calculated values of μ_{eff} and M_{sat} for different spin states of $Co^{3+}$and Co^{2+}. μ_{eff} and M_{sat} are calculated assuming g = 2.

4.2.3 Field dependence: bulk susceptibility measurements

The susceptibility measurements suggest a ferromagnetic transition at a $T_c \sim 100$ K in the $\delta \simeq 0.25$ samples. However, we do not observe the onset of a spontaneous uniform moment when the sample is cooled in zero-field; below T_{peak}, the moment falls to zero. Here, we discuss field-dependence measurements which suggest ferromagnetism, despite the absence of a spontaneous uniform moment at zero field.

In Figure 4-9, the uniform moment as a function of field is shown for temperatures 30 K, 60 K and 200 K in xtal 1974c and at 30 K in xtal 2043an800c. The field scans are performed with the field applied along **a**, the direction which shows the largest ferromagnetic susceptibility. In addition, the field-scans are taken above the temperature range where thermal hysteresis is observed.

The field dependence of the moment, M(H), at 30 K exhibits the characteristic sigmoidal shape found in ferromagnets. The large moment at 5 Tesla suggests nearly full polarization of the spins: the moment at 5 Tesla is 1.5 μ_b/Co in xtal 1974C and 1.9 μ_b/Co in xtal 2043an800C. Table 4.3 shows the expected saturated moment, M_{sat} for the various spin combinations, again assuming $g = 2$. As with the susceptibility measurement, we determine separately the moment on the Co^{3+} or Co^{2+} site with this bulk measurement; the average Co moment evaluated at 5 Tesla in our samples falls between 3/2 and 5/2 μ_b/Co. However, taken together, the susceptibility and field dependence measurements are most consistent with either the S = 1 and S = 3/2 configuration or the S = 2 and S = 1/2 configuration.

The inset to 4-9 shows M(H) at 30 K and 10 K. Except for the hysteresis in the 10 K scan, the two field sweeps appear identical. The absence of temperature dependence is the signature of an ordered phase. If the spins were uncorrelated, and Curie-like, the slope of

the 10 K scan would be 3 times larger than the 30 K scan. In addition, the Zeeman energy of a moment of 2 μ_b in a 1 T field is 120 μeV, while k_bT at 30 K is $\sim$ 2.6 meV. Therefore, for Curie-like spins, we would not expect to see saturation of the moment below 20 Tesla. We observe saturation near 5 Tesla.

4.2.4 Field dependence: neutron scattering measurements

Field-dependent neutron scattering measurements were performed on the $\delta \simeq 0.25$ samples in order to understand the ferromagnetic order, particularly at low field. All of the neutron scattering measurements were performed in the (0KL) plane, so that the magnetic field could be applied along the a-axis.

FM Bragg reflections occur at the same positions in reciprocal space as the structural peaks. For unpolarized spins, the total intensity at a structural reflection is the sum of the magnetic and nuclear scattering cross-sections,

$$\left(\frac{d\sigma}{d\Omega}\right)_{TOT} = \left(\frac{d\sigma}{d\Omega}\right)_{MAG} + \left(\frac{d\sigma}{d\Omega}\right)_{NUC}$$

The ratio of the intensities is therefore,

$$\frac{I_{MAG}}{I_{NUC}} = \frac{(\frac{1}{2}g)^2(\gamma r_0)^2[\sum_d e^{i\mathbf{Q}\cdot\mathbf{d}} f_{mag,d}(Q)\langle \mathbf{S_d}\rangle(1-\hat{\mathbf{S}}\cdot\hat{\mathbf{Q}})]^2}{[\sum_p e^{i\mathbf{Q}\cdot\mathbf{p}} f_{nuc,p}(Q)]^2} \tag{4.9}$$

In the numerator of Eqn. 4.9, the sum is over the positions of all of the magnetic ions in the structural unit cell, while in the denominator, the sum is over all of the atomic positions in the unit cell. The experimentally determined nuclear form factors for the dominant reflections are given in the Appendix.

Since magnetic scattering is relatively weak compared to nuclear scattering, it is easiest to look for FM scattering at 'weak' nuclear peaks. The (0, 0, 4) reflection is ideal as it has a relatively small structure factor (of order 10^{-2} times the (0, 2, 0) reflection) and occurs at a low enough $|\mathbf{Q}|$ that the form factor for magnetic scattering remains close to one. In addition, the susceptibility in Figure 4-8 suggests that the spins lie in the ab plane; therefore, the scattering vector at the (0, 0, 4) reflection is perpendicular to $\mathbf{S}$ and we can take the geometric factor in Equation 4.9 to equal one.

Figure 4-10 shows the change in intensity of the (0, 0, 4) Bragg peak upon application

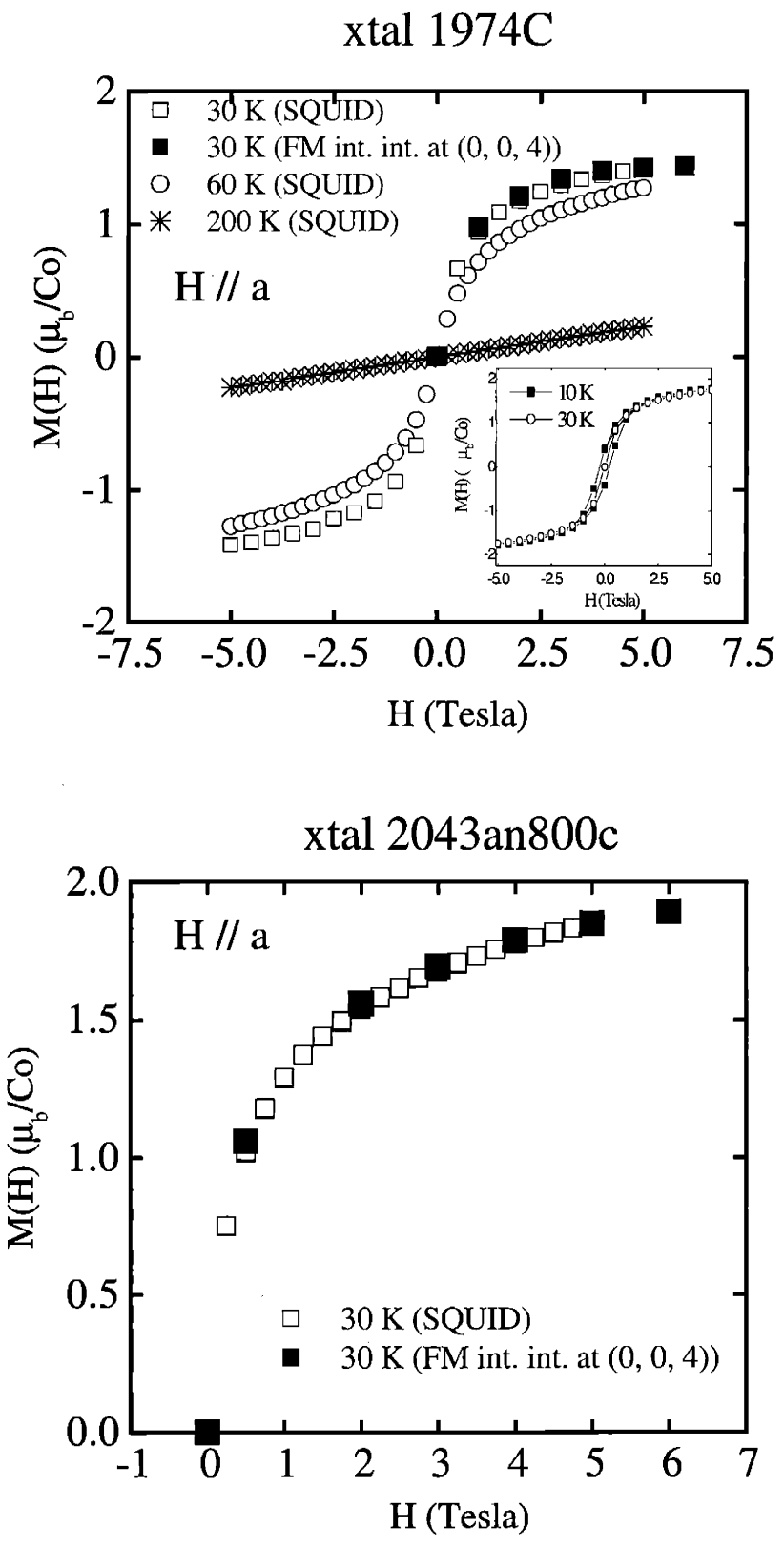

Figure 4-9: The field dependence of the uniform moment measured in the SQUID with H along **a** in xtals 1974C (top) and 2043an800c (bottom). Also shown is the field dependence of the square root of the intensity of the ferromagnetic scattering at (0, 0, 4) measured with neutrons (closed squares), normalized to the SQUID data at 5 T. The inset to the top panel shows field sweeps at 10 K and 30 K, showing an absence of temperature dependence.

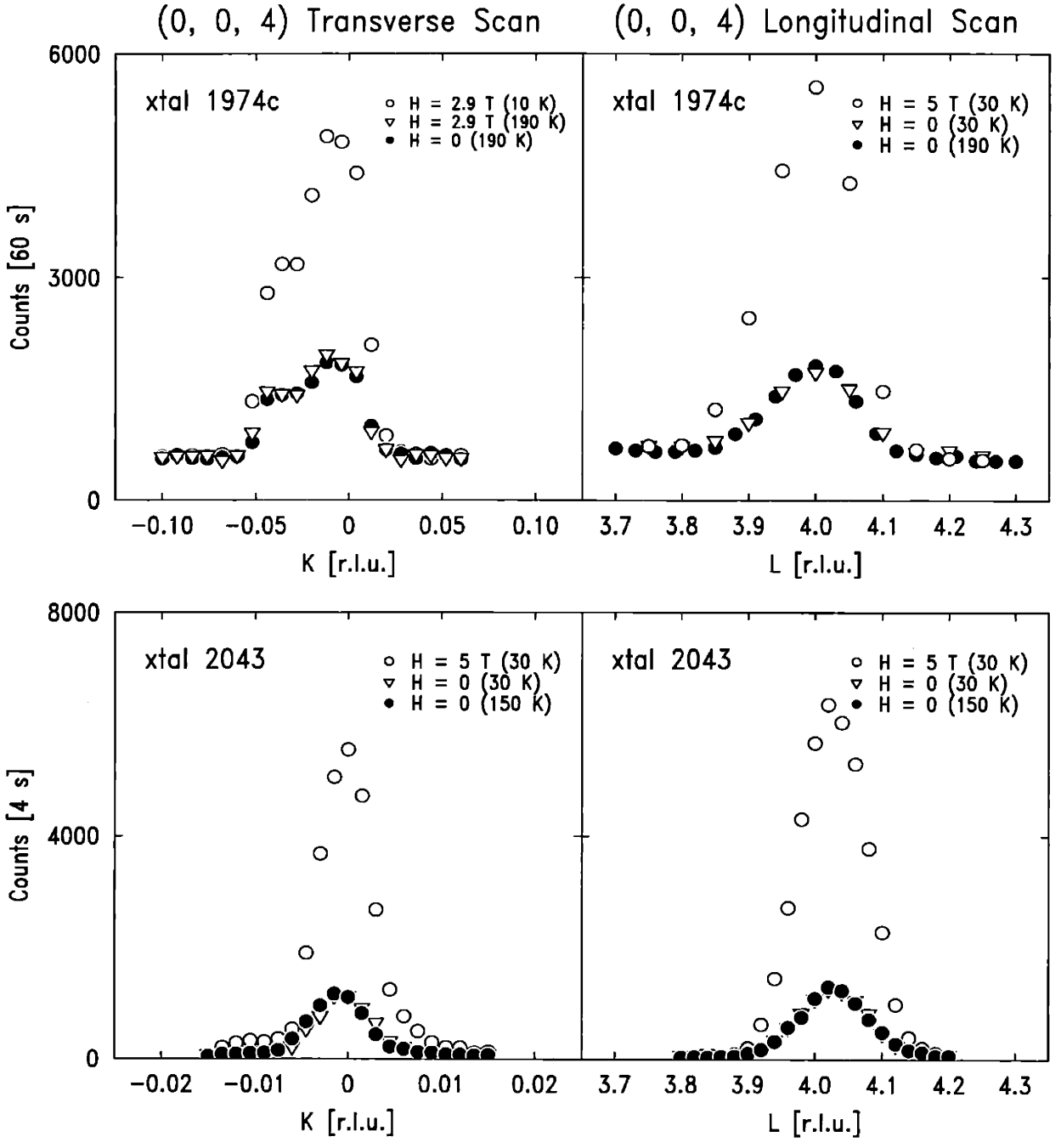

Figure 4-10: Enhancement of the scattering at the (0, 0, 4) reflection in xtals 1974C (top) and 2043an800C (bottom). Transverse and longitudinal scans in both samples show that there is no additional intensity at the (0, 0, 4) peak at H = 0, even at 30 K. The mosaic spread in xtal 1974C is more than five times that of xtal 2043an800C, which explains why longer counting times are required for xtal 1974C.

of a field at 30 K in xtals 1974C and 2043an800C. Note that the intensity of the 30 K, H = 0 peak has the same intensity as the peak at 190 K and H = 0. That is, in zero field, there is no spontaneous FM moment below the Curie-Weiss temperature $T_c \sim 100$ K.

To determine the field-dependent ferromagnetic contribution to the scattering, we subtract scans taken at zero-field and at temperatures above T_c. We can estimate the average uniform moment at 5 Tesla on a Co site using Equation 4.9 and letting $\langle S_d \rangle = \langle S_{FM} \rangle$. For crystal 1974C, we obtain $\langle S_{FM} \rangle = 1.84$ using the (0, 0, 4) nuclear peak for normalization. As a check, we compare this result with the moment calculated using a stronger nuclear reflection for normalization. Using the (0, 2, 0) peak for normalization, we find $\langle S_{FM} \rangle = 2.03$.[5] Similarly, for xtal 2043an800c, we find a ferromagnetic moment per Co of 2.2 ± 0.7 upon normalization to the nuclear (0, 0, 4) intensity. The moments measured at 5 T with neutrons agree well with the moment measured in the SQUID.

The field-dependent measurements of the FM intensity are in excellent agreement with the SQUID data. For both crystals 1974C (Figure 4-9(a)) and 2043an800C (Figure 4-9(b)), the FM contribution to the (0, 0, 4) peak at 30 K is plotted as a function of field. The neutron data are normalized to the SQUID data at 5 Tesla to emphasize the similar field dependence.

The temperature dependence of the high-field ferromagnetic moment is measured in both the SQUID and with neutrons. The data are plotted in Figure 4-11. In both measurements, the moment falls to zero around a temperature close to the T_c found in the Curie-Weiss fits of the susceptibility. Indeed, the inflection point of the moment as a function of temperature occurs between 95 and 100 K for both samples.

The data in Figure 4-9 show that both the moment measured in the SQUID and the moment measured by neutrons are zero in zero field. This is an important result: while the SQUID measures the *total* moment of the crystal, the intensity of magnetic Bragg peaks depends on the correlation of atomic magnetic moments on microscopic length scales. The formation of domains, which can affect the bulk measurement, does not affect the neutron scattering measurement provided the domains are sufficiently large ($L_{domain} \sim 100$ Å). This is because for an unpolarized neutron beam, the total scattering cross-section is symmetric with the sign of the FM moment. The result that the FM Bragg peak vanishes at zero field indicates that the ground state in zero field does not have a uniform moment. The loss of

[5] In this sample, we compared *peak* intensities and not *integrated* intensities.

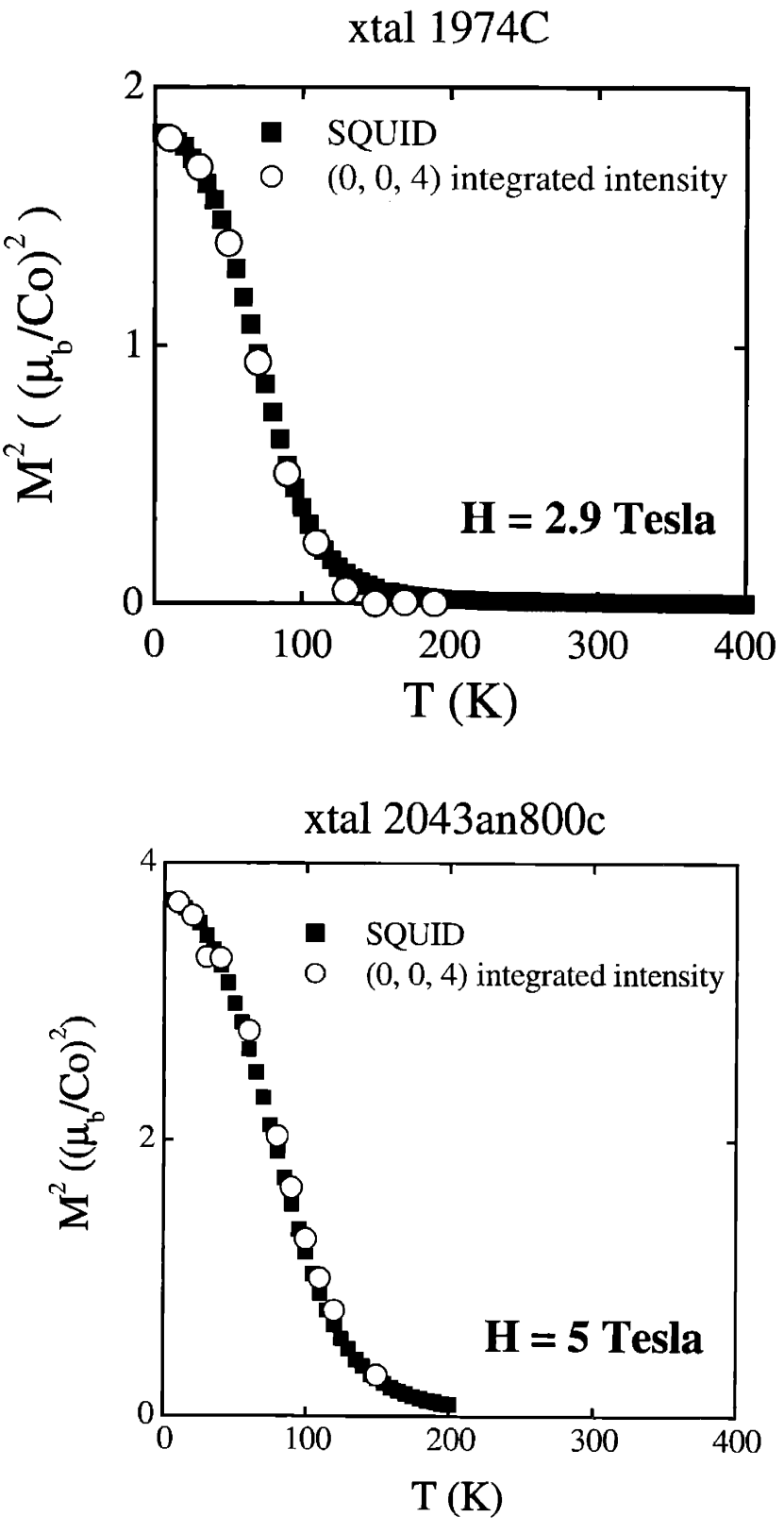

Figure 4-11: Temperature dependence of the square of the uniform moment measured in the SQUID (dark squares) and the magnetic contribution to the intensity at the (0, 0, 4) Bragg peak (open circles). The top panel shows xtal 1974C, in which the measurement is made at 2.9 Tesla. The bottom panel shows xtal 2043an800C, in which the measurement is made at 5 Tesla.

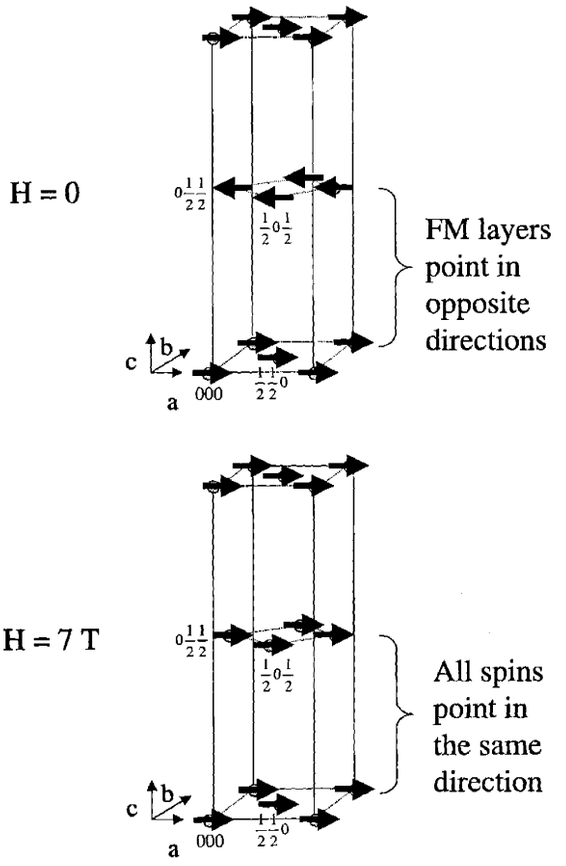

Figure 4-12: Model for the spin structure at zero-field (top figure) and at 7 Tesla (bottom figure). At zero-field, the in-plane spins are ferromagnetically aligned, while adjacent layers are anti-parallel. The overall order is antiferromagnetic at zero-field because the net moment vanishes. Application of a field along the a-axis results in a ferromagnetic alignment of all of the spins.

ferromagnetic scattering at the structural positions in zero field must therefore result in an increase in scattering elsewhere in reciprocal space.

4.2.5 Ferromagnetic order at zero-field

We are guided in our search for zero-field reflections by the susceptibility, which suggests that the spins enter an AF ground state below T_{peak}. Such an AF state does not have anti-parallel spins in the plane. Rather, we propose that at zero-field the spins are parallel in the plane but adjacent planes are anti-parallel. Such an arrangement is shown schematically in Figure 4-12.

An AF ground state in which the in-plane spins are parallel and adjacent layers are anti-parallel is characterized by magnetic reflections at the positions (0, 0, L = *odd*). Figure 4-13 shows an L scan through (0, 0, L = *odd*) at 30 K in zero field. The data are obtained by subtracting the same scan taken at 80 K. (The subtraction is necessary because structural

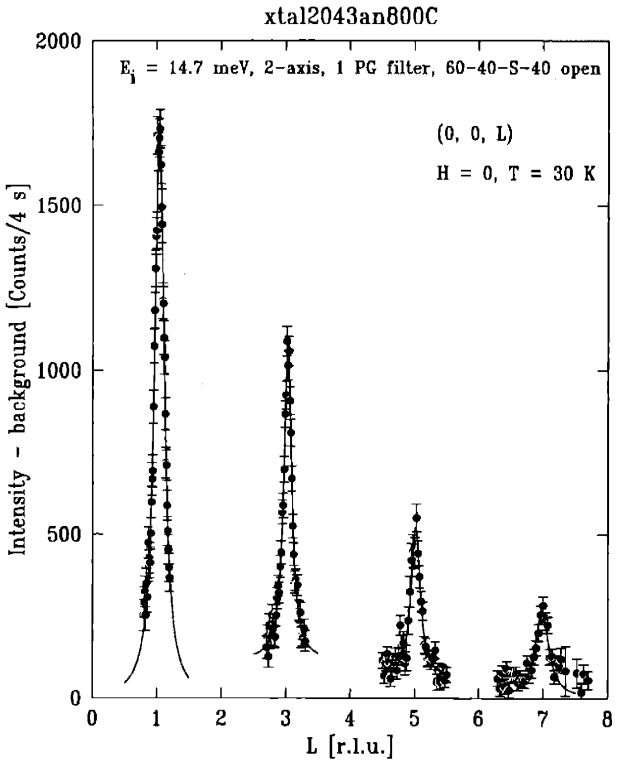

Figure 4-13: Scan through (0, 0, L) at 30 K in zero-field. The data are obtained by subtracting the same scan at 80 K. The solid curves are fits using a Lorentzian line shape. The fits have a non-zero background (which is most pronounced in the (0, 0, 3) scan) indicating that the background is also temperature dependent.

scattering is weakly allowed at these positions.) The peaks in Figure 4-13 show a fall off with increasing Q which suggests that these are indeed magnetic peaks. The peaks are fit with a Lorentzian line-shape. The peaks are slightly broader along L than the resolution width of the spectrometer, indicating that the magnetic layers are only correlated over short length scales perpendicular to the Co-O layers.

Figure 4-14 shows the temperature dependencies of the fitted amplitude of the (0, 0, 1) peak measured in zero-field and the square of the uniform moment measured in a 100 G field. Both curves are normalized to the same value at 25 K. The comparison of the neutron and susceptibility data indicates that the suppression in χ_a below the peak results from the 3D ordering of the ferromagnetic layers. The difference between the neutron data and the SQUID data presumably results because the susceptibility is measured in a 100 G field while the (0, 0, 1) reflection is measured at zero-field. The temperature dependence of the (0, 0, 4) peak and the corresponding SQUID measurement of the uniform moment are shown in the top panel of Figure 4-14

Field-dependence measurements show that the (0, 0, L = *odd*) peaks disappear at very

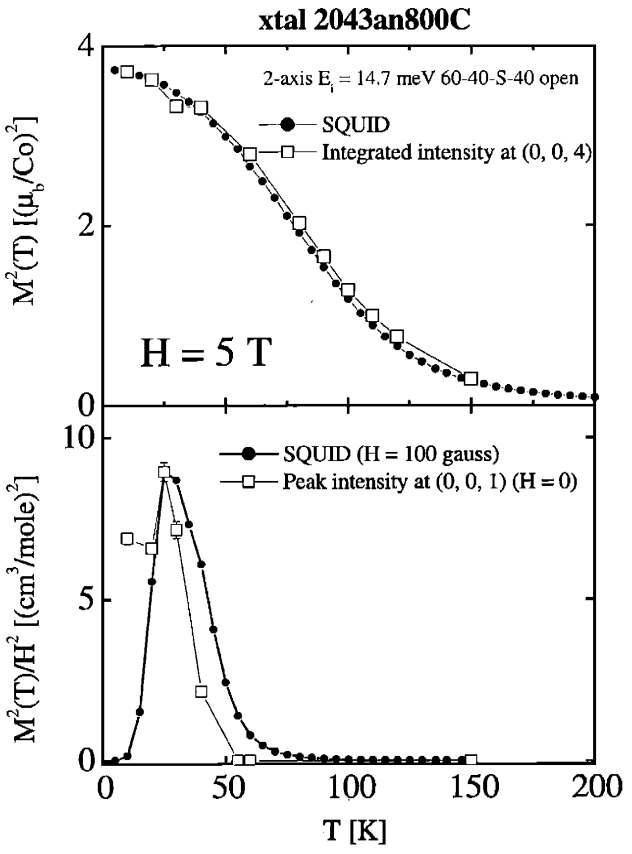

Figure 4-14: Top panel: Temperature dependence of the (0, 0, 4) FM peak and the moment measured in the SQUID after field-cooling in 5 Tesla. Bottom panel: Temperature dependence of the (0, 0, 1) magnetic peak in zero-field and the square of M/H measured in the SQUID at 100 Gauss. The data are normalized at the peak temperature of 25 K.

small fields. Scans through the (0, 0, 3) and (0, 0, 4) magnetic peaks at various fields are shown in Figure 4-15. We compare the (0, 0, 3) and (0, 0, 4) peaks because they have similar form factors. At 0.5 Tesla, the (0, 0, 3) peak is zero while the ferromagnetic contribution to the (0, 0, 4) peak is not even half of its 6 Tesla value. Thus, there is not a one-to-one correlation between the decrease in intensity of the (0, 0, 3) peak and the increase in the (0, 0, 4) peak, even accounting for differences in the magnetic form factor. In addition, the background near the (0, 0, L=*odd*) peak decreases with field. This suggests that there is diffuse scattering at zero-field which is contributing to the total scattering at higher fields.

Magnetization measurements in the SQUID suggest a change in the field dependence at very low fields. Figure 4-16 shows M(H) measured below 1 kG. There is a subtle change in curvature near 60 Gauss, which is apparent in the derivative of M(H) shown in the inset.

One possible explanation for the antiferromagnetic coupling between layers is a dipolar interaction. Consider the interaction between a spin and its four nearest-neighbor spins in

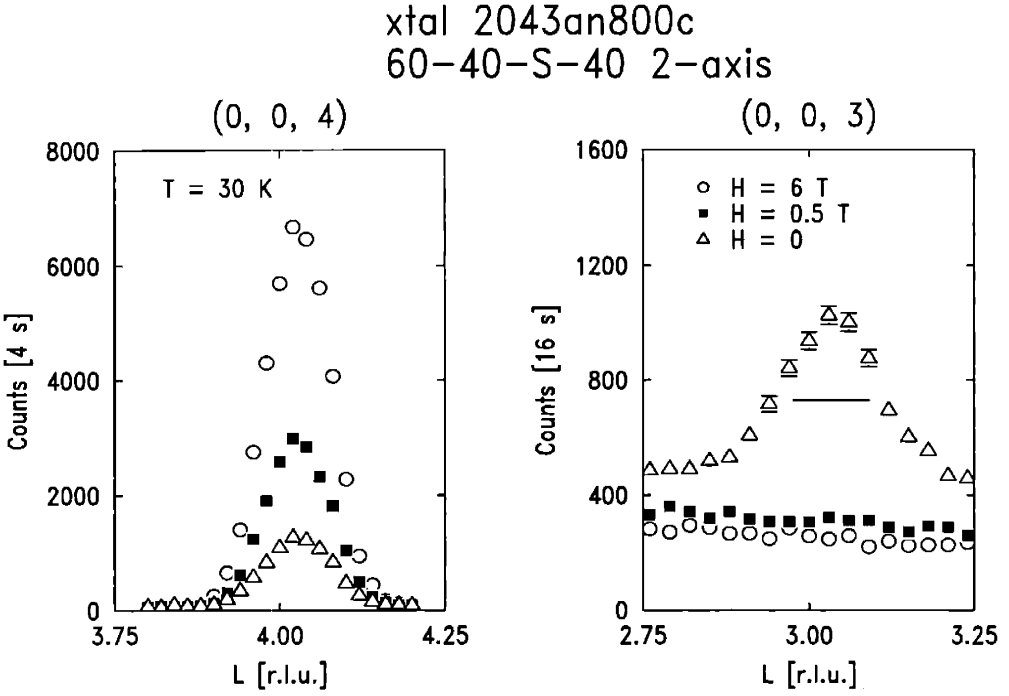

Figure 4-15: Field dependence of the (0, 0, 4) and (0, 0, 3) peaks at 30 K. The FM (0, 0, 4) peak shows a continuous increase in intensity with field, while the (0, 0, 3) peak shows a sudden decrease between 0 and 0.5 Tesla. The background in the vicinity of the (0, 0, 3) peak also continues to decrease with field.

adjacent layers shown in Figure 4-17. The dipolar interaction between spins in neighboring layers will result in spins in adjacent layers pointing in opposite directions. A smaller "antiferromagnetic" dipolar interaction also exists between next-nearest neighbor spins in adjacent layers.

The dipole field from a magnetic moment $\mathbf{m}$ is given by

$$B_{dipole} = \frac{\mu_0}{4\pi r^3}[3[\mathbf{m}\cdot\hat{\mathbf{r}}]\hat{\mathbf{r}} - \mathbf{m}] \tag{4.10}$$

Here, $\mathbf{m} = g\mu_b\mathbf{S}$ is the effective magnetic moment resulting from the spin on a Co ion and $\mu_0 = 4\pi \times 10^{-7}\ \frac{N}{A^2}$.[6] Plugging in appropriate values for the lattice parameters, we find $r = 12.1\ \mathring{A}$ and $\mathbf{m} = 2.7$ x 10^{-23}J/Tesla (for $g\mathbf{S} = 1.5$). The total dipole field at a spin site resulting from the dipole field of the four spins in layers above and below (eight total spins) is therefore about 63 Gauss. This is in very good agreement with the measurements of M(H) shown in 4-16, which indicates a change in curvature near 60 Gauss.

[6]Equation 4.10 is written in SI units, so that B is in units of Tesla and $\mathbf{m}$ is in units of A m^2. To calculate B_{dipole} in **cgs** units of **gauss**, $\frac{\mu_0}{4\pi}$ should be replaced by $\frac{1}{c}$ and m must have units of **emu**.

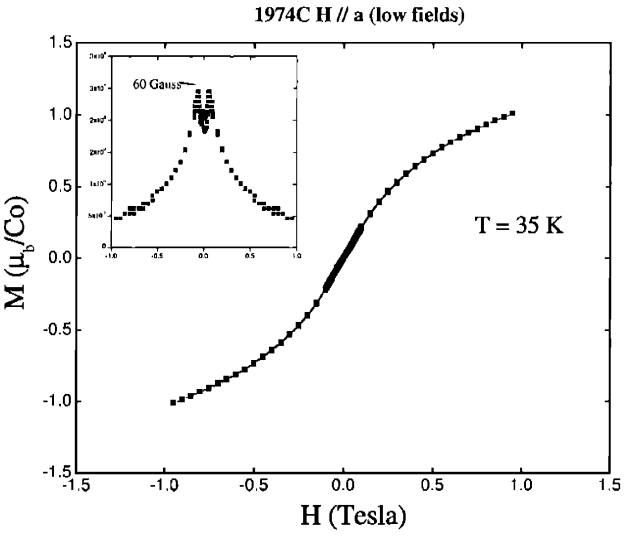

Figure 4-16: M(H) at 35 K, showing finer steps near zero field in xtal 1974C. At high fields, the M(H) curve is sigmoidal, while at low fields, M(H) is nearly linear in H. The inset shows dM/dH. A change in curvature occurs near 60 Gauss.

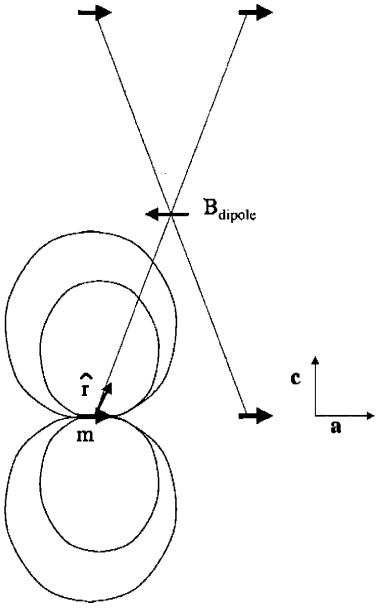

Figure 4-17: Schematic showing the dipole field at a spin resulting from nearest neighbor spins in adjacent layers. There is also a contribution from the next-nearest neighbors in adjacent planes, which is not shown.

There is a problem, however, with the interpretation that at zero-field, the spins in adjacent planes are anti-parallel and at high-fields, they are parallel. If the field forces alternating layers to flip, then the total intensity of the scattering at (0, 0, L = *even*) at high-field and the total intensity of the scattering at (0, 0, L = *odd*) in zero-field should be the same. Comparing Figures 4-15 (a) and (b), the scattering at (0, 0, 4) in 6 T is nearly 20 times larger than the scattering at (0, 0, 3) in zero-field. Even if we account for the broadening along L in the (0, 0, 3) scan, which results in a peak width less than a factor of two times the width of the (0, 0, 4) peak, we can not fully recover the intensity of the (0, 0,4) peak at high field. In addition, the zero-field magnetic peaks fall off rapidly with field, while the high-field magnetic peaks show a gradual increase.

The fact that the (0, 0, L = *odd*) peaks are broad at zero-field suggests that the coupling between magnetic layers is sufficiently weak that only short range correlations exist. Disorder, resulting from the long-wavelength modulation along **a** and hence differences in the effective interaction between nearest-neighbor spins in adjacent layers, may result in large deviations from the dipolar interaction calculated above. Furthermore, the observation that the diffuse scattering in the vicinity of the (0, 0, L = *odd*) peak decreases with increasing field suggests that spins in adjacent layers are only weakly correlated; the presence of a small Bragg peak at zero-field suggests that the dominant interaction, though weak, is antiferromagnetic between nearest neighbors. Since the magnetic field polarizes spins in adjacent layers in the same direction, the field induces an effective correlation between spins and the intensity under the ferromagnetic Bragg peak at (0, 0, 4) grows immediately with field. Again, disorder may explain why the transition to the fully polarized state occurs over a wide range of fields.

4.2.6 Charge ordering

Samples with $\delta \simeq 0.25$ samples are insulating. Since there should be an equal concentration of Co^{3+} and Co^{2+} in these samples, it is reasonable to expect the stabilization of a charge ordered phase. Charge order peaks should be detectable by x-rays and neutrons as structural super-lattice peaks. For example, one might expect a periodic distortion of the cobalt-oxygen bond distances: the oxygen ions will lower their energy by moving in toward the Co^{3+} ions and away from the Co^{2+} ions.

We have looked for charge ordering peaks with neutrons at high-symmetry positions

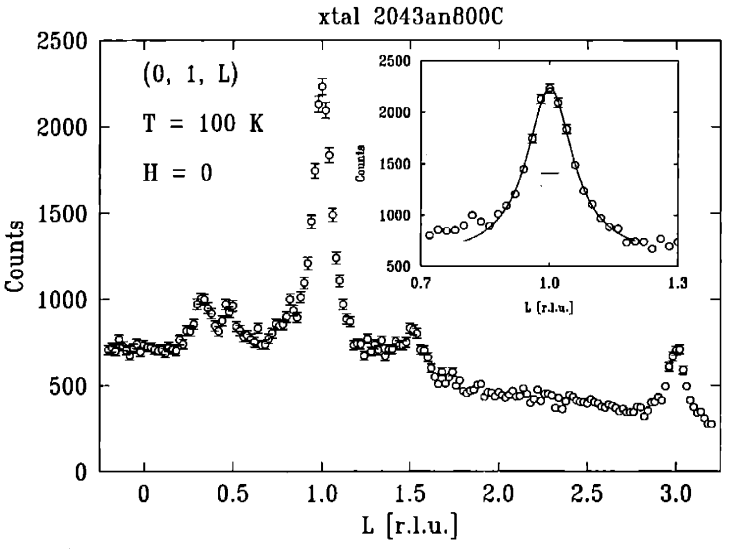

Figure 4-18: Scan along (0, 1, L) showing peaks which are consistent with charge-ordering. The inset shows the (0, 1, 1) peak and the spectrometer resolution.

in xtal 2043an800c. Figure 4-18 shows a scan along (0, 1, L) at 100 K and in zero-field. Broad peaks are visible at the L = 1 and L = 3 positions and no peaks are observed at the (0, 1, L=*even*) positions. The peaks extend to higher Q and the intensity of the peaks shows a similar structure factor dependence on L to the fundamental nuclear Bragg peaks. Therefore, these peaks are not magnetic.

The inset to Figure 4-18 shows the (0, 1, 1) peak and the spectrometer resolution width, which is much narrower than the observed peak width. The data are fit with a Lorentzian line-shape (dark curve) with $\Gamma \sim 0.066$ r.l.u. The peak width corresponds to a correlation length of approximately two c-axis lattice constants, or four Co-O sheets. On the other hand, the peaks are resolution limited in the plane. The charge-order peaks exhibit little temperature dependence up to 300 K, indicating that the melting temperature for the charge order is well above room temperature.

The positions of the peaks are consistent with a model in which Co^{2+} and Co^{3+} are in a checkerboard arrangement in the plane. The L-dependence of the charge-order peaks suggests a particular stacking arrangement along the c-axis. In Figure 4-19, two possible stacking arrangements of the checkerboard are indicated. In (a), all Co^{2+} sites are in the same bc plane, while in (b), all Co^{2+} sites are in the same ac plane. The configuration in (a) results in CO peaks at the (0, 1, L=*odd*) positions, as observed in our measurements. The fact that we observe only a particular stacking arrangement along the c-axis may be

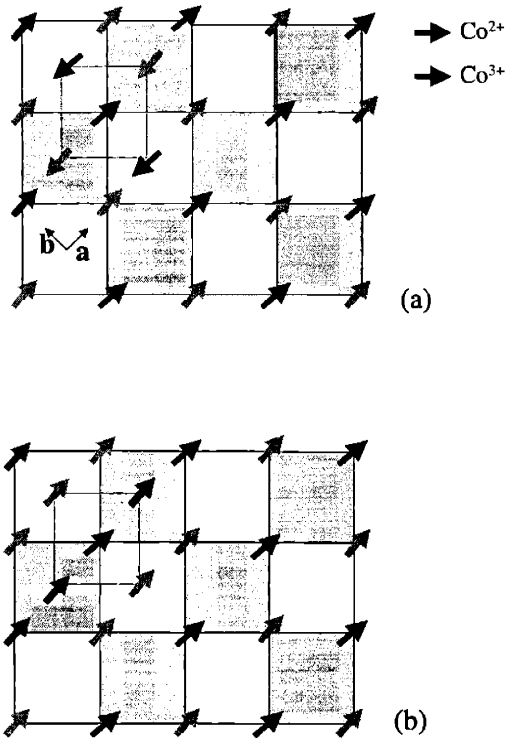

Figure 4-19: Arrangement of Co^{2+} and Co^{3+} spins in a single layer. There are two possible stacking arrangements for the charge-ordered checkerboard. This is indicated by the dotted square, which shows the orientation of a plaquette of spins in the neighboring layer. The configurations correspond to (a) all like charges in the same *bc* plane or (b) all like charges in the same *ac* plane.

related to the orthorhombic distortion.

A checkerboard arrangement of the Co^{2+} and Co^{3+}charges in the plane is the most energetically favorable configuration because it minimizes the Coulomb interaction. This configuration is observed, for example, in $La_{1.5}Sr_{0.5}CoO_4$, in which there are an equal number of Co^{2+} and Co^{3+} sites.[11] The charge order peaks are also short-ranged in $La_{1.5}Sr_{0.5}CoO_4$, and persist up to a temperature 700 K.

4.2.7 Magnetic super-lattice peaks

A direct consequence of the charge ordering is the existence of two distinct *magnetic* sublattices. Co^{2+} and Co^{3+} should have different sized spins and this will be reflected in magnetic super-lattice peaks. We have looked for magnetic super-lattice peaks in xtal 2043an800C, the same sample in which we saw the charge ordered peaks described above.

For a checkerboard of Co^{2+} and Co^{3+} with spins S_1 and S_2, respectively, super-lattice peaks should occur at the positions (0, 1, L) and (1, 0, L), with the particular integer

values of L determined by the stacking of the magnetic lattice along **c**. It should be noted that, in terms of the in-plane scattering, the magnetic super-lattice is analogous to an antiferromagnet with $S_{AF} = 1/2(S_1 + S_2)$. In the (0KL) scattering geometry, we looked at the reflections along (0, 1, L) as a function of temperature and field. In Figure 4-20, L-scans through (0, 1, 0) and (0, 1, 1) are shown as a function of field and temperature. There is already a large peak at (0, 1, 1), which we argued above, may arise from charge ordering. Therefore, the inset to the scan through (0, 1, 1) shows the difference between a scan through (0, 1, 1) at 0 field and at 6 Tesla. We see that the (0, 1, L = *even*) peak is present at low temperatures and zero-field and the additional scattering at the (0, 1, L=*odd*) peak is present at low temperature and high-field. Thus, the (0, 1, 0) peak appears to follow the field and temperature dependence of the (0, 0, L = *odd*), zero-field FM peaks. On the other hand, the (0, 1, 1) peak follows the temperature and field dependence of the high-field, FM (0, 0, 4) peak. Figure 4-21 shows the (0, 0, 1), (0, 1, 0), (0, 0, 4) and (0, 1, 1) peaks as a function of temperature. The data show that the (0, 1, 0) intensity has the same temperature dependence as the (0, 0, 1) peak, while the (0, 1, 1) peak follows that of the ferromagnetic contribution to the (0, 0, 4) peak.

It is natural to interpret the peaks in Figure 4-20 as magnetic super-lattice peaks of the ferromagnet. If we conclude that the temperature independent peaks at (0, 1, L = *odd*) are charge-order peaks, then we have a definite prediction for the L-dependence of the magnetic super-lattice peaks. The magnetic super-lattice peaks are consistent with the proposed charge arrangement. Furthermore, the change in the L-dependence with field is consistent with the change in the L-dependence of the fundamental ferromagnetic reflections.

However, there are several observations which suggest these peaks are not magnetic super-lattice peaks. The first is that the intensities of the peaks are actually quite large. We can, for example, compare the intensity of the (0, 1, 0) peak at zero-field to the (0, 0, 3) peak at zero-field. The (0, 1, 0) peak is approximately 9 counts/s while the (0, 0, 3) peak is about 35 C/s. Thus, the intensity at the (0, 1, 0) peak close to 25% of the intensity at the (0, 0, 3) peak. For S = 3/2 and S = 1, we expect the relative intensity to be closer to 0.04; thus the observed scattering seems large. Furthermore, the magnetic (0, 1, 0) and (0, 1, 1) peaks are resolution limited, while the zero-field ferromagnetic peaks are not resolution limited. We would expect the magnetic super-lattice peak at zero-field to have the same correlation length along **c** that is observed in the zero-field ferromagnetic peak. Finally, we

can not rule out the possibility that these peaks result from a residue of $\delta \sim 0.5$ phase. More work is required to unambiguously determine that these peaks are magnetic super-lattice peaks.

4.2.8 Summary

There are a number of results from the neutron and SQUID measurements, which we summarize here.

1. The dominant interaction is ferromagnetic. The high temperature susceptibility follows a Curie-Weiss temperature dependence, with a ferromagnetic $T_c \sim 100$ K. In addition, the M(H) curves exhibit a large uniform moment (approximately 1.5-1.9 μ_b/Co at 5 Tesla).

2. The neutron scattering measurements are consistent with long-range ordered ferromagnetism at fields > 0.5 T and below $T_c \simeq 100$ K.

3. At zero-field, the uniform moment vanishes. Magnetic peaks are observed which indicate antiferromagnetic coupling between adjacent ferromagnetic layers. The zero-field magnetic phase is only short-range ordered perpendicular to the layers. In addition, diffuse scattering indicates that the zero-field state may be highly disordered. This may explain why the high-field ferromagnetic peak is so much larger than the zero-field antiferromagnetic peak.

4. We observe peaks which are consistent with charge ordering resulting from a checker-board of Co^{2+} and Co^{3+} spins. The charge order peaks correspond to a particular stacking arrangement of the checker-board along the c-axis. The charge ordering is correlated over ~ 4 Co-O layers.

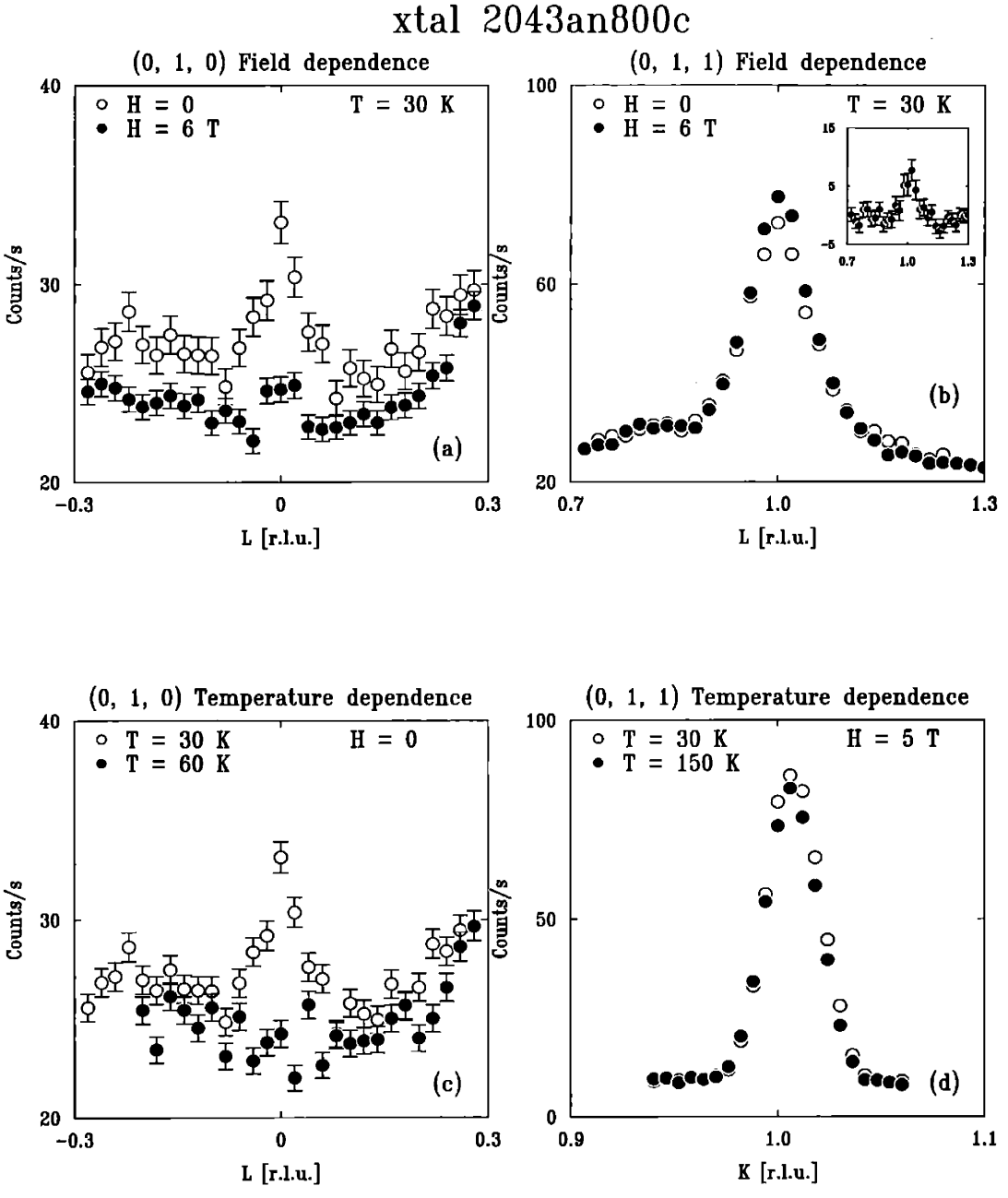

Figure 4-20: Scans through the reflections where magnetic super-lattice peaks are expected to occur. The two top panels show the (0, 1, 0) and (0, 1, 1) peaks as a function of field at 30 K. The (0, 1, 0) peak disappears in a field while the field induces additional scattering at the (0, 1, 1) peak (see inset). The bottom two panels show the (0, 1, 0) and (0, 1, 1) peaks as a function of temperature.

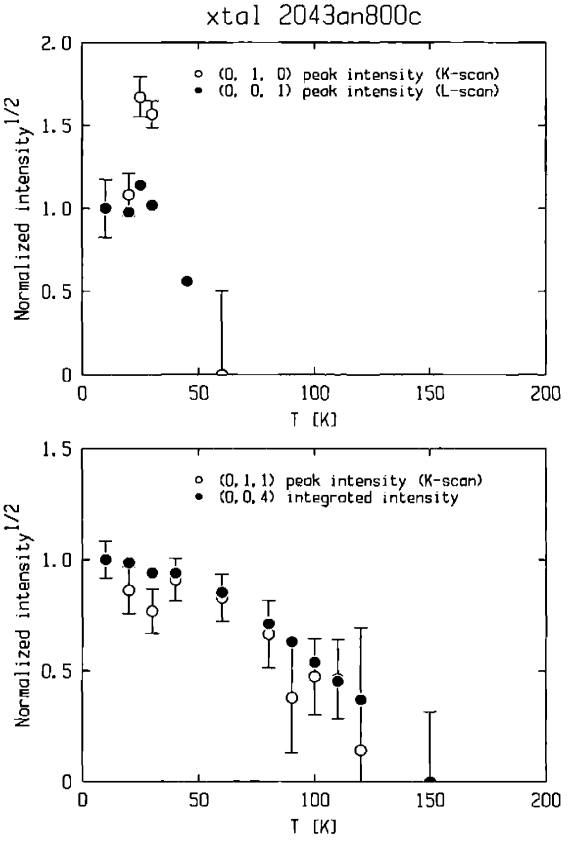

Figure 4-21: Temperature dependence of the (0, 1, 0) and (0, 0, 1) peaks in zero-field (top panel) and the (0, 1, 1) and (0, 0, 4) peaks in a 5 Tesla field (bottom panel).

4.3 Doping dependence

The compositions $Bi_2Sr_2CoO_{6.5}$ and $Bi_2Sr_2CoO_{6.25}$ appear to be two end points in the phase diagram of $Bi_2Sr_2CoO_{6+\delta}$. $Bi_2Sr_2CoO_{6+\delta}$ with $\delta \geq 0.4$ has mostly Co^{3+} spins and undergoes a transition to an antiferromagnetic alignment of the spins in the *ab* plane with $T_N > 200$ K. On the other hand, samples with $\delta \simeq 0.25$ have nearly equal numbers of Co^{3+} and Co^{2+} ions and the in-plane interaction is ferromagnetic with $T_c \sim 100$ K. It is important to understand how the removal of oxygen results in a transition from antiferromagnetic to ferromagnetic ordering. To study the evolution of the magnetism between the two end-point compositions $\delta = 0.25$ and $\delta = 0.5$, we have characterized samples which have been annealed to give a range of Néel temperatures from 295 to 0 K. Field dependent neutron scattering measurements on several of these samples indicate that antiferromagnetic and ferromagnetic domains, characteristic of the $\delta = 0.5$ and $\delta = 0.25$ crystals respectively, co-exist in samples with intermediate δ.

4.3.1 Susceptibility: overview of doping dependence

The magnetic susceptibility χ_a of several samples with different T_{peak} is shown in Figure 4-22. As we discuss below, T_{peak} can be considered a measure of T_N for samples with T_{peak} greater than 100 K. The susceptibility curves in Figure 4-22 show the dramatic evolution of the magnetism with removal of oxygen: coincident with the suppression of the Néel temperature with decreasing oxygen is an enormous growth in the ferromagnetic-like peak. The magnitude of the peak in the sample with $T_{peak} = 25$ K is nearly two-orders of magnitude larger than the $T_{peak} = 295$ K sample. Fits of the curves to a Curie-Weiss form, $\frac{C}{(T-T_c)} + \chi_0$, confirm that all of the samples have a ferromagnetic T_c (i.e. $T_c > 0$). From the Curie-Weiss fits, T_c is approximately equal to T_{peak} for $T_{peak} > 100$ K, but plateaus at around 100 K for $T_{peak} < 100$ K. It should be noted that the T_c of the pure ferromagnetic samples, with $\delta \simeq 0.25$, is also 100 K. Therefore, ferromagnetism with $T_c \sim 100$ K appears to be the limiting behavior of the reduced samples. Finally, concomitant with the decrease in T_c is an increase in the fitted Curie constant. This trend is clear in the plot of $\frac{1}{\chi(T)-\chi_0}$ in Figure 4-23. The lines through each curve emphasize the linear dependence of $\chi^{-1}(T)$ above T_{peak} as well as the x-intercept, which is equal to T_c.

For most of the samples shown in Figure 4-22, we measure T_N, the onset temperature

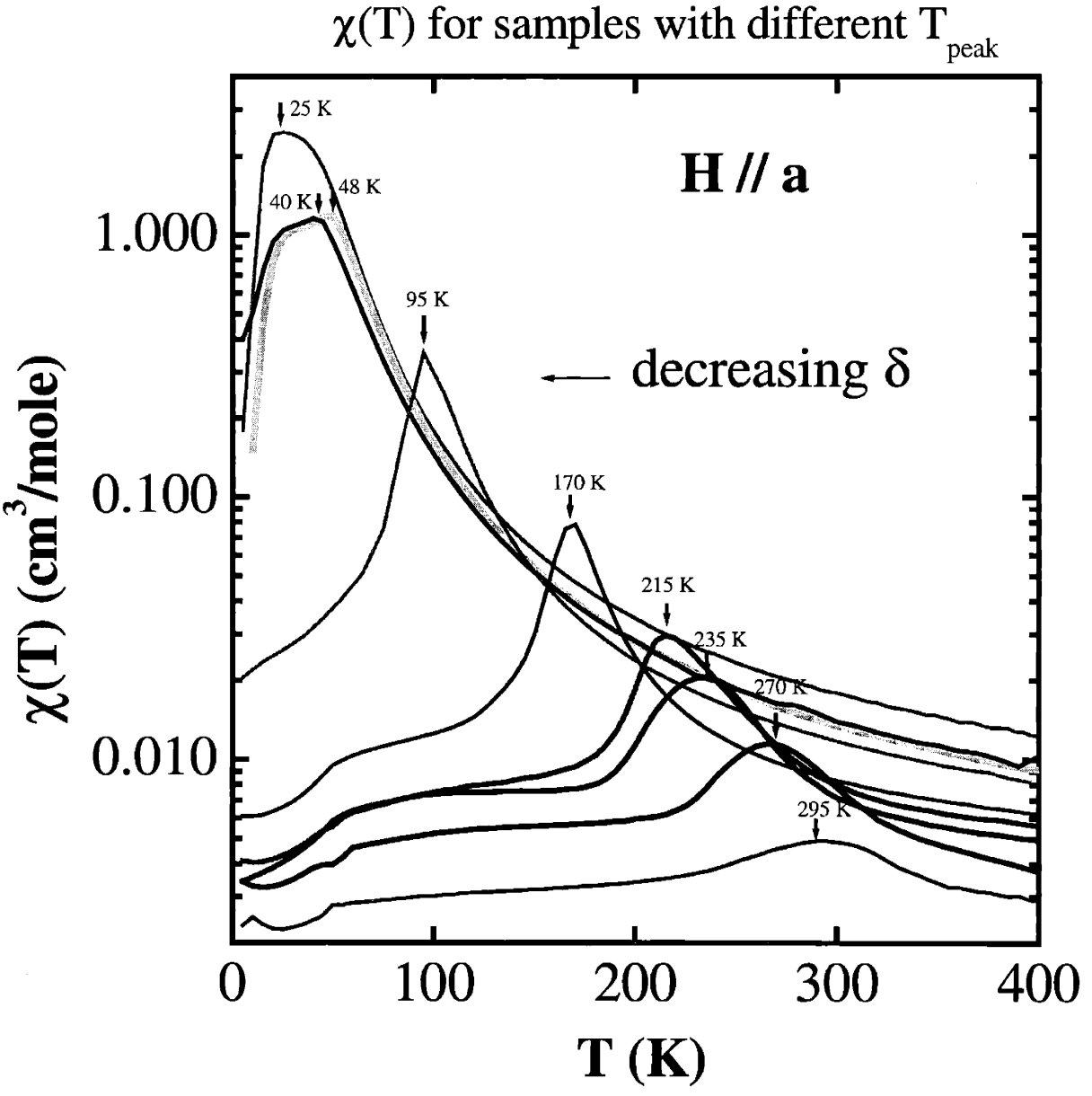

Figure 4-22: Semi-logarithmic plot of the temperature dependent susceptibility of samples annealed in vacuum or oxygen to yield different oxygen content, δ. The field is along **a**, the AF spin direction. The samples with T_{peak} = 270, 235 and 215 K were measured as-grown. The samples with T_{peak} = 170 and 95 K were annealed in < 10 mTorr vacuum at 600 and 750 C, respectively. The samples with T_{peak} = 47.5 and 40 K were annealed at 800 C in an evacuated quartz tube with Cu powder as a reducing agent. The T_{peak} = 25 K was annealed in vacuum at 800 C. The sample with T_{peak} = 295 K was first reduced using the quartz tube method and then annealed, at 900 C, in a flow of pure oxygen.

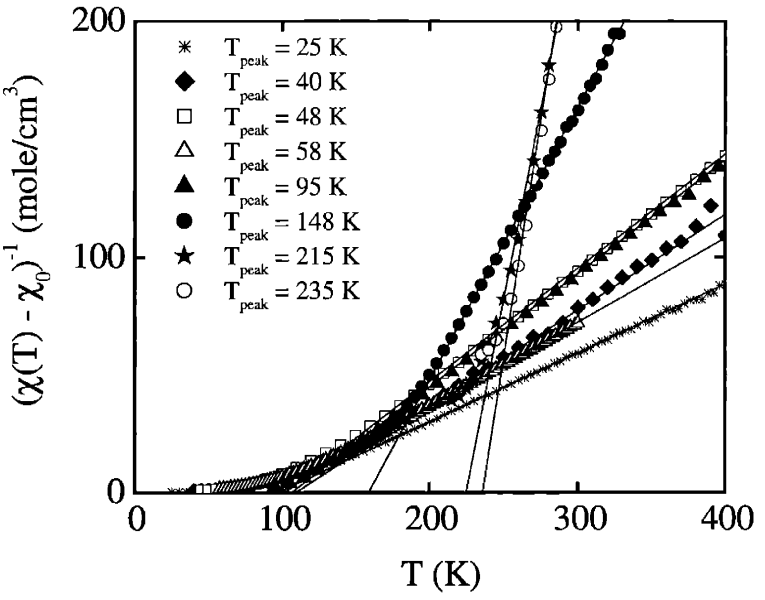

Figure 4-23: Temperature dependent inverse susceptibility for samples which have been annealed to obtain different T_{peak}. The temperature independent susceptibility, χ_0, has been subtracted. Note that the slope of the curves above T_{peak} is equal to 1/C, while the x-intercept is equal to T_c.

of the (in-plane) antiferromagnetic sub-lattice magnetization [7] and T_c, the Curie-Weiss temperature. We find that $T_N \sim T_{peak} \sim T_c$ for $T_{peak} \geq 125$ K. On the other hand, for samples with $T_{peak} < 125$ K, T_c levels off at ~ 100 K. This is true even in samples for which there is no observed antiferromagnetic transition. The enormous growth of the ferromagnetic-like peak with decreasing T_N suggests that the ferromagnetic interaction is favored by removal of oxygen from $Bi_2Sr_2CoO_{6+\delta}$ and competes with the antiferromagnetic order found in samples with $\delta \simeq 0.5$.

The AF spin ordering of samples with $\delta \sim 0.5$ and $T_N > 200$ K was discussed in Section 4.1. From Figure 4-22, it is clear that the ferromagnetic peak, though much reduced compared to the peak in samples with $\delta \sim 0.25$, is present for these high T_N samples as well. Therefore, we first focus on understanding the presence of ferromagnetism in a sample which has a nominally high δ ($\delta > 0.4$) and a well defined AF transition at $T_N > 200$ K, before discussing the full doping dependence of the magnetism for $0.25 < \delta < 0.5$.

[7] Since the transition to antiferromagnetic order is difficult to fit with a unique choice of parameters, T_N is defined as the temperature at which the intensity at the AF reflection is 10% of the intensity at base temperature

4.3.2 Field dependence in samples with $\delta > 0.4$

The field dependence of the moment at temperatures below T_N suggests ferromagnetism which is hidden at zero field. Figure 4-24(a) shows scans of the moment as a function of field in xtal 2043 ($T_N \sim T_{peak} = 215$ K). The scans are performed at temperatures 180 K and 50 K, with the field applied along **a**, the antiferromagnetic spin-direction. At low fields, the moment is linear in field and the slope is equal to the zero field susceptibility. Near 1.6 Tesla, there is a large jump in the moment which corresponds to $\sim 0.25\ \mu_b$ per Co for the field sweep at 180 K. We define the maximum in dM/dH as the "critical field", H_c, for the jump in the moment.

The comparison between M(H) at 180 K and 50 K in Figure 4-24(a) shows that the field dependence of the moment becomes increasingly hysteretic with decreasing temperature. Below 10 K there is no sign of a deviation from a constant susceptibility up to 5 T, suggesting that the hysteresis is larger than the range of the field used in the measurement. (The growing hysteresis with decreasing temperature is consistent with the observed difference between field cooled and zero-field cooled measurements of the susceptibility.) Therefore, in order to obtain the largest uniform moment, the sample should be cooled in a field.

Figure 4-24(b) shows the moment as a function of temperature while cooling in a 5 Tesla field. The moment versus temperature in the field-cooled measurement resembles that of a ferromagnet with $T_c = T_{peak}$. This is consistent with the Curie-Weiss fit of χ_a above the peak, which suggests ferromagnetism with $T_c \sim T_{peak}$. Yet, the uniform moment only appears above H_c; as we show below, neutrons reveal no ferromagnetic moment below H_c. The data in Figure 4-24(b) therefore describe the temperature dependence of a field-induced ferromagnetic moment. The fact that the onset of the ferromagnetic moment coincides with T_{peak} (and hence T_N) suggests that the field induced ferromagnetic behavior only occurs in the ordered phase of the AF.

The moment obtained at 5 Tesla after first cooling in zero-field is also shown in Figure 4-24(b). Comparing the zero-field cooled and field-cooled moment, we see that the discrepancy between the two grow dramatically with temperature. The large hysteresis of the moment in a field suggests that the field driven transition is first-order.

Finally, we note that when the field is applied along **b** or **c** the moment is linear with field up to 5 Tesla at all temperatures. Again, this is consistent with the susceptibility data,

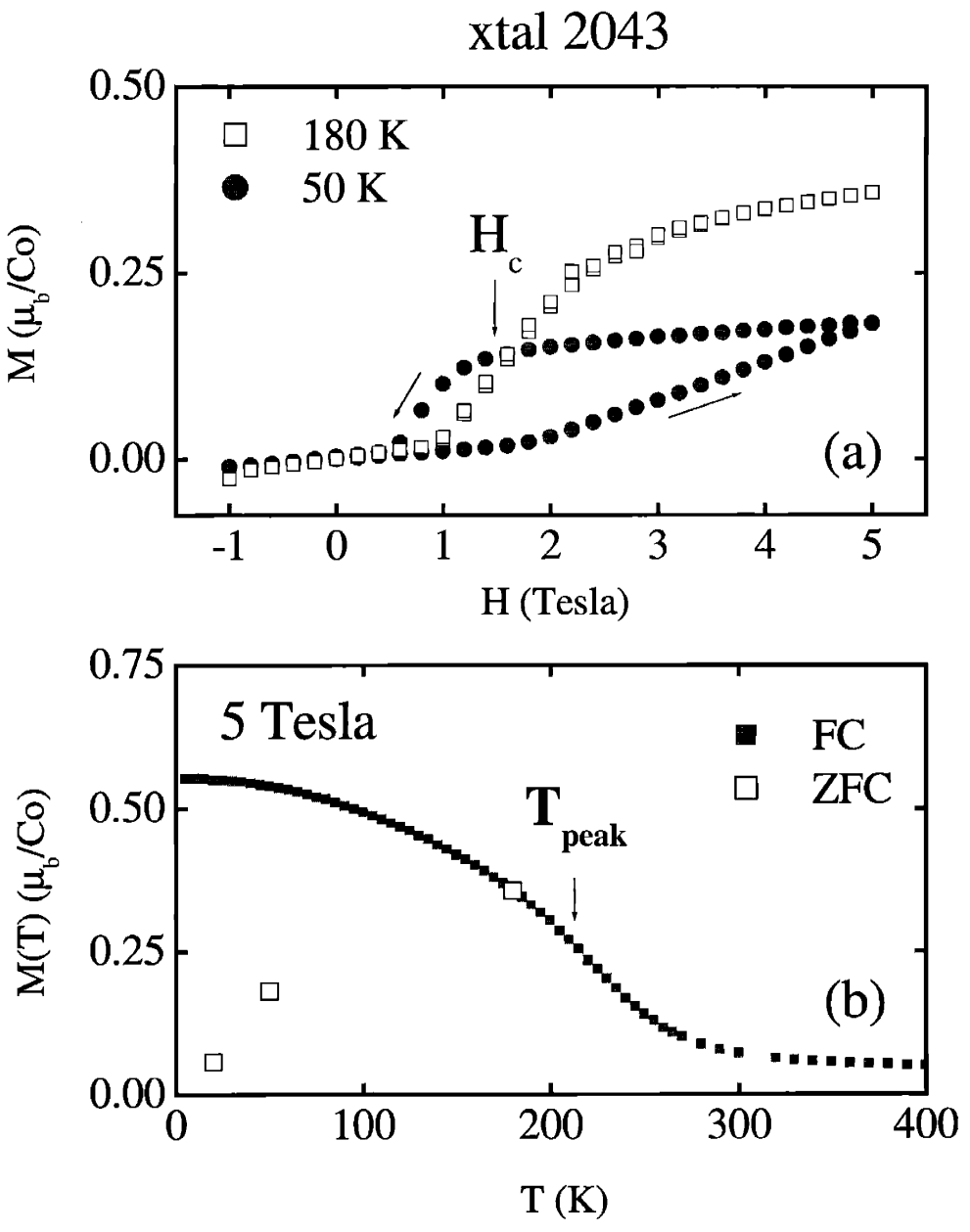

Figure 4-24: (a) Field dependence measured in xtal 2043 ($T_N \sim T_{peak} = 215$ K) for $T < T_N$ and H along **a**. The arrows indicate the direction of changing field. H_c is the critical field at 180 K, defined as the field where $\frac{dM}{dH}$ is a maximum. (b) Temperature dependence of the high field phase. The field-cooled (FC) measurement is made by first cooling in a 5 T field from above T_N and then measuring the moment while warming in 5 T. The open squares indicate the moment at 5 Tesla after cooling in zero field (ZFC). The inflection point of the FC M(T) curve occurs at T_{peak}.

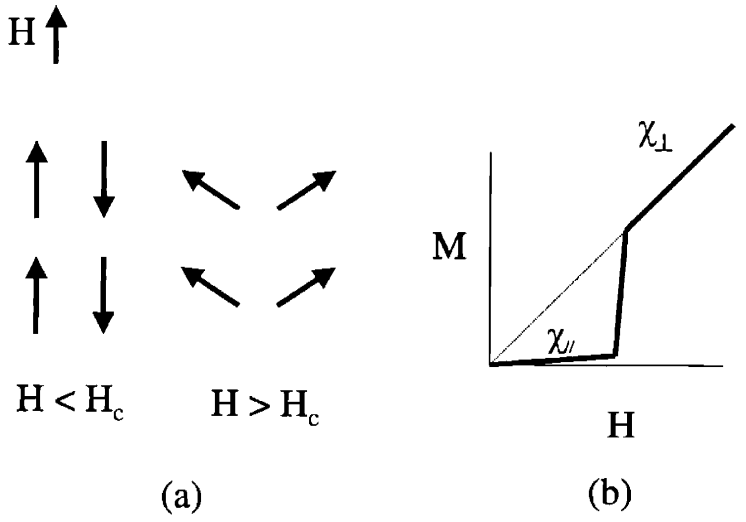

Figure 4-25: (a) Spin configuration below and above the critical field for the spin flop transition in a uni-axial AF. (b) M(H) is linear below and above the spin flop transition. Below H_c the slope of M(H) is given by the parallel susceptibility, $\chi_{//}$ and above H_c the slope of M(H) is given by the perpendicular susceptibility, $\chi_{\perp}$.

in which the largest ferromagnetic peak is observed when the field is along **a**.

At first glance, the field driven transition which occurs below T_N looks very similar to a spin-flop transition. Spin-flop transitions occur in uniaxial antiferromagnets when a magnetic field is applied along the spin direction. At low fields, the spin susceptibility is given by the parallel susceptibility, χ, which is small because the spins prefer to be anti-parallel rather than line up with the field. However, when the field is large enough to overcome the axial anisotropy, the spins "flop" into the perpendicular direction, as indicated in Figure 4-25(a). In the high field state, the spins are still mostly anti-parallel, but can rotate slightly in the direction of the field. The slope of M(H) above the critical field H_c is given by the perpendicular susceptibility, $\chi_{\perp}$, which is larger than χ. A schematic of M(H) is shown in 4-25(b).[36]

The spin-flop model predicts a larger slope of M(H) above the transition than below the transition. However, the field dependent moment of $Bi_2Sr_2CoO_{6+\delta}$ shown in Figure 4-24(b) does not show this behavior; the slope of M(H) above H_c is nearly equal to the slope below H_c. As we will discuss below, the neutron scattering measurements reveal a reconfiguration of the spins above the critical field which is more complex than a spin-flop.

4.3.3 Field dependent neutron scattering in samples with $T_N = 225$ K and $T_N = 115$ K

Field dependent neutron scattering reveals complex changes in the magnetic scattering when a magnetic field is applied along **a**. In addition to the observation of FM scattering, consistent with the SQUID measurements, we observe a change in the correlation of the AF spins along the c-axis.

We will focus on the field-dependence in two samples. One sample is xtal 2043, the field dependent susceptibility of which is shown in Figure 4-24. As mentioned, this sample has a high $T_N = 225$ K and therefore provides a close approximation of a crystal with mostly Co^{3+}. The other sample is xtal 1974b, which has a $T_N \sim T_{peak} = 125$ K and therefore a δ intermediate to the $\delta \simeq 0.5$ and $\delta \simeq 0.25$ crystals. However, two features of the 1974b crystal facilitate the analysis of the magnetic peaks in this sample compared to xtal 2043. The first is that this crystal has a better mosaic than xtal 2043. This is an important consideration in the analysis of the line-shapes of transverse scans. The second feature is that the FM behavior is more pronounced in xtal 1974b because it has a lower T_N.

For the field-dependence measurements, we looked at scattering in the (0KL) plane, with the field along the a-axis. This was the same set-up we used to study ferromagnetism in the $\delta \simeq 0.25$ samples. In addition, we continued to look at the (0, 0, 4) nuclear reflection for ferromagnetism.

Field-dependent neutron scattering measurements reveal both FM and AF Bragg peaks above H_c, and below T_N, in both samples. We first discuss the field induced FM peaks. Figure 4-26(a) shows transverse scans through the (0, 0, 4) nuclear position in xtal 2043an800C. The scans are taken at H = 0 and T = 180 K and after field cooling in 7 T to 7 K. There is a clear enhancement of the scattering in the 7 K, field-cooled scan compared to the scan measured at zero field. The enhancement corresponds to about 15% of the nuclear peak.

Similar measurements of the (0, 0, 4) reflection in xtal 1974b reveal the presence of a uniform moment. Longitudinal scans through the (0, 0, 4) peak, in zero field and at 7 Tesla, are shown in the top panel of Figure 4-27. The measurements are performed at 70 K, which is below the Néel temperature of 115 K measured in this sample. The additional scattering at this reflection corresponds to about 75% of the nuclear peak.

In both samples, the magnetic field induces dramatic changes in the AF structure.

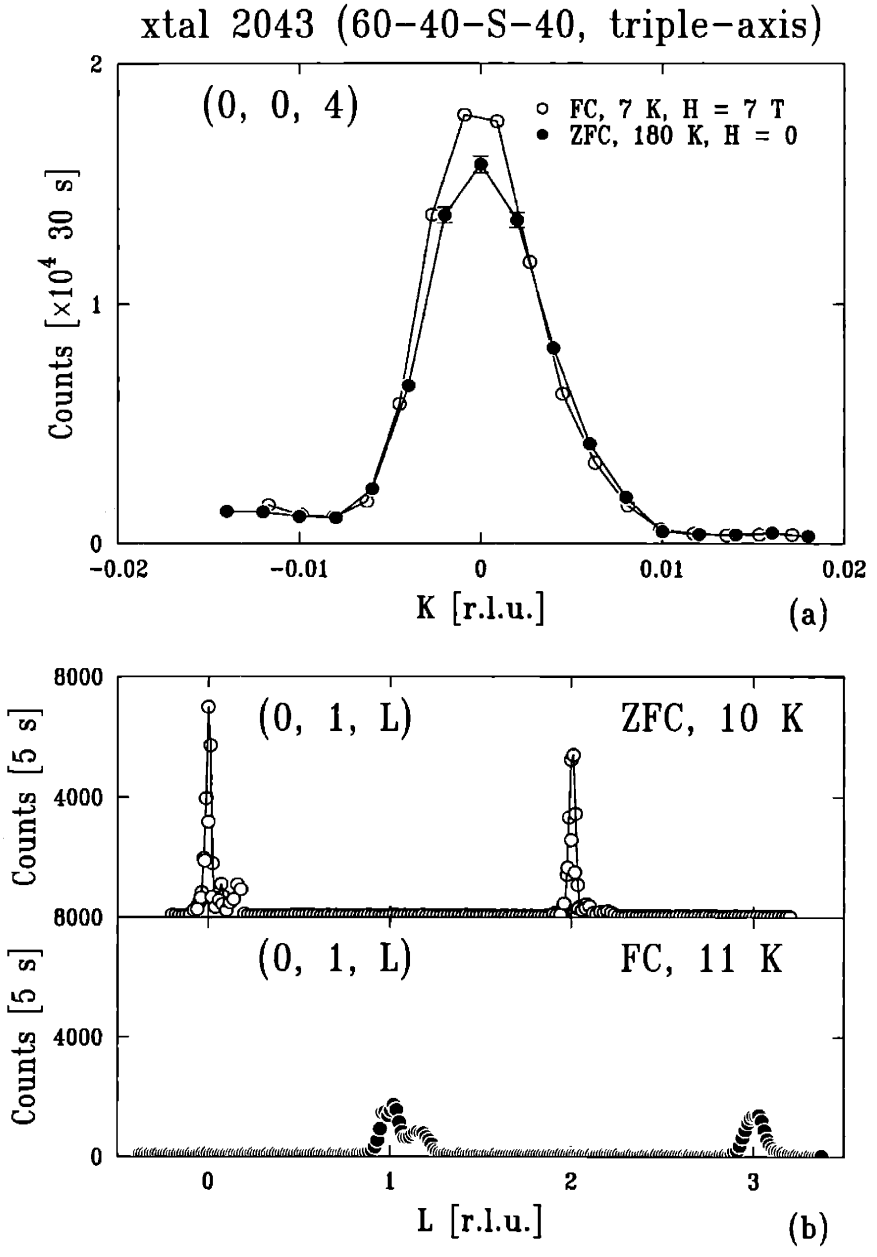

Figure 4-26: Field induced changes in the magnetic Bragg peaks in xtal 2043 (T_N = 215 K). The field is applied along **a**. (a) A transverse scan through (0,0,4) shows an enhanced signal resulting from ferromagnetic scattering when the sample is cooled in a field compared to when the sample is cooled in zero-field. (b) Cooling in a field also has a pronounced effect on the AF Bragg peaks. The top panel shows the AF Bragg peaks after cooling in zero field. These peaks are resolution limited and defined by the scattering condition (0, 1, L = *even*). The bottom panel shows the same scan after cooling in a 7 T field. The peaks have shifted to (0, 1, L = *odd*) and are less intense and much broader than the ZFC peaks. The shoulders on the peaks at (0, 1, 0) and (0, 1, 1) result from a nearby crystallite, which is most visible at low L where the scan is nearly transverse.

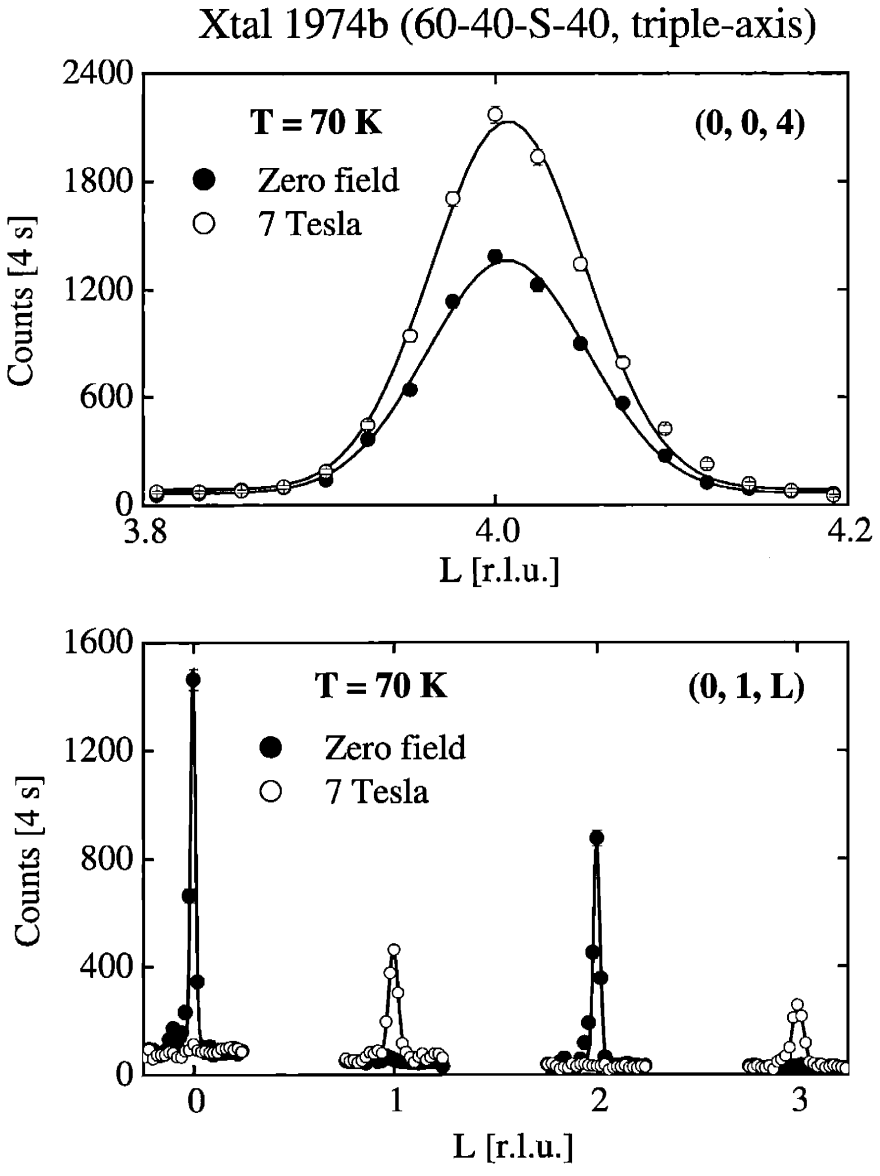

Figure 4-27: Field effect on the magnetic diffraction peaks in crystal 1974b, which has a T_N = 115 K and more pronounced ferromagnetic behavior than in xtal 2043. The measurements are performed at 70 K. Top panel: the intensity of the (0, 0, 4) nuclear peak increases by 75 % in a 7 T field. Bottom panel: the antiferromagnetic Bragg peaks shift from (0, 1, L = *even*) to (0, 1, L = *odd*) in a field.

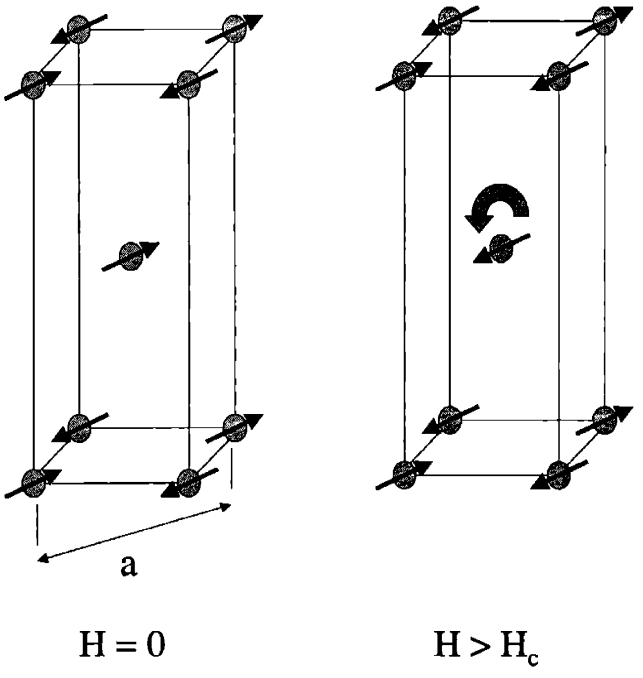

Figure 4-28: The shift in the AF peaks can be attributed to a change in the inter-layer stacking.

Figure 4-26(b) shows a scan along L through (0, 1, L) at 10 K after cooling in zero field and after cooling in 7 T in xtal 2043. When the sample is cooled in zero field, there are AF Bragg peaks at the L = *even* positions just as we expect for the antiferromagnetic structure. After cooling in a 7 Tesla field, however, these peaks disappear completely and new AF peaks appear at the L = *odd* positions. Similar behavior is observed in xtal 1974b (Figure 4-27, bottom panel).

The new reflections at (0, 1, L = *odd*) and the disappearance of the peaks at (0, 1, L = *even*), indicate a high field antiferromagnetic phase with a different spin arrangement than the H = 0 phase. The positions of the high field antiferromagnetic peaks are consistent with a 180° rotation of all of the spins in alternate layers of the low-field AF. This change in the stacking arrangement is indicated in Figure 4-28.

In both samples, the high field AF peaks have a significantly smaller peak intensity and are nearly twice as broad along L as the AF peaks in zero field; in other words, the high field AF peaks are no longer resolution limited. If we compare the integrated intensity of the (0, 1, 0) peak after zero-field cooling and the (0, 1, 1) peak after cooling in 7 T in

xtal 2043, we find that the scattering is nearly conserved when the field is applied. In xtal 1974b, we find that only half of the total intensity in the (0, 1, 0) peak is regained in the (0, 1, 1), high field peak.

The broadening of the high field antiferromagnetic peaks only occurs in the L direction; the peaks are resolution limited in the in-plane direction. This implies that the antiferromagnetic order at high field has a smaller magnetic correlation length along **c** than that at zero field. In Figures 4-29 and 4-30, the zero-field and high-field antiferromagnetic peaks are shown on an enlarged scale. The calculated spectrometer resolution function is indicated for the high-field antiferromagnetic peaks, which are defined by (0, 1, L = *odd*). Note that the mosaic width is broader in xtal 2043 than in xtal 1974b. Thus, the high-field antiferromagnetic peaks in xtal 2043 have an asymmetric shape.

4.3.4 Arguments for phase separation

In Figure 4-31, the field dependence of the (0, 1, 0) and (0, 1, 1) AF peaks, the FM contribution to the (0, 0, 4) peak and the square of the uniform moment, as measured in the SQUID, are shown for xtals 2043 and 1974b. (We do not show field dependence of the (0, 0, 4) FM peak for xtal 2043 because the magnetic field caused the sample to move during the measurement, so that the peak intensity actually *decreased.*) Clearly, the AF structure and the magnitude of the uniform moment both show strong variations at approximately the same field. One might conclude from the data in Figure 4-31 that the field induces a transition from a low-field AF phase to a complex high-field phase with both FM and AF components. However, there are several experimental results suggesting that the antiferromagnetic and ferromagnetic reflections observed at high field result from *distinct* magnetic domains.

The first argument is based on an analysis of the line-shapes of the antiferromagnetic and ferromagnetic reflections at high field. From Figures 4-29 and 4-30, it is clear that the high field AF peaks are much broader along L than the zero-field, antiferromagnetic Bragg peaks. Peak broadening indicates that the high-field antiferromagnetic order resulting in scattering at (0, 1, L = *odd*) is only correlated over short length scales perpendicular to the layers. On the other hand, the FM peak at high field has the same width along L as the nuclear peak and thus appears to be resolution limited. We might therefore immediately conclude that the high-field AF and FM peaks arise from different magnetic regions in the

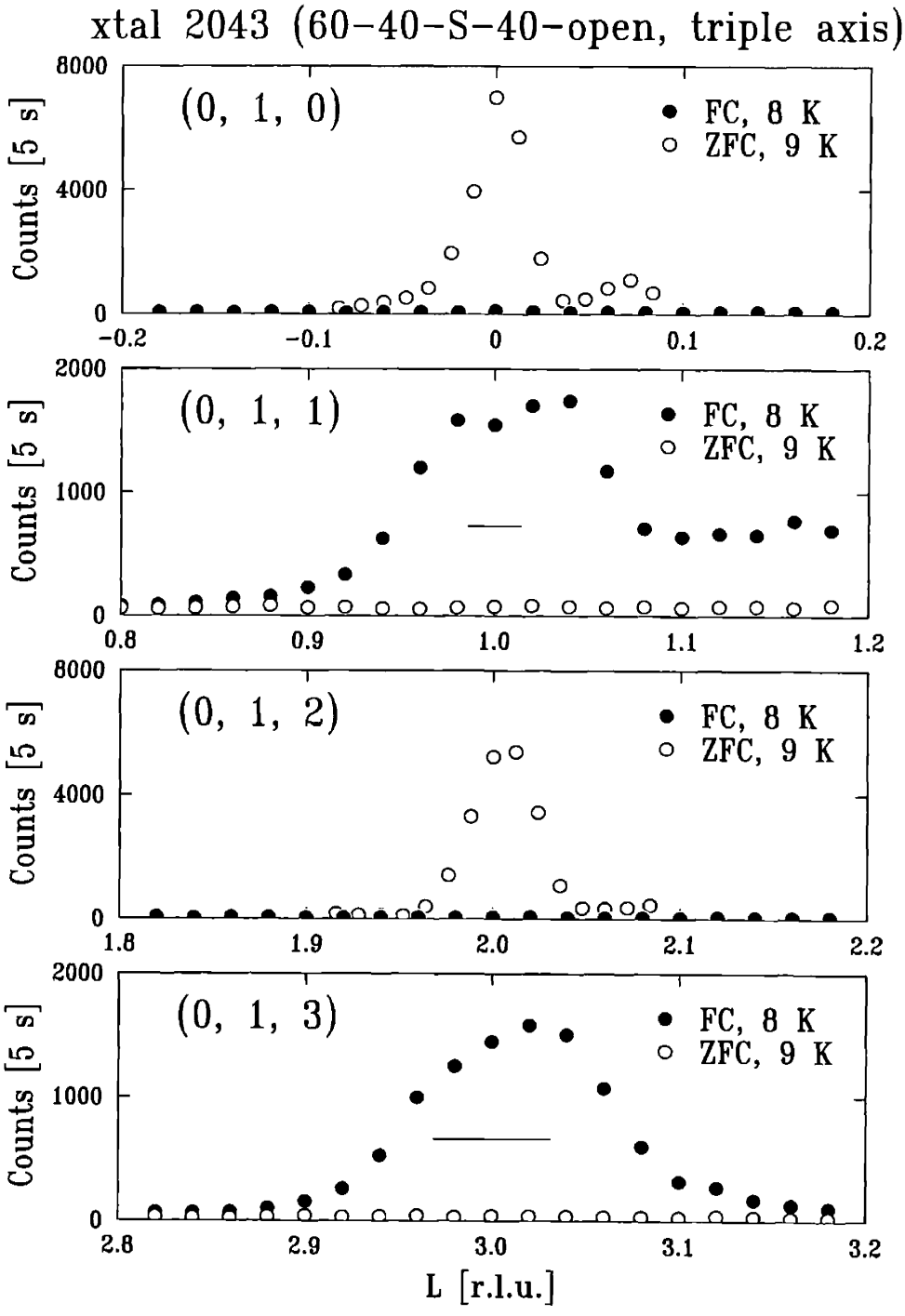

Figure 4-29: Scans along L through the (0, 1, L) reflections (L = 0, 1, 2 and 3) after cooling in a field of 7 Tesla (FC) and after cooling in zero-field (ZFC). The FC (0, 1, L = *odd*) peaks are not resolution limited. The horizontal line shows the resolution width at the (0, 1, 1) and (0, 1, 3) reflection.

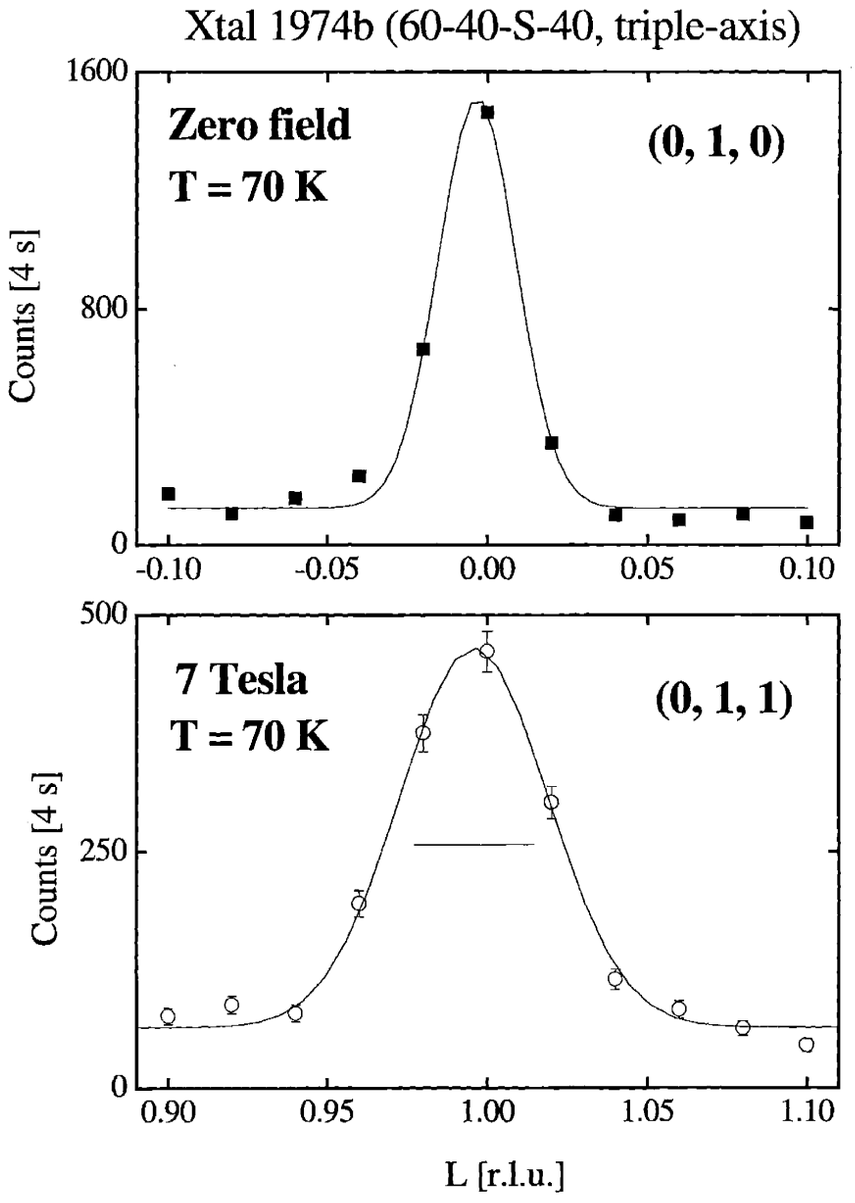

Figure 4-30: Comparison of the (0, 1, 0) peak at zero field (top panel) and the (0, 1, 1) peak at 7 Tesla (bottom panel). Both measurements are made at 70 K. The horizontal line shows the resolution width, which is narrower than the width of the (0, 1, 1) peak.

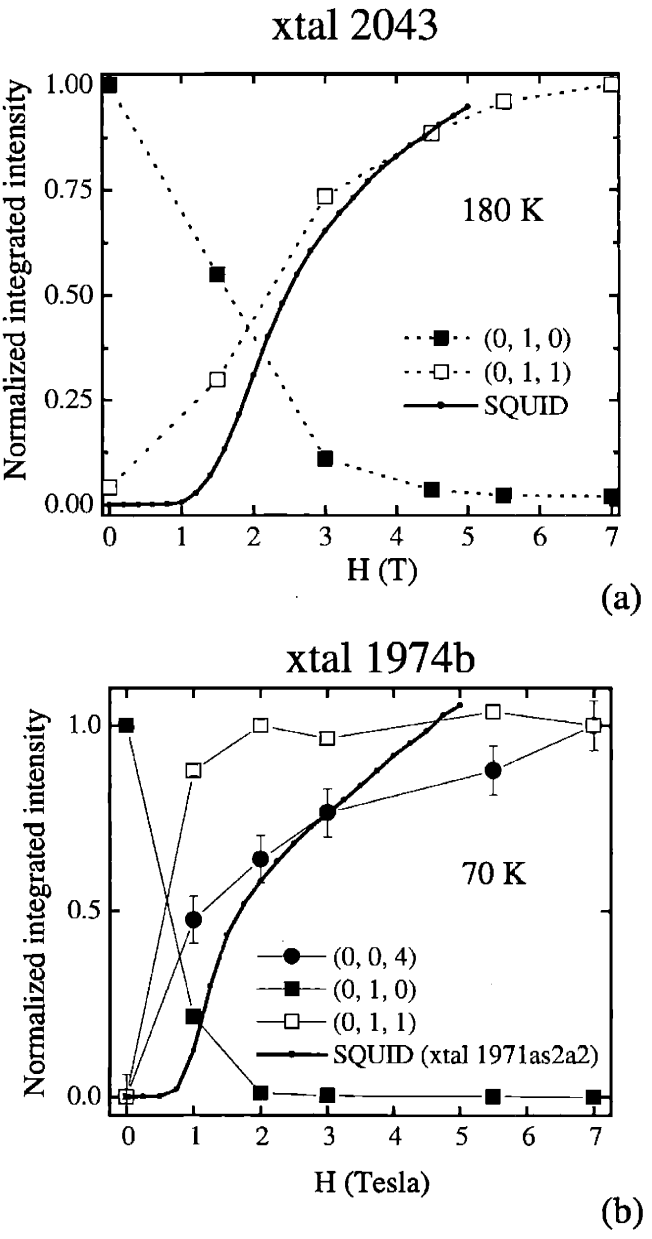

Figure 4-31: Field dependencies of the (0, 1, 0), (0, 1, 1) and (0, 0, 4) peak intensities and the uniform moment measured in the SQUID in xtals 2043 (top) and 1974b (bottom). The field dependence of the (0, 0, 4) peak intensity is not shown for xtal 2043 because the magnetic field moved the sample during this measurement. SQUID data is unavailable for xtal 1974b because the entire sample was used for neutron measurements. The field dependence of a similar sample with $T_{peak} = 115$ K is shown instead. The SQUID data are normalized to the neutron data at a common field.

sample.

Unfortunately, we can not make a strict comparison between an L scan through the (0, 0, 4) peak and an L scan through the (0, 1, 1) peak because the resolution is different for the two reflections. A scan along L through the (0, 0, 4) reflection is a longitudinal scan and is therefore dominated by the spectrometer collimation. On the other hand, the scan along L through (0, 1, 1) is nearly transverse to Q and may be dominated by the sample mosaic.

The first step is to determine the resolution width at the high field AF positions; namely, the (0, 1, L = *odd*) positions. The resolution FWHMs for the (0, 1, 1) and (0, 1, 3) high-field AF peaks in xtals 2043 and 1974b are shown in Figures 4-29 and 4-30. These peaks are clearly much broader than the spectrometer resolution. A similar analysis of the FM contribution to the (0, 0, 4) peak and the zero-field AF peaks in both crystals confirms that they are resolution limited.

We would now like to ask if we can extract the length-scale over which the ferromagnetic and antiferromagnetic regions are correlated. That is, assume that the ferromagnetic and antiferromagnetic peaks arise from distinct magnetic regions, each of which is correlated over a correlation length, $\xi_{c,FM}$ and $\xi_{c,AF}$, respectively. In addition, we will allow for the correlation length to depend on field. (An explanation for the field dependent correlation length will be given later.) We will define the correlation length as the HWHM of the Gaussian line-shape, S($\mathbf{Q}$), which is convolved with the resolution function to yield the observed peak. For the broad AF peaks we allow the width of the Gaussian to vary so as to obtain the best fit to the data after the convolution of S(Q) with the resolution function, while for the resolution limited peaks, we find the largest width of the Gaussian which does not lead to an observable broadening in the measured peak. The values for $\xi_{c,AF}$ and $\xi_{c,FM}$ should only be interpreted semi-quantitatively, since the assumption of a Gaussian line-shape is only approximately correct, particularly in the transverse scans which are sensitive to the sample mosaic.

For xtal 2043, we find $\xi_{c,AF} \sim 80$ $\mathring{A}$ for the high-field AF peaks, while for the resolution limited FM peaks we find a lower bound on $\xi_{c,FM}$ of 120 ± 30 $\mathring{A}$. A similar analysis of xtal 1974b, which has a larger ferromagnetic fraction and therefore leads to more reliable fits of the ferromagnetic peak, results in $\xi_{c,AF} = 185$ $\mathring{A}$ for the high-field AF peak and a lower bound on $\xi_{c,FM}$ of 240 ± 80 $\mathring{A}$.

The difference between the correlation lengths associated with the ferromagnetic and antiferromagnetic scattering suggests that the magnetic peaks observed at the positions (0, 1, 1) and (0, 0, 4) are not caused by scattering from different components of the same ordered moment (i.e. a field induced ferrimagnet or spin-flop of the antiferromagnet). However, this is an insufficient argument. The reason is that in a canted phase, it is possible to have the correlation length of the ferromagnetic component coherent over larger length scales than the antiferromagnetic component.

To confirm that the observed peaks at the FM and high field AF reflections do not result from a canted AF, we have performed polarized neutron measurements on xtal 1974b. As discussed in Chap. 2, a set-up with a polarizer at the monochromator and analyzer allows one to measure, independently, the neutron spin flip (SF) and non-spin flip (NSF) cross-sections for scattering from the ordered spins in the sample. We can therefore determine the direction of the spins resulting in the AF and FM reflections at high field.

For this measurement, the neutrons were polarized in the same direction as the applied field, which was along the a-axis of the sample. Thus, the ferromagnetic moment and the neutron spin polarization were both along **a**. We determined the beam's polarization by measuring the ratio of NSF to SF intensities at several structural reflections above T_c. We found flipping ratios between 25 and 30, corresponding to a polarization along **a** of 0.94 $\pm$ 0.01. The SF and NSF cross-sections of the FM (0, 0, 4) and AF (0, 1, 1) reflections were measured after cooling to 5 K in a 7 T field parallel to **a** and then reducing the field to 1 T. Lowering the field was necessary to maintain a high flipping ratio, but did not affect the high field state because of the large hysteresis.

In Figure 4-32, scans through the (0, 0, 4) and (0, 1, 1) peaks are shown for both the NSF and SF configurations. Also indicated is the background expected from imperfect polarization. The absence of SF processes above the background at the (0, 0, 4) reflection indicates that the FM moment is collinear with the a-axis, as expected. At the AF (0, 1, 1) reflection, the amplitude of the peak in the SF configuration corresponds to 4.75% of the amplitude of the NSF peak, which is only slightly higher than what is expected from imperfect polarization (3.3%).

We now explain why these results are inconsistent with a canting model. In a canted AF, the FM moment arising from a canting of AF spins is necessarily perpendicular to the direction of the staggered moment. This can be seen in the spin structure suggested in Figure

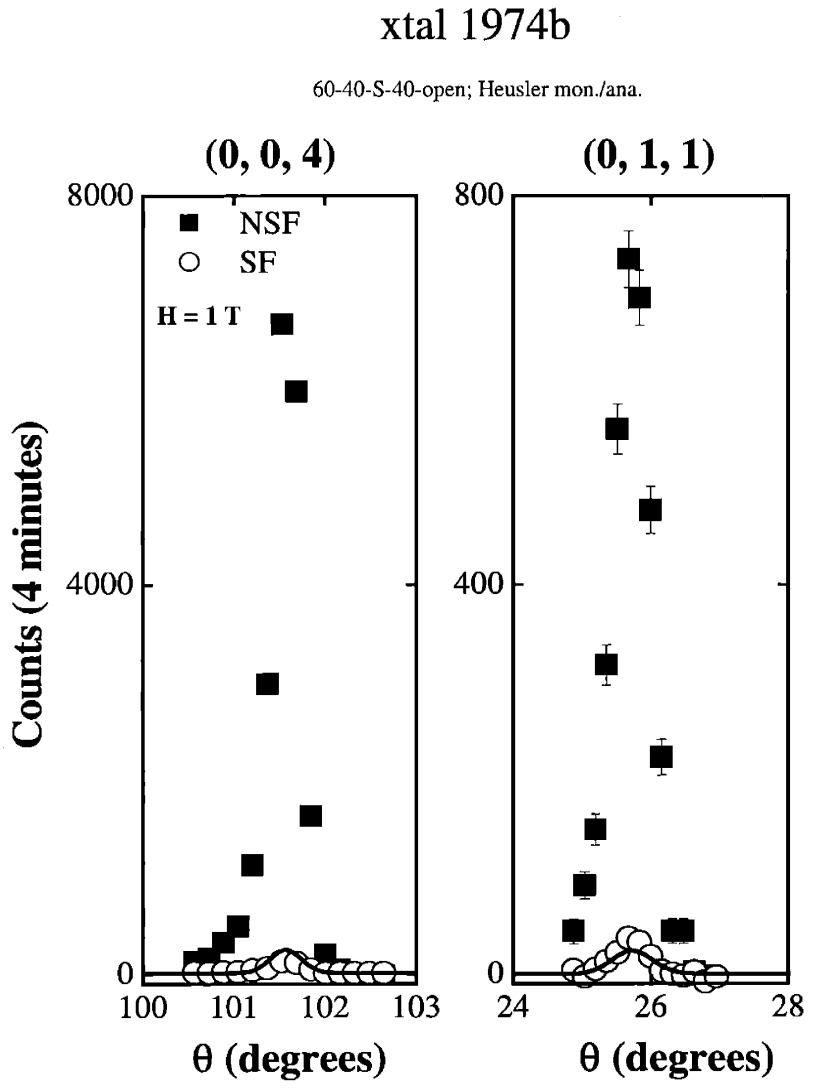

Figure 4-32: The FM (0,0,4) and AF (0, 1, 1) peaks are measured with the spectrometer in the non-spin flip (NSF) and spin-flip (SF) modes. The dark curve shows the scattering expected from imperfect polarization.

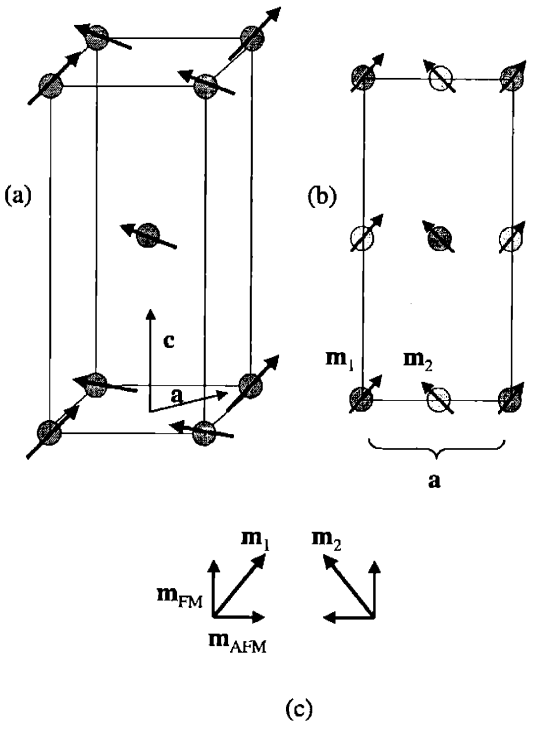

Figure 4-33: A canted magnetic phase in $Bi_2Sr_2CoO_{6+\delta}$, such as the one depicted in (a) (perspective view) and (b) (projection along **b**), would result in simultaneous FM and AF peaks at the positions observed in Fig. 4-26. (c) The uniform and staggered moments in the canted phase are perpendicular. If P is along M_{FM}, then spin-flip processes should occur at the AF reflections.

4-33, which shows a canted antiferromagnetic structure that would result in simultaneous ferromagnetic and antiferromagnetic scattering as seen in our samples. It follows that if the neutrons are polarized along the FM component, m_{FM}, of a canted AF, then the neutron spin polarization and *staggered* moment, m_{AF}, will be perpendicular to one another. Since a neutron's spin flips when scattered from a perpendicular moment, this situation will lead to 100 % SF scattering at the AF reflections. In this situation, the ratio of SF to NSF scattering at the AF reflection will be given by $(1+P)/(1-P)(1-\hat{\mathbf{Q}}\cdot\hat{\mathbf{S}})^2$. By including the $(1-\hat{\mathbf{Q}}\cdot\hat{\mathbf{S}})^2$ term, we allow for the fact that the spin direction will no longer be along **a** and may have a component parallel to Q.

We estimate that the SF scattering arising from an AF with a canted moment should be *at least* 1.4 times as great as the NSF scattering at the (0, 1, 1) reflection. (This corresponds to the case where m_{AF} is along **b** and is therefore nearly parallel to **Q** at the (0, 1, 1) reflection.) Therefore, the SF peak amplitude should be *greater* than the NSF peak amplitude. The SF scattering seen at the (0, 1, 1) reflection in Figure 4-32 is clearly much *less* than the NSF scattering. Therefore, the simultaneous FM and AF reflections seen at high field can not result from a canted AF.

Although simultaneous FM and AF reflections could result from a collinear ferrimagnetic ordering, the ratio of the FM to AF peak intensity in a ferrimagnet should not depend on the magnetic ordering temperature. Comparing xtals 2043 and 1974b, we see that the FM scattering, compared to the AF scattering, is much larger in xtal 1974b. However, xtal 1974b has a lower T_N than xtal 2043. This suggests that the ferromagnetism competes with the antiferromagnetism. As shown below, the suppression of the Néel transition temperature systematically results in an increase in the FM moment relative to the AF (staggered) moment.

For the above reasons, we propose that the FM and AF peaks result from distinct magnetic domains in the sample. We therefore interpret the intensity of the AF and FM Bragg peaks as a measure of the volume of AF and FM regions, respectively. To quantify the size of the ordered spin in both the FM and AF regions, we use the following normalization: The FM intensity at the (0, 0, 4) reflection is attributed to a uniform spin per Co ion, $\langle S_{FM} \rangle$, which lies along **a**. The additional scattering at the (0, 0, 4) reflection is therefore proportional to $\langle S_{FM} \rangle^2$. Similarly, the intensity at an AF reflection, such as the (0, 1, 0) peak at zero-field, is attributed to a spin $\langle S_{AF} \rangle$ on each Co in an antiferromagnet domain. We note that, in this picture, the measured intensity at the FM Bragg peak is proportional to the total volume of the sample which is in the FM phase. Similarly, the measured intensity at an AF Bragg peak is proportional to the volume of the sample which is in the AF phase. By normalizing either a FM or AF magnetic peak to a nuclear peak, which depends on the *entire* sample volume, we make an error in the estimate of the ordered moment in each magnetic phase of order $(\frac{V_{mag}}{V_{sample}})^{1/2}$, where V_{mag} is the volume of a magnetic phase and V_{sample} is the volume of the entire sample.

The magnetic cross-section also depends on the direction of the magnetic spin with respect to the momentum transfer vector **Q**. The polarized neutron scattering measurements show that the spin lies along **a** in both the AF and FM domains at all fields. Therefore, all peaks measured in the (0KL) scattering plane have $\mathbf{Q} \perp$ to $\langle \mathbf{S} \rangle$ and $1 - \hat{\mathbf{Q}} \cdot \hat{\mathbf{S}} = 1$.

We thus estimate that the FM moment for xtal 2043, with $T_N = 225$ K, is between 0.45 μ_b per Co ion if we normalize to the (0, 0, 4) reflection and 0.8 μ_b per Co ion if we normalize to the (0, 2, 0) reflection. On the other hand, for xtal 1974b, which has a T_N of 115 K, the FM moment is between 0.6 ((0, 2, 0) normalization)) and 0.8 μ_b/Co ((0, 0, 4) normalization). The range of values represents the uncertainty in determining the absolute

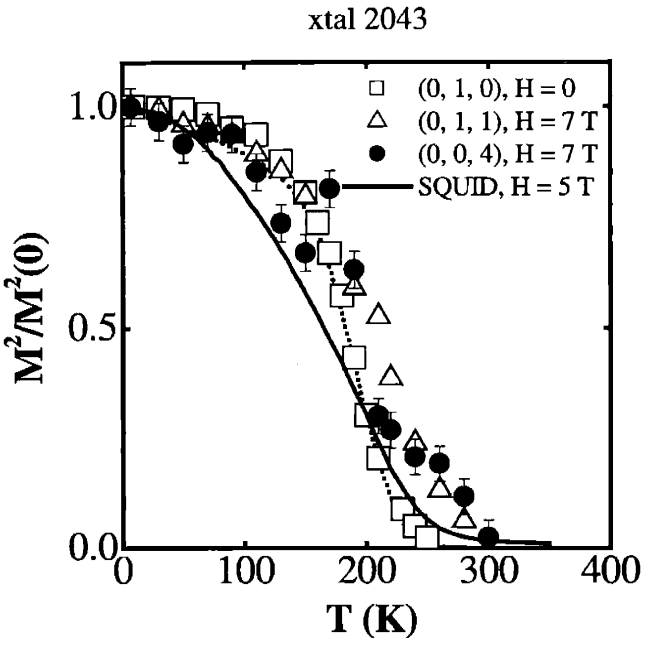

Figure 4-34: Temperature dependence of the 7 Tesla, field-cooled (0, 1, 1) and (0, 0, 4) peak intensities, the zero-field cooled (0, 1, 0) peak intensity, and the square of the moment measured in the SQUID in crystal 2043. The data are normalized to base temperature.

intensity of the different nuclear peaks for the normalization.

Figure 4-34 shows the temperature dependencies of the integrated intensity of the (0, 1, 0) peak in zero-field, the (0, 1, 1) and (0, 0, 4) peaks in 7 Tesla, and a SQUID measurement of the square of the uniform moment in a 5 Tesla field in xtal 2043. The (0, 1, 0) and (0, 1, 1) peaks are proportional to the square of the ordered moment in the AF phase at zero and high-field, respectively, while the (0, 0, 4) peak is proportional to the square of the ordered moment in the FM phase. All of the data are plotted in the form $M^2(T)/M^2(0)$. Remarkably, the ordering temperatures for the zero and high field AF phases, as well as the FM phase, appear to be the same. At first sight, this appears to be at odds with our arguments for phase separation: if the AF and FM phases are distinct, then they should have distinct ordering temperatures. However, we believe that the coincidence of the ordering temperatures can be explained by considering the interaction between the two magnetic domains, such that the ordering of one phase drives the ordering of the other. As we discuss below, the data suggest that the ordering of spins in the AF phase induces order in the FM phase.

4.3.5 Doping dependence: summary of results

We now discuss the observed growth in the ferromagnetic behavior as δ is reduced from $\delta \simeq 0.5$ to $\delta \simeq 0.25$. We have already shown that removal of oxygen not only suppresses T_N but enhances the ferromagnetic peak in χ_a by nearly two orders of magnitude between the sample with $T_{peak} = 295$ K and the sample with $T_{peak} = 25$ K (See Figure 4-22). By comparing the neutron data to susceptibility measurements, we find that for samples with $T_{peak} \geq 125$ K, T_{peak} is approximately T_N, while for $T_N < 125$ K, T_{peak} and T_N differ. In addition, we find that T_c from the Curie-Weiss fits of the paramagnetic susceptibility is $\simeq T_{peak}$ for samples with $T_{peak} > 100$ K, while for samples with $T_{peak} < 100$ K, T_c remains fixed at around 100 K. This suggests that the AF order determines the ordering of the FM phase when T_N is greater than ~ 125 K, but when T_N is below 125 K, the FM and AF orders decouple with T_c determined by the intrinsic properties of the FM phase. These results are summarized in Figure 4-35, where T_c and T_N are plotted as a function of T_{peak}. As noted in Chapter 3, we use T_{peak} to differentiate samples with different oxygen content, since this is more easily measured than δ. We note that while the AF order is likely very sensitive near the composition $\delta \sim 0.25$, T_{peak} shows little variation. This may explain why we observe a slightly lower T_{peak} for the sample which has $T_N \sim 80$ K compared to the sample with $T_{peak} = 48$, which has no observable long-range AF order. Since the substantial rounding near the onset temperature for AF ordering prevents a reliable fit of the data from sample to sample, we define T_N in Figure 4-35(a) as the temperature at which the intensity of the AF Bragg peak is 10% of the maximum intensity. T_c is the FM Curie-Weiss temperature determined from the Curie-Weiss fits of the paramagnetic susceptibility. There are fewer points for T_N than T_c because we can only measure T_N with neutrons, while T_c is easily determined from the susceptibility.

In Figure 4-35(b), the ordered AF moment at H = 0, $\langle M_{AF} \rangle = g\langle S_{AF} \rangle$, and the field induced uniform moment $\langle M_{FM} \rangle = g\langle S_{FM} \rangle$, determined from neutrons, are plotted as a function of T_{peak}. The data in Figure 4-35b show that as oxygen is removed and T_N is suppressed the FM moment increases and the AF staggered moment decreases.

Table 4.3.5 shows the calculated magnetic moment from magnetic neutron scattering measurements compared with the moment measured in the SQUID magnetometer. There is some variation in the magnetic moment calculated from the neutron peaks depending on

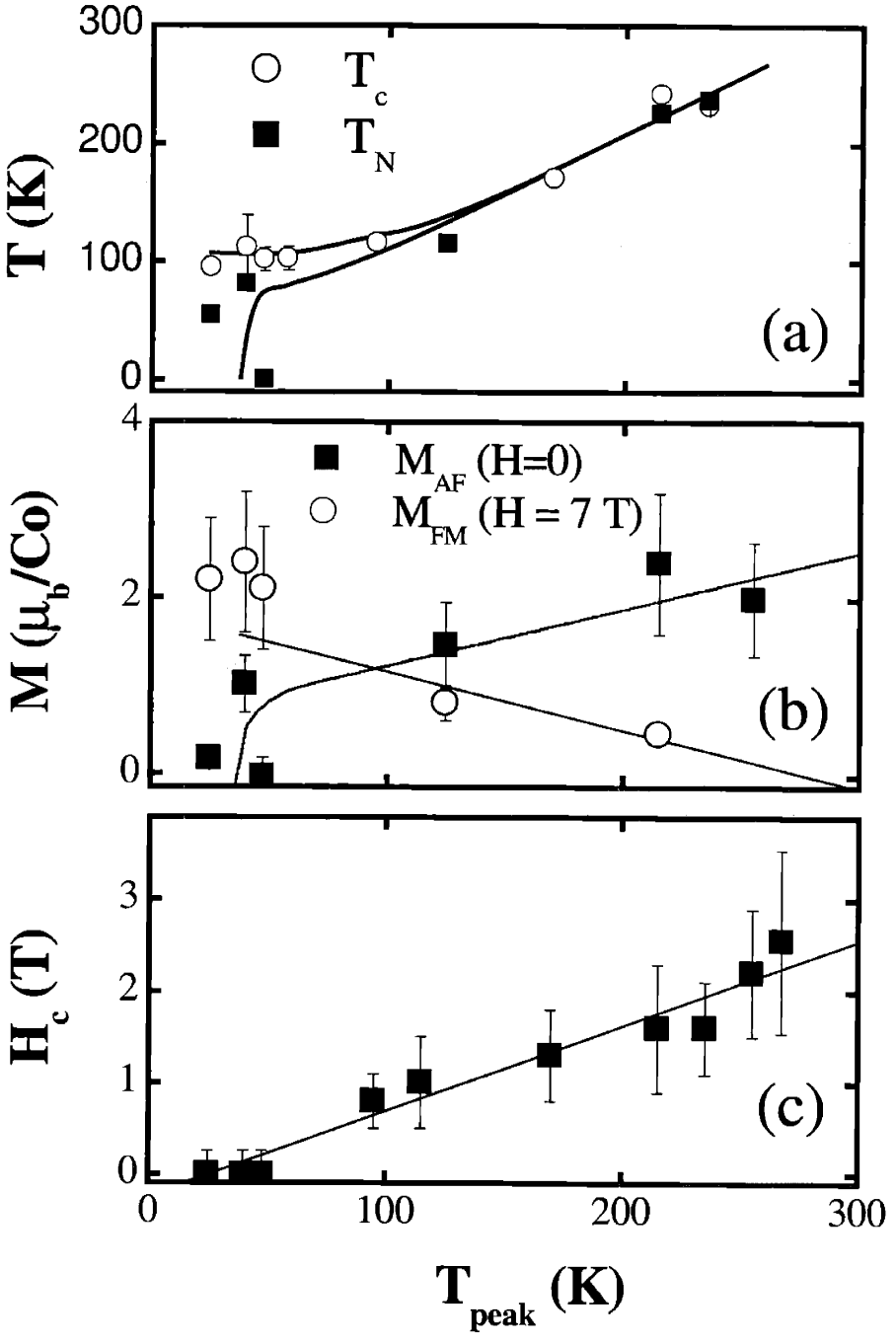

Figure 4-35: (a) T_N, determined by neutrons, and T_c, determined from the Curie-Weiss fits of the susceptibility, versus T_{peak}. The lines are guides to the eye. Below $T_{peak} \sim 100$ K, T_c is constant while T_N drops abruptly to zero. (b) Calculated AF moment, $\langle M_{AF} \rangle$, and FM moment $\langle M_{AF} \rangle$ as a function of T_{peak}. The point at $T_{peak} = 47.5$ K corresponds to the sample with no in-plane AF order, discussed in Section 4.2. The lines are guides to the eye. (c) Decrease in the critical field, H_c, with decreasing T_{peak}. The error bars correspond to the larger of the width of the transition (i.e. the HWHM of dM/dH) or the hysteresis.

T_N (K)	M_{AF}	M_{FM}	M_{FM} SQUID
237	2.5±0.8(a)	-	-
225	2.4±0.8(b) 3.7±1.2(c)	0.45±.15(b) 0.8±.3(c)	0.38
115	1.9±0.7(b) 1.8±0.7(c)	0.8±0.2(b) 0.6±0.2(c)	-
81.5	1.3±0.4(b) 1.3±0.4(c)	2.1±0.7(b) 1.9±0.6(c)	1.7
< 55	0.25±0.08(b)	2.2±0.7(b)	1.9
No in-plane AF order	-	2.4±0.8(b) 1.9±0.6(c)	1.75

Table 4.4: Calculated $\langle M_{AF} \rangle$ measured at zero-field and $\langle M_{FM} \rangle$ measured at 7 Tesla. For comparison, the field induced FM moment measured in the SQUID at 5 K after cooling in 5 Tesla is also shown. $\langle M_{AF} \rangle$, $\langle M_{FM} \rangle$ and the SQUID FM moment are all in units of μ_b/Co. Multiple entries for the same sample correspond to normalization to different nuclear peaks: (a) normalization to the (0, 0, 2) reflection, (b) normalization to the (0, 0, 4) reflection, and (c) normalization to the (0, 2, 0) reflection.

which nuclear peak is used for normalization. This probably results from extinction effects. For most samples, the table shows two entries, one for normalization with the (0, 0, 4) nuclear peak, which is a weak nuclear reflection, and the second line for normalization with the (0, 2, 0) nuclear peak, which is a strong nuclear reflection. The errors correspond to plus or minus 30%.

Figure 4-35(c) is a plot of the critical field, H_c, as a function of T_{peak}. Since the critical field can only be measured by first cooling the sample in zero field to below T_N and then measuring the field dependence, there is some error in determining H_c at low temperatures because of the hysteresis. To avoid hysteresis, the critical field is measured for temperatures within 25% of T_N. The critical field appears to vanish for samples with T_{peak} between 95 K and 45 K, which is the same temperature range over which T_N and T_{peak} appear to decouple. This suggests that the critical field depends on the fraction of the sample that is in the AF phase.

Figure 4-36 shows the temperature dependence of the integrated intensities of the (0, 1, 0) Bragg peak at H = 0 and the (0, 1, 0) and (0, 0, 4) peaks in a field H > H_c for samples with T_{peak} (T_N) = 215 (225), 125 (115), 40 (81.5), 47.5 (0) K and 25 (< 55) K. The solid line in Figure 4-36 is the square of the uniform moment measured in the SQUID in a FC measurement (5 Tesla). The dotted line is used to emphasize the (0, 1, 0) data,

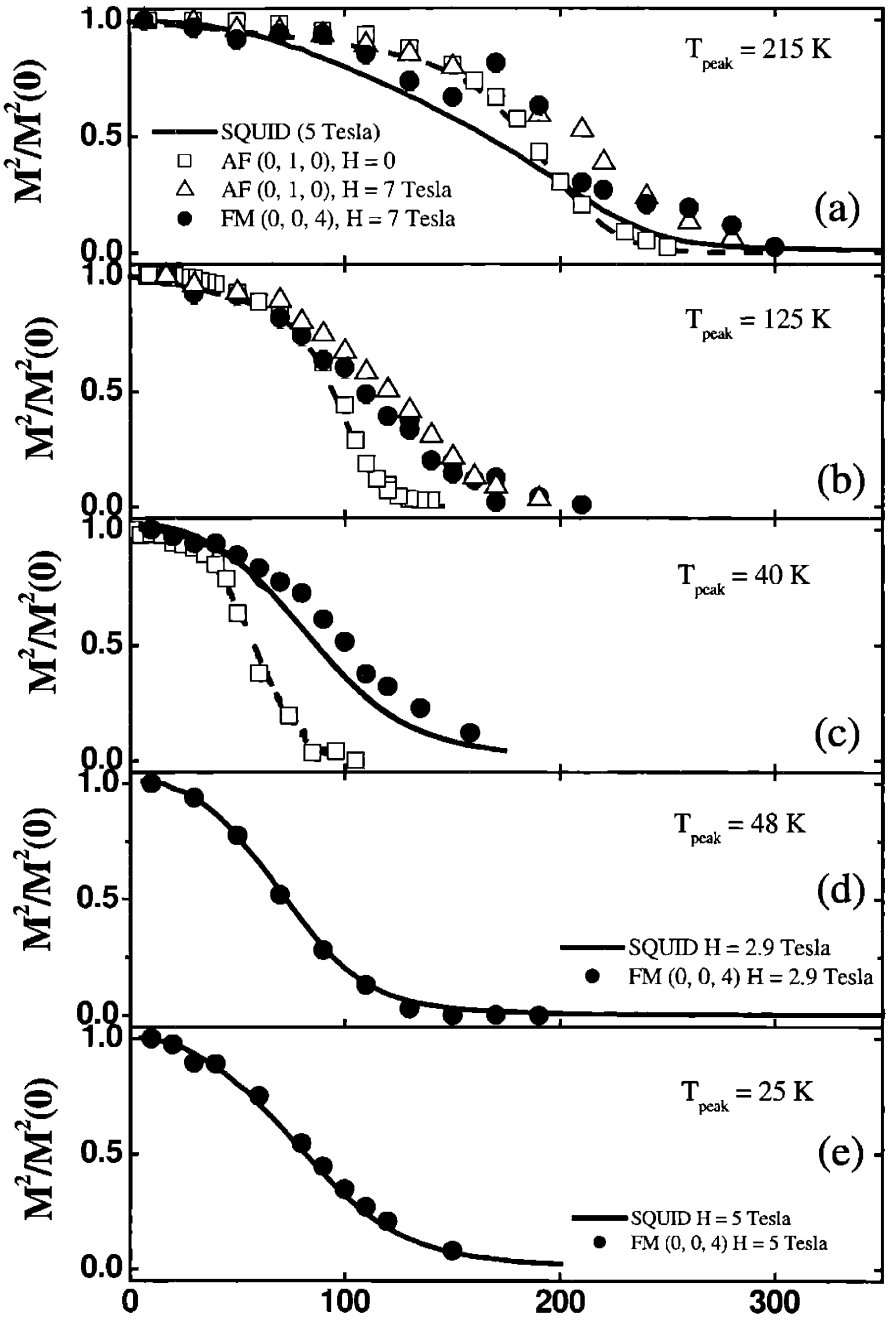

Figure 4-36: Temperature dependence of the (0, 1, 0), (0, 1, 1) and (0, 0, 4) integrated intensities measured in samples with (a) T_{peak} (T_N) = 215 K (225 K), (b) 125 K (115 K), (c) 40 K (81.5 K), (d) 48 K (no in-plane AF order) and (e) 25 K (may contain trace AF order with T_N < 55 K). The total moment measured in the SQUID is indicated by a solid curve for each sample, except for in (b), where we do not have this data. The applied field in the SQUID measurement is equal to 5 T in the samples show in (a), (c), and (e) and 2.9 T for the sample in (d). The field for the neutron measurements are 7 T, except where otherwise noted. All measurements in a magnetic field are measured after field-cooling. The data are normalized to base temperature.

which reflect the zero-field AF order parameter. In (a) and (c) the SQUID data show a more rapid fall off with temperature than indicated by the (0, 0, 4) Bragg peak. This reflects the lower field available for the SQUID measurement. There are no SQUID data available for the sample in (b). In (c) the temperature dependence of the (0, 1, 1) peak at high field is not shown because we did not take these data and in (d) there is no peak at (0, 1, 1), consistent with the disappearance of Co^{3+} AF order. The data clearly show that when the Néel temperature is below about 125 K, the FM order is independent of the AF ordering: Comparing (c), (d) and (e), the onset temperature for the FM moment occurs at approximately the same temperature, even though the AF ordering has disappeared in (d) and exists in only trace amounts for the sample shown in (e).

We have not, up to this point, considered the zero field behavior of the FM domains in a sample exhibiting phase separation. In the T_N = 115 and 225 K samples, the ferromagnetic scattering at the nuclear positions disappears below the critical field. We believe that this occurs because the spins in the ferromagnetic domain have relaxed to a zero-field ground state with vanishing microscopic moment. Preliminary zero-field measurements of xtal 2043 (T_N = 215 K) and xtal 1955 (T_N = 235 K), reveal magnetic peaks at the (0, 0, L = *odd*) reflections, as in the pure ferromagnetic samples. These peaks disappear at T_N, as does the field induced uniform moment. Unfortunately, we have not performed these measurements in a set-up with a magnetic field to check that the peaks shift to (0, 0, L = *even*) at the critical field.

Although more work remains to be done to unambiguously identify the zero-field magnetic structure of the FM phase in mixed-phase samples, the measurements described above provide strong evidence for an anti-parallel stacking of adjacent FM layers at zero-field. We note that the three dimensional ordering of the FM domains at the same temperature as the AF domains implies an interaction between the two domains. We will discuss this in more detail below.

4.3.6 Resistivity measurements

Given the dramatic changes in the magnetism, it is surprising that the resistivity is relatively insensitive to doping. Figure 4-37 shows the temperature dependent resistivity for samples with T_{peak} between 40 and 270 K. On this Arrhenius plot, all of the resistivity curves have the same slope above 200 K indicating a constant activation energy, $E_a \sim 0.25$ eV. There

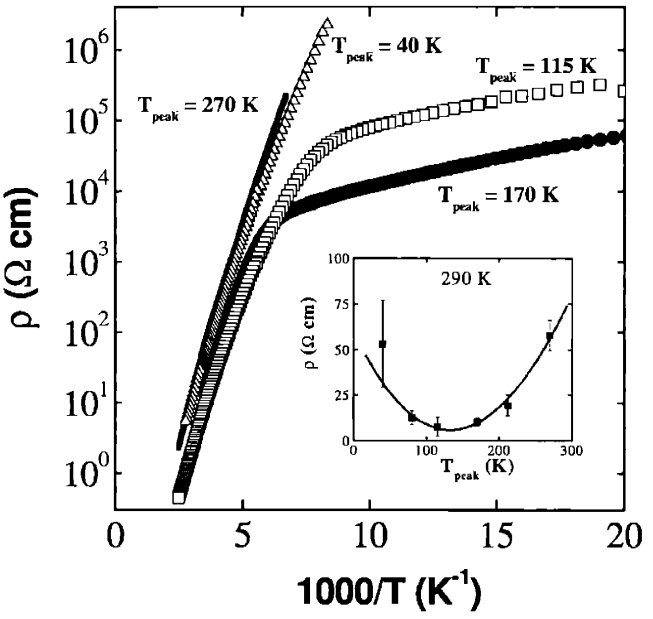

Figure 4-37: Temperature dependent resistivity for samples with different T_{peak}. Samples with different T_{peak} show the same activated behavior, with an activation energy ~ 250 meV. The inset shows the resistivity measured at 290 K as a function of T_{peak}. The error bars result from uncertainty in the geometric path of the current in the 4-probe measurement.

is no feature in $\rho(T)$ at T_{peak} for any of the samples, suggesting that the magnetic order has no significant effect on the transport. The inset shows the magnitude of the resistivity measured at 290 K, for which there is a distinct minimum for samples with T_{peak} near 115 K. The resistivity curves for $T_{peak} = 175$ and 115 K show a crossover to more weakly activated behavior with decreasing temperature, which may be related to the minimum in resistivity.

Although crystals with low T_N are expected to have large FM domains, there is no evidence for a transition to metallic behavior as one finds in the manganites.

Chapter 5

Oxygen annealing

In Chapter 3, we showed that it is possible to reverse the process of taking oxygen out of as-grown crystals. We showed this by reducing a sample such that it had very low T_{peak} ($\sim$ 25-30 K) and then annealing it again in oxygen up to 900 C. The re-oxygenated crystals had $T_{peak} \sim 270$ K and had similar properties to as grown crystals.

However, the removal of oxygen is only reversible if oxygen is re-introduced at a temperature $\geq$ 900 C. When oxygen is re-introduced at temperatures $<$ 900 C, the re-oxidized samples do not show the same properties as as-grown samples.

Figure 5-1(a) shows the TGA mass trace of a reduced sample (xtal 1975C, $T_{peak} = 48$ K and $\delta \simeq 0.25$) which is annealed at 560 C for 2 hrs. in a flow of oxygen. The mass increase corresponds to ~ 0.19 extra moles of oxygen per formula unit, so that the re-oxidized crystal has a $\delta \sim 0.44$. The susceptibilities of the reduced sample and the re-oxidized sample are shown in Fig. 5-1(b).

The re-oxidized crystal has a $T_{peak} \sim 235$ K, which is close to the value of T_{peak} expected in an as-grown sample and shows that oxygen does indeed re-enter the sample and re-oxidize Co^{2+} to Co^{3+}. However, the re-oxidized sample does not show the same ferromagnetic behavior as an as-grown crystal with the same T_{peak}. The field-cooled ferromagnetic moment is absent, and field dependence measurements show no jump in the moment. The peak in the susceptibility is also small compared to that found in an as-grown crystal with the same T_{peak}. For example, xtal 2017 has a similar $T_{peak} \sim 235$ K, but it has a peak amplitude of 0.02 cm^3/mole. This is four times larger than the peak measured in Fig. 5-1(b), which has an amplitude of 0.005 cm^3/mole.

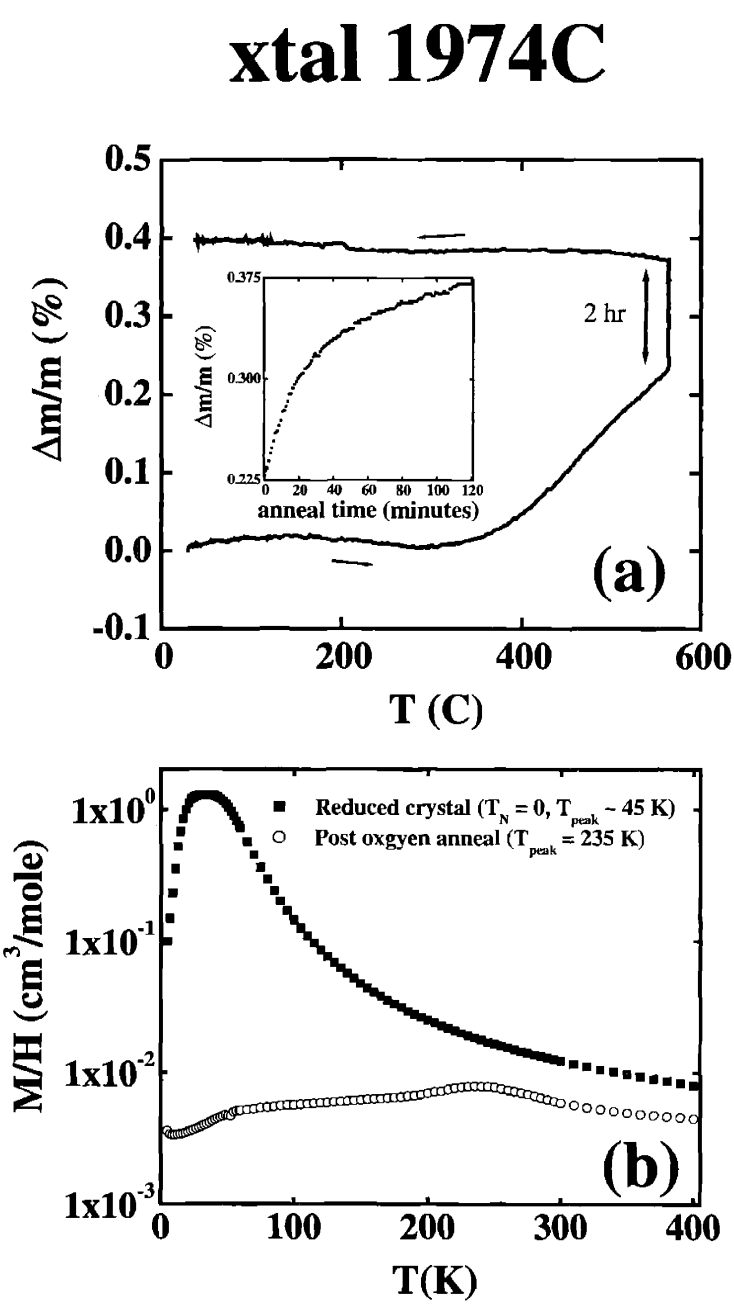

Figure 5-1: (a) TGA mass trace showing re-oxidation of xtal 1974 C. The sample is heated in a flow of pure oxygen and held at a maximum temperature of 560 C for 2hrs. The inset shows the percent change in mass a function of time at 560 C. (b) The susceptibility before (dark squares) and after (open circles) the oxygen anneal. T_{peak} increases from 47.5 K to 235 K.

Further annealing in oxygen at 400 C for 4 hours, after the 560 C anneal, resulted in little change in the susceptibility. However, by annealing the sample at progressively higher temperatures in oxygen, it was possible to push T_{peak} up to 295 K. This is the highest value of T_{peak} we have obtained. The top panel of Figure 5-2 shows the susceptibility curves which resulted from the 560 C, 400 C and the progressively higher temperature anneals. The anneals were performed in succession. For the 400, 600 and 1st 800 C anneal, the time at the maximum temperature was 4 hours. For the 560 C and 400 C anneal, the cool-down time was 5 C/min while for the 600 and 800 C anneal, the cool-down time was 0.25 C/min.

It should be pointed out that annealing $Bi_2Sr_2CoO_{6+\delta}$ in oxygen above 800 C results in the formation of a second phase, the double-layered structure $Bi_2Sr_3Co_2O_\delta$.[29] Therefore, the magnitude of the susceptibility normalized to the sample mass appears to decrease with increasing annealing temperature. In addition, there is a Curie susceptibility at very low temperatures, which increases in magnitude the longer the samples are annealed. The data in Figure 5-2 have been partially corrected for these effect.

None of the annealing stages up to 800 C result in a return of the ferromagnetic properties. In fact, the addition of oxygen results in an increase in T_{peak} and a decrease in the magnitude of the susceptibility at T_{peak}. Figure 5-2(b) shows the field cooled moment as a function of temperature after the 560 C, 400 C, 600 C and 1st 800 C anneal. None of the samples show the ferromagnetic-like field-cooled moment; the field cooled moment in these annealed samples looks almost identical to the zero-field cooled moment, except at very low temperatures.

When the sample is annealed in oxygen at 900 C, however, the large field-cooled ferromagnetic moment and sharp peak at T_{peak} re-appear. The zero-field cooled susceptibility and field-cooled moment after the 900 C anneal are shown in Figures 5-2(a) and (b) as dark curves. The susceptibility after the 900 C anneal has a sharp peak at around 250 K and a field cooled moment $\sim 0.25\ \mu_b$/Co.

It should be noted that for the 900 C anneal, the cooling rate was increased to 5 C/min while for the previous anneals, the cooling rate was 0.25 C/min. The increased rate of cooling below 900 C was a significant factor. Since the susceptibility of the sample after being annealed at 600 or 800 C in oxygen did not show the ferromagnetic-like behavior, it was necessary to cool the sample through these temperatures rapidly. To confirm this, a subsequent anneal at 800 C in oxygen was performed, with a slow cooling time of 0.25

C/min.. After the anneal, the susceptibility of the sample had a higher T_{peak} of 290 K, as shown in Figure 5-2 and the peak and the field cooled FM moment were approximately a factor of two smaller after the slow 800 C anneal than after the 900 C anneal.

This annealing study suggests that it is not only necessary to go to high temperatures in oxygen to achieve the phase separation, but the sample must also be *quenched* below temperatures (400-800 C) where only the uniform, antiferromagnetic phase forms. This may explain why as-grown crystals exhibit phase separation, since the crystal growth occurs at a very high temperature and the sample cools fairy quickly. At a pulling rate of 2mm/hr, the sample cools from the melt to 400 C in $\sim$ 10 hours.

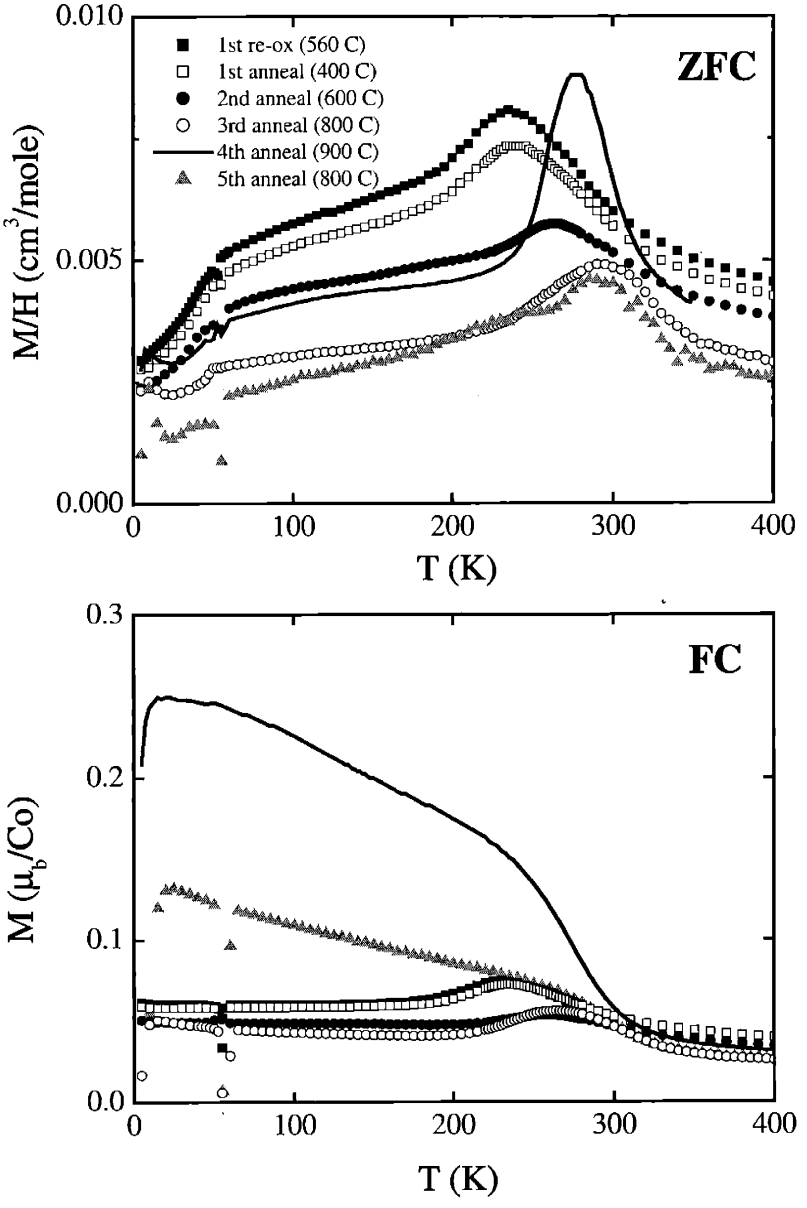

Figure 5-2: Top panel: ZFC susceptibility measured in xtal 1974C as a function of the annealing temperature. All of the samples are annealed in pure oxygen. The key shows the chronology of the anneals. With increasing annealing temperature, the T_{peak} increases and the magnitude of the susceptibilty decreases. However, when the sample is annealed at 900 C (solid curve), the peak magnitude increases and shifts slightly to lower T_{peak}. Bottom panel: The field-cooled, ferromagnetic-like moment only re-appears after the 900 C anneal. When the sample is then annealed again at 800 C, the field-cooled moment decreases slightly. The down-turn at low temperatures results from the subtraction of a Curie susceptibility.

Chapter 6

Discussion

The most important results that we have discovered are as follows. From the doping dependence studies, the primary observation is that the removal of oxygen results in a suppression of the in-plane antiferromagnetic order characteristic of the crystal with mostly Co^{3+}. Both T_N and $\langle M_{AF} \rangle$ decrease as a result of vacuum annealing. Coincident with the suppression of antiferromagnetic order is an enhancement of the peculiar ferromagnetic features; namely, the magnitude of the ferromagnetic peak at T_{peak} and the field induced ferromagnetic moment *increase* with decreasing T_N. In addition, the field dependent neutron scattering results provide compelling evidence for magnetically distinct phases in samples with $0.25 < \delta < 0.5$. The arguments for magnetic phase separation are three-fold. First, the antiferromagnetic and ferromagnetic peaks at high field have different correlation lengths along **c**. Second, the polarized neutron measurements show that both the high-field AF and FM moments lie along **a**. This experiment rules out the existence of a canted phase as the origin of the simultaneous antiferromagnetic and ferromagnetic peaks. We argue that although a ferrimagnetic ordering has simultaneous antiferromagnetic and ferromagnetic moments which share a common axis, one would not expect the ratio of the uniform moment to the staggered moment to increase as the transition temperature decreases. Thirdly, a model of distinct phases provides a simple explanation for the systematic increase in the integrated intensity of the ferromagnetic peaks relative to the antiferromagnetic peaks as T_N is reduced.

We propose a model in which two phases, exhibiting distinct magnetic order, co-exist for $0.25 < \delta < 0.5$. One phase exhibits ferromagnetic ordering in the plane, characteristic of the

$\delta = 0.25$ phase with equal amounts of Co^{2+} and Co^{3+}. The other phase exhibits in-plane antiferromagnetic order, as observed in the $\delta = 0.5$ phase with all Co^{3+}. We propose that the antiferromagnetic phase is a Co^{3+} rich phase and that the ferromagnetic phase has an equal concentration of Co^{3+} and Co^{2+}. For the purpose of discussion, we will refer to these phases as the AF phase and the FM phase.

The magnetization of $Bi_2Sr_2CoO_{6+\delta}$ evolves smoothly with decreasing δ to exhibit purely ferromagnetic behavior. This suggests that it is the removal of oxygen that increases the volume of the FM phase, which is Co^{2+} rich, while suppressing the antiferromagnetic ordering of the Co^{3+} spins in the AF phase. We interpret the removal of one oxygen as equivalent to the addition of two Co^{2+} sites, and hence two ferromagnetic bonds, to the magnetic lattice. The decrease in the Néel transition temperature with decreasing δ likely results from finite amount of Co^{2+} in the AF phase. In other words, we understand the addition of Co^{2+} to the cobalt-oxide plane to result in both an increase in the volume of the FM phase and a dilution of the AF phase.

In this chapter, we develop a microscopic picture of the magnetism occurring in $Bi_2Sr_2CoO_{6+\delta}$ for $0.25 \leq \delta \leq 0.5$. We first discuss a plausible explanation for antiferromagnetic coupling between the spins on Co^{3+} sites and ferromagnetic coupling between spins on adjacent Co^{2+} and Co^{3+} sites. We then propose a simple model to explain the field dependence in mixed phase samples. We show that this model maps to the Random Field Ising model in two-dimensions in the limit that the FM clusters are small.

6.1 Microscopic model for ferromagnetism and antiferromagnetism

We need to explain the interaction which results in antiferromagnetism between nearest neighbor spins on Co^{3+} sites and ferromagnetism between neighboring Co^{2+} and Co^{3+} spins. We discuss first the situation in which all of the sites are Co^{3+}. The spin state of Co^{3+} in the samples with δ near 0.5 is closest to S = 1, the intermediate spin state of trivalent Co. Co^{3+} at perfectly octahedral sites is usually found to have S = 0. However, a tetragonal distortion of the surrounding oxygen ions [Figure 6-1(a)] favors the intermediate spin state of Co^{3+} because the crystal-field energy difference between the e_g and t_{2g} orbitals is lowered with respect to the electron-electron exchange. In $Bi_2Sr_2CoO_{6+\delta}$, the tetragonal

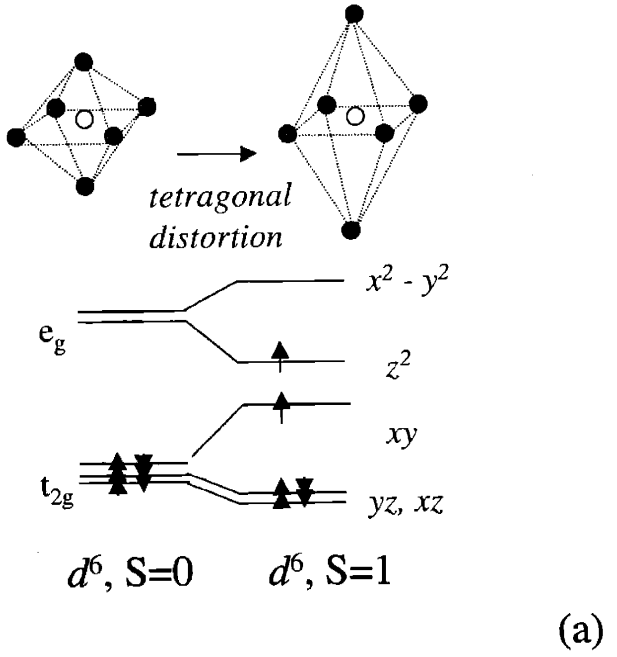

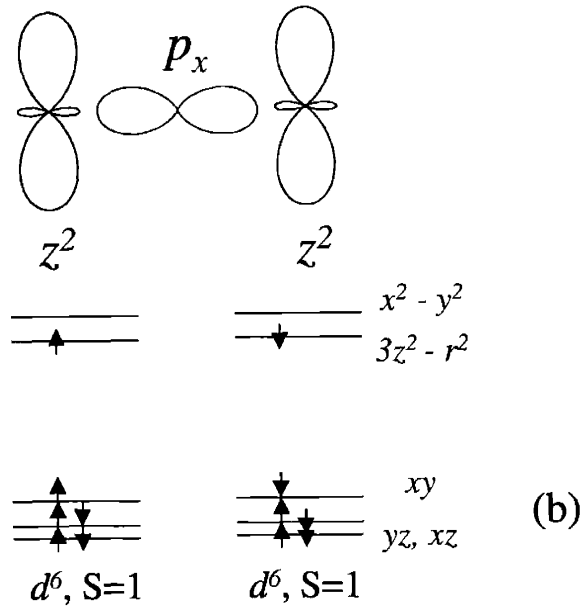

Figure 6-1: (a) A tetragonal distortion of the oxygen octahedron favors the intermediate spin state of Co^{3+} with S = 1. (b) An antiferromagnetic interaction between neighboring Co^{3+} results from super-exchange via the z^2 orbitals and the intervening oxygen p_x-orbital.

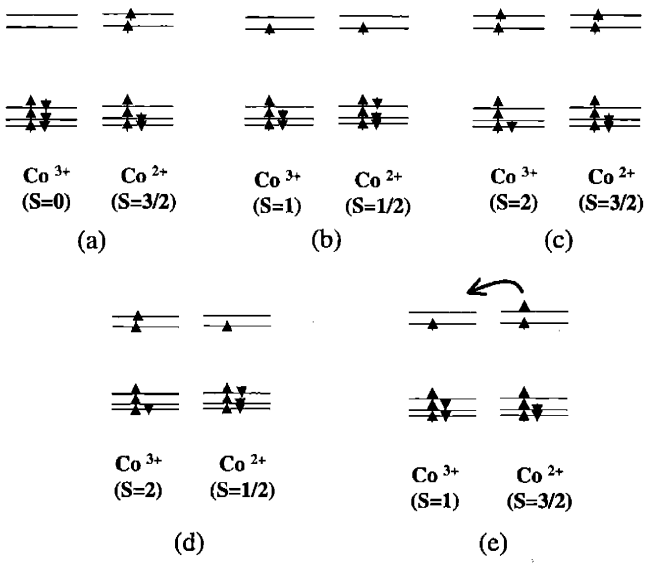

Figure 6-2: The electronic configurations of the d-orbitals for various spin states on the Co^{2+} and Co^{3+} sites.

distortion averaged over the entire unit cell is $(c-a)/a$ = (2.46-1.95)/1.95 = 0.26. (Here c is the bond length between Co and an apical oxygen ion and a is the bond length between Co and an in-plane oxygen.) This distortion should be compared to the nearly cubic symmetry of the oxygen octahedron surrounding Co in $La_{2-x}Sr_xCoO_4$ or $LaCoO_3$, in which the S = 0 ground state may be preferred. For a sample in which every Co is in the 3+ state with S = 1, an antiferromagnetic interaction between neighboring Co^{3+} ions can be explained by super-exchange [Fig. 6-1(b)] between spins in the half-filled z^2 orbitals.

We infer from the magnetic properties in samples with $\delta = 0.25$ that Co^{2+} and Co^{3+} have a ferromagnetic interaction. Unfortunately, the Curie fits of the susceptibility of samples with $\delta \sim 0.25$ do not provide a unique determination of the Co^{2+} and Co^{3+} spin states separately. The fits show that μ_{eff} is between 3.9 and 5.1 μ_b/Co and the field-cooled saturated moment is between 1.5 and 1.9 μ_b/Co. Table 4.3 summarizes the expected values of μ_{eff} and M_{sat} for the six possible spin configurations of the Co^{2+} - Co^{3+} pair, assuming $g = 2$. Based on this table, we may effectively rule out the case where the spin on the Co^{3+} site is 0 and the spin on the Co^{2+} site is 1/2, since this configuration results in a saturated moment which is only a fraction of a Bohr magneton. Let us therefore consider the dominant magnetic interaction between the five other Co^{3+} and Co^{2+} combinations.

The electron filling of the d-orbitals for each of these configurations is shown in Fig. 6-2.

In configuration (a), the spin on the Co^{3+} site is 0 and the spin on the Co^{2+} site is S = 3/2. In this case, one expects no nearest neighbor magnetic interaction to first order and next-nearest-neighbor (NNN) interactions between Co^{2+} may be important. NNN interactions between Co^{2+} with S = 3/2 are expected to be antiferromagnetic[11]

In configurations (b) and (c), one might expect a double-exchange ferromagnetic interaction mediated by the hole in the t_{2g} orbitals. However, this interaction should be small, since the t_{2g} and bridging oxygen p_x orbitals are orthogonal. Furthermore, the antiferromagnetic interactions resulting from super-exchange between spins in the half-filled z^2 orbitals in case (b) and between the half-filled $x^2 - y^2$ orbitals in case (c) would dominate this interaction.

A ferromagnetic interaction is most likely between neighboring Co^{2+} with S = 3/2 and Co^{3+} with S = 1 (configuration (e)). In this configuration, double-exchange resulting from the hopping of the electron in the $x^2 - y^2$ orbital should be the dominant interaction. This mechanism is suppressed for configuration (d): moving the electron from the Co^{3+} $x^2 - y^2$ orbital to the $x^2 - y^2$ orbital on the Co^{2+} site requires the creation of a Co^{4+} and Co^{1+} pair.

Double-exchange, as shown in configuration in (e), would provide a satisfactory explanation for the ferromagnetism observed in samples of $Bi_2Sr_2CoO_{6+\delta}$ with $\delta = 0.25$ if these samples exhibited metallic behavior. However, the ferromagnetic samples are always insulating, well below T_c. Figure 6-3 shows the resistance, R(T), and the uniform moment, M(T), measured in a 5 Tesla field. The data are shown for xtal 2002b, a sample in which ferromagnetic behavior dominates. The data show that the resistance exhibits insulating behavior, even when the moment is half its saturated value.

This behavior should be contrasted to that observed in the hole-doped manganites in the ferromagnetic regime. For these materials, the transition to ferromagnetic order at T_c is accompanied by a large decrease in the resistivity. In our predominantly ferromagnetic samples, temperature dependence measurements below T_c show no drop-off of resistance with decreasing temperature and no enhancement of conductivity with field. Therefore, the simple double-exchange mechanism is inadequate to explain the ferromagnetism. However, double-exchange, coupled with charge-ordering, may explain the behavior. If the Co^{3+} and Co^{2+} ions in the FM phase prefer a charge-ordered arrangement, then exchange of the

electron from the Co^{2+} site to the Co^{3+} site does not result in an energetically equivalent configuration. The electron in the $x^2 - y^2$ orbital on Co^{2+} is therefore localized and the ferromagnetic interaction with neighboring Co^{3+} results from virtual excitations of electrons from Co^{2+} to Co^{3+}.

Although we may explain the insulating behavior of samples with $\delta = 0.25$, it is difficult to explain the origin of the activated behavior in the conductivity for *all* oxygen concentrations, $0.25 < \delta < 0.5$. The observation that the activation energy does not depend on the Co^{2+} fraction suggests that it is the mobility rather than the density of charge carriers which is activated. On the other hand, we do observe a dip in the *magnitude* of the room temperature resistivity for samples with $T_{peak} \sim 115$ K suggesting that the number of carriers is maximal at intermediate doping.

The activated behavior of the resistivity suggests that the dominant mechanism for charge transport is polaron hopping. When the electron motion is coupled to the lattice, the electron plus lattice distortion move together as a single particle called a *polaron*. In the limit of very strong coupling to the lattice, the electron will be trapped on a single ion. In this case, the movement of an electron from one lattice site to another is an activated process and the temperature dependence of the resistivity is given by,

$$\rho \sim e^{-\frac{E_a}{2k_b T}}$$

where E_a is the polaron activation energy.

We can understand the doping dependence of the resistivity with this polaron picture. Let us assume that each Co^{2+} site introduces a lattice distortion, so that the electron + lattice distortion is a polaron. Starting from the dilute Co^{2+} limit, we would then understand the decrease in the magnitude of the resistivity with decreasing δ to result from an increase in the number of Co^{2+} sites. However, in our phase separation picture, there are two possible regions in which an additional Co^{2+} can reside: the mostly Co^{3+}, AF region or the Co^{2+} - Co^{3+} FM region. Since the clusters prefer a charge-ordered state, Co^{2+} sites in the FM clusters are strongly localized. Therefore, as the FM clusters take up more of the available volume in the Co-O sheet, there are fewer Co^{2+} polarons. This is shown schematically in Figure 6-4. This is our explanation for the observed dip in the magnitude of the resistivity at $T_{peak} = 115$ K.

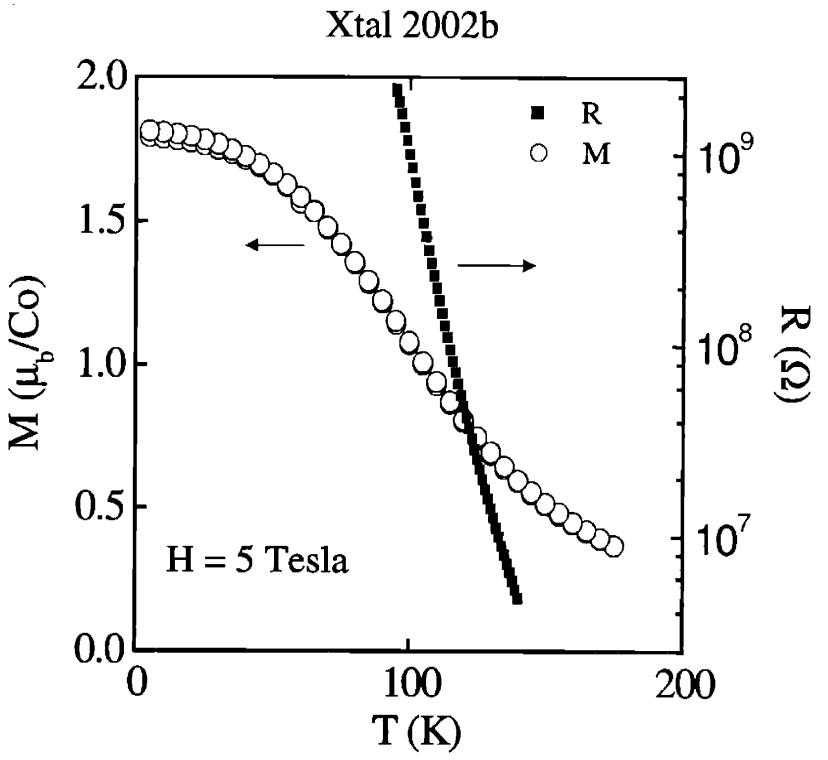

Figure 6-3: There is no evident decrease in the resistivity at the on-set of ferromagnetic ordering. Both R(T) and M(T) are measured in a 5 Tesla field. The sample shown is xtal 2002b, which has a $T_N \sim 80$ K and a large ferromagnetic moment.

It should be noted that the resistivity in the related cobaltate $La_{2-x}Sr_xCoO_4$ is also activated, with an activation energy of $\sim$ 500 meV.[37] In addition, measurements of the resistivity in these crystals, as a function of Sr, show that the activation energy does not change with doping in the range $0.4 < x < 0.8$. When $x = 0.5$, the magnitude of the resistivity is at a maximum. Note that $x = 0.5$ in these crystals corresponds to $Bi_2Sr_2CoO_{6+\delta}$ with $\delta = 0.25$.

6.2 Microscopic model for phase separation

We now consider a specific model of the spin arrangement at intermediate doping, $0.25 < x < 0.5$, that can explain the observed field dependence. In particular, any model must explain the simultaneous change in the structure of the AF and FM phases at H_c. Figure 6-5 shows a plausible magnetic ground state at the phase boundary between adjacent AF and FM domains. In the figure, the boundary between the two phases occurs at the middle *bc* plane, since to the right of this plane all of the Co ions are 3+, while to the left, there are equal numbers of 2+ and 3+ Co ions. The AF phase consists of only Co^{3+} spins, which

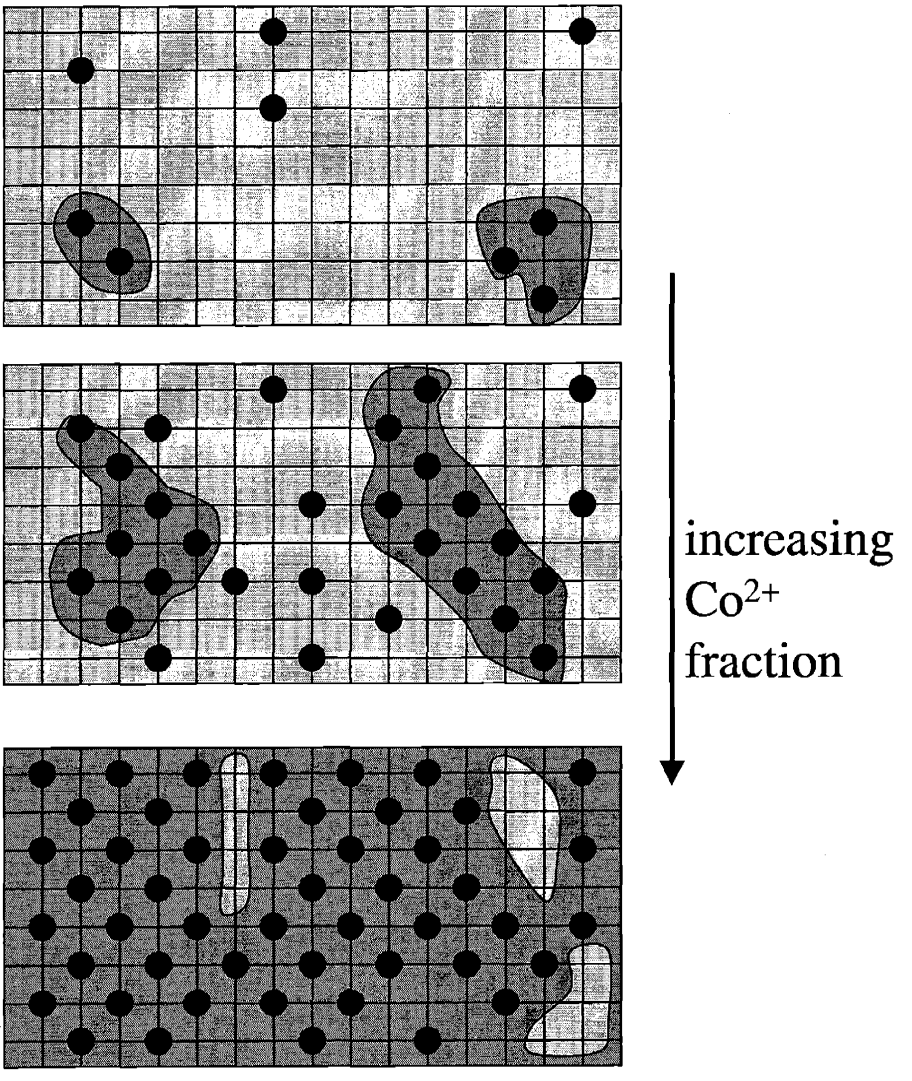

Figure 6-4: Increasing the Co^{2+} fraction increases the number of polaron sites and the volume of FM clusters. Only those electrons in the Co^{3+} background are mobile.

have the spin arrangement discussed in Section 4.1. Note that this means that all of the spins in a given *ac* plane point in the same direction, which is described by a ferromagnetic $J_{\perp}^{AF}$ between adjacent layers in the AF phase. The relevant in-plane exchange interactions are J_{FM} between nearest neighbor Co^{3+} and Co^{2+} spins and J_{AF} between nearest neighbor Co^{3+} spins. We assume that J_{FM} is less than J_{AF}.

In the top cobalt oxide layer shown in Fig. 6-5a, the ordering of the AF spins at T_N creates an effective field pointing to the right on the FM cluster, which therefore prefers to polarize in this direction. In the bottom layer, the antiferromagnetic ordering in the AF phase causes the FM cluster to polarize toward the left. In Figure 6-5a, all of the magnetic bonds are satisfied: all nearest neighbor Co^{3+} spins are antiparallel and all neighboring Co^{2+} and Co^{3+} spins are parallel. In addition, the perpendicular couplings between layers in the AF phase and between ferromagnetic layers in the FM phase are satisfied because the FM clusters are antiparallel from layer to layer.

The model in Figure 6-5 can explain the effect of the applied magnetic field, which induces both a change in the stacking between layers in the AF phase and the onset of an overt moment in the FM phase at the same field. Consider the interaction of the spins in the two-phase mixture in Figure 6-5 with a magnetic field along the spin direction, **a**. The spins in the AF phase are not expected to contribute to the susceptibility since the field is applied along the spin direction. The FM phase has a large polarizability at fairly small fields (< 1 T). In the mixed phase crystal, there is a strong in-plane FM exchange at the phase boundary which changes sign from layer to layer. The surrounding AF phase prevents the FM cluster from polarizing along the field direction without costing the in-plane FM exchange energy, J_{FM}, for those spins on the edge of the cluster. However, a rotation of every other Co^{3+} AF layer allows the FM domain to polarize with the field, without breaking the in-plane bonds at the phase boundary (Figure 6-5(b)). Such a rotation results in a shift of the AF peaks from the positions (0, 1, L = *even*) to (0, 1, L = *odd*) at the same field as the onset in the uniform moment, as observed.

The critical field for the transition described above is determined by a balance between the Zeeman energy gained by the spins in the FM domain and the cost in the exchange energy between layers in the AF domain. Consider a square which contains a single FM patch, which is correlated over several layers. The FM patch contains N_{FM} sites and the AF contains N_{AF} sites. At zero field, the FM moment in adjacent layers points in opposite

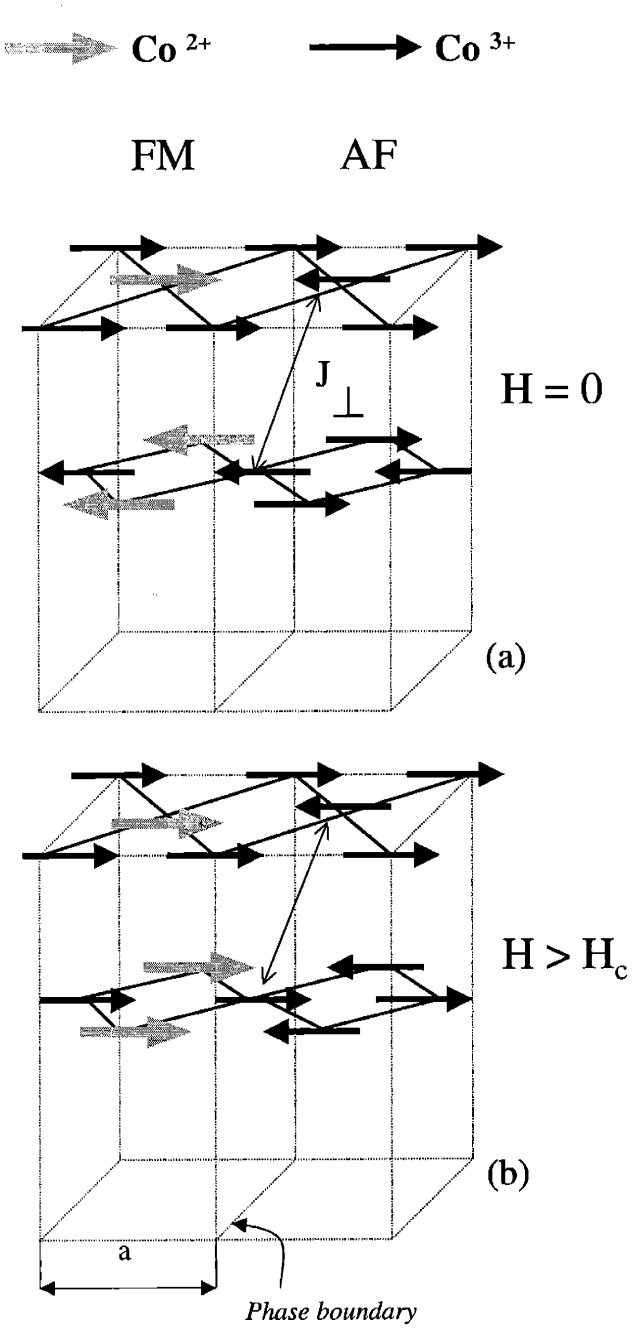

Figure 6-5: Idealization of the two-phase mixture. The left cell is in the $\delta = 0.25$ FM phase and the right cell is in the $\delta = 0.5$ AF phase. The zero field configuration is shown in (a). The double headed arrow connects nearest-neighbor spins in adjacent layers in the AF phase, which are parallel at zero-field. In the $\delta = 0.25$ phase, the spins are ferromagnetically arranged in the layer, but at H = 0, adjacent spins point in opposite directions. The FM phase is pinned in each layer by the FM coupling, J_{FM}, between Co^{3+} and Co^{2+} spins at the phase boundary. (b) When the field is greater than H_c, every other layer (in both phases) rotates by 180°. The high-field configuration preserves the in-plane interactions J_{FM} and J_{AF} but costs the perpendicular exchange $J_\perp$ in the antiferromagnetic phase.

directions. If a field is now applied along **a**, then only half of the layers will be oriented in the correct direction.

When the FM patches rotate into the field, the gain in magnetic energy per layer is given by

$$\Delta E = -\frac{1}{2} N_{FM}(2g\mu_b S_{FM} H) \tag{6.1}$$

The factor of $\frac{1}{2}$ occurs because only half of the FM spins re-orient.

On the other hand, there is a cost in energy to rotate every other layer in the AF phase. This is given by

$$\Delta E = \frac{z}{2} N_{AF}(2J_\perp S_{AF}^2) \tag{6.2}$$

In this equation, z is the number of nearest neighbors in adjacent layers.

These two energies are equal at the critical field, H_c

$$H_c = \frac{\frac{z}{2} n_{AF}(J_\perp^{AF} S_{AF}^2)}{n_{FM}(g\mu_b S_{FM})} \tag{6.3}$$

where $n_{FM} = N_{FM}/N$ and $n_{AF} = N_{AF}/N$ are the densities of the FM and AF phases respectively, $J_\perp^{AF}$ is the inter-layer exchange in the AF phase and $z = 4$ is the number of nearest neighbors. The expression for H_c in Equation 6.3 explains the decrease of H_c with T_{peak} shown in Figure 4-35: a decreasing T_{peak} means the ratio of n_{FM} to n_{AF} is decreasing.

For the sample with T_N = 215 K, the experimentally measured H_c is 1.6 Tesla. Since δ is close to 0.4 for this T_N, $n_{FM} = 2(1\text{-}2\delta) = 0.4$ and $n_{AF} = 0.6$. Using $S_{FM} \sim 5/4$ and $S_{AF} \sim 1$, the above equation gives $J_\perp \sim 38$ μeV. This value should be compared with other layered transition metal oxides. For example, in La_2CuO_4, $J_\perp$ is about 6 μeV. The ratio of $J_\perp$ to J_{NN} in La_2CuO_4 is about 5 x 10^{-5}, while in $Bi_2Sr_2CoO_{6+\delta}$ it is about 2 x 10^{-3}.

Although the model described in Figure 6-5 can explain the behavior of a single FM domain in the AF host, the random direction of the FM domains makes the real system more complicated. The following is an explanation proposed by Patrick Lee and Senthil Todadri which reconciles the random orientation of the FM clusters with the local picture suggested above.[38]

Consider the large area patch in the Co-O plane shown in Figure 6-6. Two FM patches are shown, separated by an AF domain. The Co^{2+} can choose to sit on one of two sub-lattices, which we will call the A and B sub-lattices. If the Co^{2+} sits on an A sub-lattice, it will point along **a** and if it sits on a B sub-lattice, it will point along **a**. Therefore, in Figure 6-6 the upper patch is an A-type domain and the lower patch is a B-type domain. Let us also assume that the stacking of the FM domains perpendicular to the layers maintains the AB sub-lattice coherence, at least on a finite length scale. We see from Fig. 6-6 that the A-type and B-type domains are driven by the boundary with the AF to order in *opposite* directions. Thus in zero field the FM order is necessarily short range, with a coherence length of the order of the domain size. If we now apply a large magnetic field in the plane along **a**, the spins in the B-type domain will flip. This will tend to flip the AF sub-lattice magnetization as explained earlier. However, this is opposed by the A-type domains, which do not flip. The orientation of the AF sub-lattice magnetization is therefore frustrated.

It turns out that this problem maps onto the Random Field Ising model in two-dimensions. To see this, define M_S as the sub-lattice magnetization ($M_S = M_A$ - M_B, where M_A and M_B are the magnetizations of the A-type and B-type domains, respectively). The coupling across the A-type and B-type FM domain walls can be modeled by an effective field $H_S(\vec{r})$, which is positive for A-type and negative for B-type domains. Extending the description to different layers, we see from Figure 6-5(b) that for a given FM patch, the coupling changes sign from one layer to the next. After course graining (i.e. averaging over large length scales), we may write down the following effective Hamiltonian

$$H_{eff} = \sum_j \int d^2r(-1)^j H_S(\vec{r}) M_S(\vec{r}), \tag{6.4}$$

where j is the layer index. The sum over j is restricted to the number of layers where the Co^{2+} coherently occupy A or B sites. Equation 6.4 is the classic Random Field Ising model. By the Imry-Ma argument, the system may break up into domains of size L.[39, 40] For a given dimension d, the energy cost of the domain walls σL^{d-1} is balanced by the RMS fluctuation of the random field energy, which goes as $|H_S|L^{d/2}$. According to this argument, $d = 2$ is the lower critical dimension; i.e., the system is always disordered below two dimensions. For a two-dimensinal system, a rigorous proof states that the ground state is always disordered, independent of the strength of the random field. Apparently,

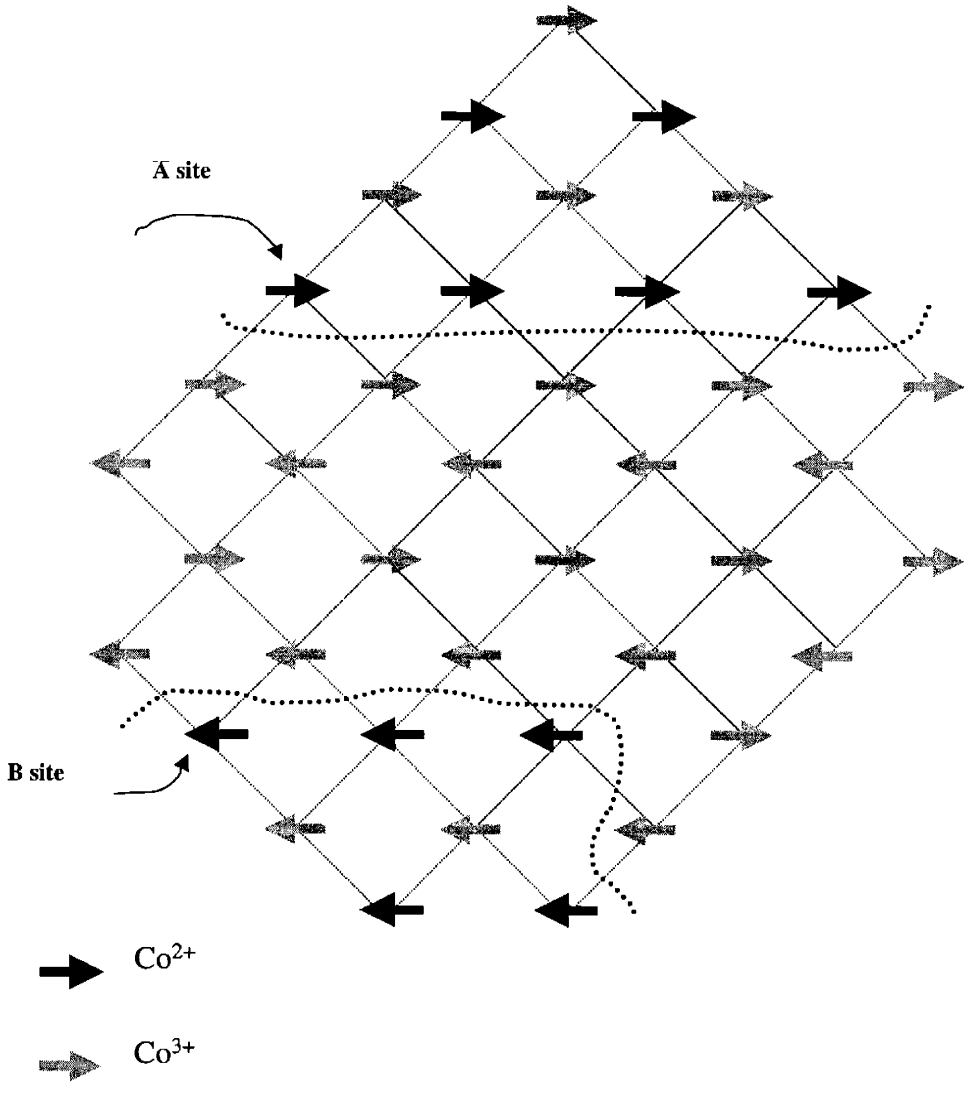

Figure 6-6: Illustration of the zero external field spin configuration in a single layer, showing an AF region ($\delta = 0.5$) in contact with two FM domains ($\delta = 0.25$). The Co^{2+} spins lie on sub-lattice A in the top domain and on sub-lattice B in the bottom domain. The two FM domains are therefore oriented in opposite directions.

the system is always able to find a domain configuration which allows it to gain from the fluctuations in the random field configurations. The domain size will be extremely large for weak random fields, but nevertheless finite. Based on these arguments, our picture is that above H_c, the AF region will break up into large domains with opposite M_S. However, because the random field changes sign from layer to layer, the sublattice magnetization on neighboring layers is always opposite; i.e., the *relative* orientation of the sublattice is always flipped by applying a large magnetic field.

The random field model makes several predictions, which may be tested experimentally:

1. In zero field, the c-axis correlation length of the FM Bragg peak is limited by the c-axis coherence of the sublattice occupation of the Co^{2+}.

2. In high field, the c-axis correlation length of the AF Bragg peak is limited by the same length as in (1).

3. In zero field, the FM correlation length in the ab plane is limited by the domain size of the $\delta = 0.25$ clusters.

4. In high field, the AF correlation length in the ab plane is finite, but may be much larger than the FM correlation length in (3).

5. The random field Ising model may explain the glassy behavior and hysteresis effects we observe.

These arguments likely hold only in the dilute limit. To test these predictions, we need to look in samples in which the ferromagnetic fraction is small, such as xtal 2043 which has a $T_N \sim 225$ K.

6.3 Implications of the phase separation model

From an energy standpoint, segregation into hole rich, Co^{3+} regions and hole poor, Co^{2+} - Co^{3+} regions, is extremely unfavorable. Therefore, we propose that oxygen, which may be mobile at the annealing temperatures necessary to change the magnetic properties, accommodates charge inhomogeneity. A higher concentration of oxygen vacancies in the vicinity of the FM, Co^{2+} rich regions would screen the excess charge.

Direct evidence for oxygen inhomogeneity is still lacking. One signature of oxygen inhomogeneity would be the presence of more than one c-axis lattice constant. In $Bi_2Sr_2CoO_{6+\delta}$, the c-axis lattice constant is observed to *decrease* slightly when oxygen is removed: The $\delta \sim 0.5$ crystals have a c-axis lattice constant of 23.6-23.7 $\AA$, while the reduced samples with $\delta \sim 0.25$ crystals have a c-axis lattice closer to 23.4. The presence of two phases with lattice constants differring by a few percent should be easily measured with neutrons and x-rays.

We have not observed multiple lattice constants with neutrons. Considering the resolution of our measurements, any splitting of a structural (0, 0, L) peak resulting from different c-axis lattice constants was less than 1%. We have also tried to look for splitting of the (0, 0, L) peaks using the much higher resolution available at a synchrotron light source; unfortunately, we were only able to study $\delta = 0.25$ crystals, which were expected to be single phase.

More experiments devoted to structural studies are needed to show direct evidence of oxygen inhomogeneity. However, the TGA measurements described in Chapter 5 indicate the important role of oxygen in facilitating phase separation. When oxygen is re-introduced into reduced samples at temperatures < 900 C, the oxygen vacancies appear to fill in randomly. The result is a mostly Co^{3+} lattice, which orders antiferromagnetically but does not exhibit a large ferromagnetic peak or field induced moment. Only when oxygen is introduced at ~ 900 C, do the signatures of phase separtion return.

This study is an important part of our picture of phase separation. If the FM clusters resulted from a random distribution of the magnetically interacting Co^{2+} sites, we would not observe irreversible behavior in the annealing.

We do not know the mechanism which favors the formation of the FM clusters in the AF phase. The clustering and charge ordering must occur at temperatures well above 300 K. Certainly, the charge-order peaks which we observe with neutrons suggest a melting temperature well above 300 K. The annealing studies suggest that the mechanism for clustering is a high temperature phenomenon. This may imply that a structural distortion occurs at high temperatures, which accommodates oxygen inhomogeneity and hence the formation of the Co^{2+} and Co^{3+} clusters. The question remains, however, of whether it is the charge ordering which drives the oxygen inhomogeneity, or if it is the quenching of oxygen inhomogeneity which permits clusters to form.

Even within the context of the phase-separation model, the susceptibility in the para-

magnetic phase, above T_{peak}, is puzzling. The ferromagnetic-like peak is well fit to a Curie-Weiss susceptibility above T_{peak}. However, Curie-Weiss is a mean field description of the interaction between neighboring spins and the transition temperature, T_c, extracted from the fit is a measure of the average effective magnetic field on a spin due to the magnetization of surrounding spins. We clearly observe two-dimensional scattering above T_N in the antiferromagnetic phase and yet this appears to have little effect on the susceptibility. This suggests that the spins in the FM cluster fluctuate as free objects above the transition to long-range order in the AF phase.

Another complication is the shift in T_{peak} with T_N. We have argued that the intrinsic T_c of the pure FM phase is 100 K, while the pure AF phase orders at a much higher temperature, $T_N \sim 250$ K. We suggested that the observation of a $T_{peak} > 100$ K in mixed phase samples was a result of the effective field, at the phase boundary, of the AF phase on the FM phase. Such a field would cause the ferromagnetic spins to order. However, this effective field is the same in-plane J_{FM} which governs ferromagnetic ordering in the pure FM samples. Furthermore, the interaction at the phase boundary can only be communicated to the interior of the FM domains by the in-plane coupling J_{FM}. How, then, can the FM regions order at the Néel transition temperature?[1] We can only explain this behavior if the FM domains are extremely rarefied, so that the FM interaction at the perimeter of the domains is large compared to the area of the domains.

Many of these questions may be answered by further neutron scattering measurements of Co^{2+} - dilute samples, at zero-field. Analysis of the FM phase at zero-field would provide information on the dynamics of the spins in these domains above T_N. In addition, we would be able to test the prediction that the ferromagnetic clusters are a measure of the coherence of the Co^{2+}- rich clusters. So far, we have only made careful studies of the FM phase in intermediate doped samples at high fields. Since the field forces all of the spins in all of the clusters to have a uniform moment, we measure sharp Bragg peaks, even though the FM clusters themselves may only occur on small length scales.

[1] I would like to thank Amnon Aharony for pointing out this important point.

6.4 Conclusions

In this thesis, we have studied the evolution of the magnetic properties in $Bi_2Sr_2CoO_{6+\delta}$ as a function of the oxgyen content δ. We have shown that in the compound with $\delta \sim 0.5$, the magnetic Co^{3+} ions are in the intermediate spin state with S = 1 and order antiferromagnetically below $T_N \sim 230$ K. The antiferromagnetic order is characterized by nearest-neighbor spins which are antiparallel in the plane and point along the orthorhombic a-axis. The compound with $\delta \sim 0.25$ should have an equal concentration of Co^{2+} and Co^{3+} sites. The in-plane interaction between Co^{2+} and Co^{3+} is ferromagnetic with a $T_c \sim 100$ K. However, a weak inter-plane coupling causes adjacent layers to point in opposite directions such that the uniform moment is zero at zero field.

Our central finding is that antiferromagnetic and ferromagnetic regions, characteristic of the $\delta \sim 0.5$ and $\delta \sim 0.25$ limits, co-exist in samples with $0.25 < \delta < 0.5$. These phases are distinct in that the magnetic order parameter describing the antiferromagnetic phase is a staggered moment and the order parameter describing the ferromagnetic phase is a uniform moment. However, field dependence measurements suggest that the two phases interact at their phase boundary, with the FM domains exerting a random field on the AF region above a field H_c.

The oxygen annealing measurements suggest that oxygen plays an important role in facilitating phase separation. We propose that oxygen inhomogeneities on small length scales accommodates electronic phase separation. That is, we do not believe that the oxygen content of our samples are macroscopically inhomogeneous; the well defined T_N of large crystals measured with neutrons precludes macroscopic phase separation. More measurements devoted to looking for oxygen inhomogeneities are required to confirm this picture.

The magnetic inhomogeneities found in $Bi_2Sr_2CoO_{6+\delta}$ suggest that this material is an interesting analogue to the hole-doped manganites in which magnetic and electronic phase separation are believed to occur. Given the similar structures for $Bi_2Sr_2CoO_{6+\delta}$ and $Bi_2Sr_2CuO_{6+\delta}$, our evidence suggests oxygen inhomogeneities may be important for the cuprate system as well.

Appendix A

Nuclear and magnetic form factors

Reflection	F_{nuc} (10^{-12} cm)	d-spacing ($\AA$)	θ	sin(2θ)
(0, 0, 2)	9.3	11.8	5.72	0.198
(0, 0, 4)	5.6	5.9	11.48	0.39
(0, 0, 6)	24.1	3.9	17.46	0.57
(0, 0, 8)	29	2.95	23.45	0.72
(0, 0, 10)	44.6	2.36	29.87	0.86
(0, 2, 0)	48	2.72	25.6	0.779

Table A.1: Fundamental nuclear reflections and associated nuclear form factors. The θ and sin(2θ) values correspond to an incident neutron energy of 14.7 meV.

Reflection	s = $\frac{Q}{4\pi}$ ($\AA^{-1}$)	f	θ	sin(2θ)
(0, 1, 0)	0.092	0.938	12.44	0.42
(0, 1, 1)	0.094	0.934	12.77	0.42
(0, 1, 2)	0.101	0.925	13.71	0.46
(0, 1, 3)	0.112	0.909	15.84	0.525
(0, 1, 4)	0.125	0.888	17.10	0.56
(0, 1, 5)	0.140	0.862	19.21	0.62
(0, 0, 4)	0.085	0.946	11.48	0.39

Table A.2: Magnetic reflections and associated magnetic form factors for Co^{3+}.[30] The form factor is assumed to be spherically symmetric in $s = \frac{Q}{4\pi}$ and follows the form $Ae^{-as^2} + B^{-bs^2} + C^{-cs^2} + D$, with the experimentally determined parameters $A = 0.3902, a = 12.508, B = 0.6324, b = 4.457, C = -0.015, c = 0.034$, and $D = 0.1272$. The θ and sin(2θ) values correspond to an incident neutron energy of 14.7 meV.

Energy (meV) to wavenumber ($\mathring{A}^{-1}$)	$k = 0.6969\ E^{1/2}$
Wavenumber ($\mathring{A}^{-1}$) to energy (meV)	$E = 2.06\ k^2$
Energy (meV) to wavelength ($\mathring{A}$)	$\lambda = 9.016\ E^{-1/2}$
Wavelength ($\mathring{A}$) to energy (meV)	$E = 81.29\ \lambda^{-2}$

Table A.3: Useful conversions for neutron diffraction. The energy-momentum relation for a neutron is given by $\frac{\hbar^2 k^2}{2m} = E$, where $k = \frac{2\pi}{\lambda}$ is the neutron wavevector and $m = 1.67 \times 10^{-27}$ kg is the neutron mass.

Bibliography

[1] E. Dagotto, T. Hotta, and A. Moreo. *Physics Reports* **344**, 2001.

[2] A. P. Ramirez. *Journal of Physics: Condensed Matter* **9**, 1997.

[3] M. B. Salamon and M. Jaime. *Review of Modern Physics* **73**, 2001.

[4] R. J. Birgeneau and G. Shirane. *Physical Properties of high temperature superconductors* **1**, 1989.

[5] M. A. Kastner, R. J. Birgeneau, G. Shirane, and Y. Endoh. *Reviews of Modern Physics* **70**, 1998.

[6] G. Briceno, H. Chang, X. Sun, P. G. Schultz, and X. D. Ziang. *Science* **270**, 1995.

[7] M. Abbate, J. C. Fuggle, A. Fujimori, L. H. Tjeng, C. T. Chen, R. Potze, G. A. Sawatzky, H. Eisaki, and S. Uchica. *Physical Review B* **47**, 1993.

[8] M. A. Senaris-Rodriguez and J. B. Goodenough. *Journal of Solid State Chemistry* **118**, 1995.

[9] R. J. Cava, K. Yamaura, S. Loureiro, Q. Huang, R. W. Erwin, J. W. Lynn, and D. Young. *Physica C* **341-348**, 2000.

[10] K. Yamada, M. Matsuda, Y. Endoh, B. Keimer, R. J. Birgeneau, S. Onodara, J. Mizusaki, T. Matsuura, and G. Shirane. *Physical Review B* **39**, 1989.

[11] I. A. Zaliznyak, J. P. Hill, J. M. Tranquada, R. Erwin, and Y. Moritomo. *Physical Review Letters* **85**, 2000.

[12] J. M. Tarascon, P. M. Miceli, P. Barboux, D. M. Hwang, G. W. Hull, M. Giroud, L. H. Greene, Y. Le Page, W. R. McKinnon, E. Tselepis, G. Pleizier, M. Eibschutz, D. A. Neumann, and J. J. Rhyne. *Physical Review B* **39**, 1989.

[13] P. H. Duvigneaud, C. De Boeck, and V. F. Guo. *Superconducting Science and Technology* **11**, 1998.

[14] K. Koike, S. Kambe, S. Ohshima, Y. Takasugi, T. Furusawa, and T. Shiomi. *Physica C* **282-287**, 1997.

[15] A. Moreo, S. Yunoki, E. Dagotto, and T. Hotta. *Science* **283**, 2001.

[16] Q. Huang, J. W. Lynn, R. W. Erwin, A. Santoro, D. C. Dender, V. N. Smolyaninova, K. Ghosh, and R. L. Greene. *Physical Review B* **61**, 2000.

[17] M. Uehara, S. Mori, C. H. Chen, and S. W. Cheong. *Nature* **399**, 1999.

[18] B. Lake, G. Aeppli, K. N. Clausen, D. F. McMorrow, K. Lefmann, N. E. Hussey, N. Mangkorntong, M. Nohara, H. Takagi, T. E. Mason, and A. Schroder. *Science* **291**, 2001.

[19] B. Khaykovich, Y. S. Lee, R. W. Erwin, S. H. Lee, S. Wakimoto, K. J. Thomas, M. A. Kastner, and R. J. Birgeneau. *Physical Review B* **63**, 2002.

[20] J. E. Hoffman, E. W. Hudson, K. M. Lang, V. Madhavan, E. Eisake, S. Uchida, and J. C. Davis. *Science* **295**, 2002.

[21] J. Mira, J. Rivas, G. Baio, G. Barucca, R. Caciuffo, D. Rinaldi, D. Fiorani, and M. A. Senaris Rodriguez. *Journal of Applied Physics* **89**, 2001.

[22] R. Caciuffo, D. Rinaldi, G. Barucca, J. Mira, J. Rivas, M. A. Senaris Rodriguez, P. G. Radaelli, D. Fiorani, and J. B. Goodenough. *Physical Review B* **59**, 1999.

[23] G. L. Squires. *Introduction to the theory of thermal neutron scattering.* Cambridge University Press, 1978.

[24] Gen Shirane, Steve Shapiro, and John Tranquada. *Neutron Scattering.* Cambridge University Press, 2001.

[25] L. Dobrzynski and K. Blinowski. *Neutrons and solid state physics.* Ellis Horwood Limited, 1994.

[26] Roger Pynn. Neutron scattering: A primer. *Los Alamos Science* **19**, 1990.

[27] J. M. Tranquada, J. E. Lorenzo, D. J. Buttrey, and V. Sachan. *Physical Review B* **52**, 1995.

[28] Y. S. Lee, R. J. Birgeneau, M. A. Kastner, Y. Endoh, S. Wakimoto, K. Yamada, R. W. Erwin, S. H. Lee, and G. Shirane. *Physical Review B* **60**, 1999.

[29] M. V. Zinkevich, S. A. Prodan, Yu. G Zonov, and V. V. Vashook. Stability, oxygen nonstoichiometry, and transformations of the $bi_2sr_2coo_{6+\delta}$ ceramic. *Journal of Solid State Chemistry*, **136**.

[30] A. J. C. Wilson, editor. *International Tables for Crystallography*, volume C. Kluwer Academic Publishers, 1995.

[31] M. Greven, R. J. Birgeneau, Y. EMdoh, M. A. Kastner, M. Matsuda, and G. Shirane. *Zeitschrift fur Physik B: Condensed Matter* **96**, 1995.

[32] R. J. Birgeneau, Jr. J. Skalyo, and G. Shirane. *Physical Review B* **3**, 1971.

[33] R. J. Birgeneau, J. Als-Nielsen, and G. Shirane. *Physical Review B* **16**, 1977.

[34] P. Aleshkevych, M. Berkowski, W. Ryba-Romanowski, and H. Szymczak. *Physical State of Solids* **218**, 2000.

[35] T Thio, T. R. Thurston, N. W. Preyer, P. J. Picone, M. A. Kastner, H. P. Jenssen, D. R. Gabbe, C. Y. Chen, R. J. Birgeneau, and A. Aharony. *Physical Review B* **38**, 1988.

[36] M. E. Fisher and D. R. Nelson. *Physical Review Letters*, 1974.

[37] Y. Moritomo, K. Higashi, K. Matsuda, and A. Nakamura. *Physical Review B* **55**, 1997.

[38] K. J. Thomas, Y. S. Lee, F. C. Chou, B. Khaykovich, P. A. Lee, M. A. Kastner, R. J. Cava, and J. W. Lynn. *Physical Review B* **66**, 2002.

[39] J. Z. Imbrie. *Physical Review Letters* **53**, 1984.

[40] M. Aizeman and J. Wehr. *Physical Review Letters* **62**, 1989.